University of Central Florida

STARS

2022

Power Inductors: Design, Modeling and Analysis

Subash Pokharel
University of Central Florida

POWER INDUCTORS: DESIGN, MODELING AND ANALYSIS

by

SUBASH POKHAREL
B.E. Tribhuvan University, 2016

A dissertation submitted in partial fulfilment of the requirements
for the degree of Doctor of Philosophy
in the Department of Electrical and Computer Engineering
in the College of Engineering and Computer Science
at the University of Central Florida
Orlando, Florida

Spring Term
2022

Major Professor: Aleksandar Dimitrovski

ABSTRACT

Power inductors, or reactors as they are called in the power industry, are one of the fundamental components of a power system. They serve various purposes in both conventional and emerging power systems including: power flow control, fault current limitation, reactive power compensation, harmonic filtering, and others. This dissertation explores the design and applications of conventional power inductors and ways to overcome their shortcomings and expand their functionalities. In addition, novel inductor designs are proposed and analyzed to address power system challenges. A series of inductors, including traditional constant reactance inductor, gapless ferromagnetic core reactor (GFCR) (both costant and variable reactance), and magnetic amplifier-based variable reactance reactor (both single-phase and three-phase), are considered and examined. The various unique inductor designs have been analyzed, both analytically and numerically, and their potential assessed for applications in modern power systems using novel simulation frameworks. A finite element analysis (FEA) based numerical modeling has been carried out for all inductors for accurate representation and analysis. On the other hand, analytical modeling based on magnetic equivalent circuit (MEC) has been presented, to complement the FEA-based approach and overcome its shortcomings. A comparative analysis of the processes provides insights into the effectiveness and accuracy of the proposed analytical models. Also, an advanced data-intensive machine learning (ML) approach to understanding the working of magnetic amplifier technology has been proposed. Additionally, a unique optimal power flow (OPF) formulation with variable reactance because of the power magnetic devices like a magnetic amplifier in a power system is presented. This dissertation covers the presentation of novel inductor designs and their advantages, analyses, and assessments to the broad scientific community and the industry. This kind of research is expected to pave the pathway for future innovations in inductor technologies for applications in modern power systems to make them more reliable, resilient, and efficient.

I want to dedicate this dissertation to my parents, whose enormous sacrifices, hard work, and constant belief have led me to where I am today. I am indebted to you. I love you.

ACKNOWLEDGMENTS

TABLE OF CONTENTS

LIST OF FIGURES

LIST OF TABLES

CHAPTER 1: INTRODUCTION

Energy system is one of the most critical infrastructure systems of a modern society, and the electric power system is its backbone. The objective of an electric power system is to generate and deliver electric energy in the most reliable, secure, efficient, and economical way. The demand for quantity and quality of electric energy is growing continuously throughout the world. This growth puts the existing aging power grids under much additional stress and they become increasingly vulnerable. Recent changes in the power industry have further exaggerated the problem. These changes that result with different power flow patterns include:

- Deregulated market structure– in a free market, the power exchange is driven by economics rather than technical capabilities

- Emerging technologies– the proliferation of distributed energy resources (DERs), renewable energy sources (RESs), demand response

- Governmental policies and regulations for reduction of greenhouse gas (GHG) emitting energy sources and incentivization for GHG neutral sources

- Increased frequency and intensity of extreme weather events and natural disasters (high-impact low-frequency events)

Despite these changes, the investment in the new transmission and distribution (T&D) systems has not followed the generation and demand growth. In 2019, the investment in transmission infrastructure rose up 1% over the previous year to \$23.5 billion, while the energy production grew by 6 % and energy demand remained almost the same [1]. The reasons for limited T&D

---

[1] Source: U.S. Energy Information Administration (Mar 2022)

investment include administrative, ecological, and economic factors. For instance, the average cost of transmission capability addition for wind energy system is found to be \$300/kW in [1].

The compound effect on the power grid is bottlenecks leading to overloads, loop flows, stability, and security limit violations. Furthermore, the system has become more complex to operate, stressed and less reliable, resilient, and secure.

Therefore, getting the most out of the existing T&D system is the only viable choice now and the near future, and it is vital to find ways to optimize the existing infrastructure utilization. In general, natural power flows through uncontrolled electrical networks are not economically optimal. The use of power flow controller (PFC)– a grid enhancing technology– is a preferred option to fully utilize the power transfer capacity of existing power lines [2].

Principle of Power Flow Control

The power flow should be fully controlled to achieve optimal and secure system operation. The objective is to balance the power generation to the loads with lower system loss and provide economically but premium quality electricity services to end customers. An effective power flow control can increase power transfer capability, lower system loss, keep voltage drop to a minimum, improve security and stability margin, remove congestion, etc. These effects, in turn, improve system reliability and efficiency, postpone transmission expansion, reduce power outages and blackouts, and have positive impacts on the environment. These effects of power flow control mean savings of billions of dollars.

With line resistances and shunt elements neglected, the active power flow between two buses in a

power system, bus 1 and bus 2, is simply expressed as:

$$P = \frac{V_1 V_2}{X} sin\delta \qquad (1.1)$$

where, V_1 and V_2 are the voltage magnitudes of bus 1 and bus 2, respectively; X is the reactance of the line connecting the buses and δ is the phase angle difference between the buses. According to (1.1), the active power flow between the buses can be controlled by changing either voltage magnitudes, phase angle between bus voltages, or reactance of the connecting line. It is also evident that active power flow is directly proportional to the square of the voltage level, closely linear to the phase angle difference, while it is inversely proportional to the reactance of the line. The focus of this thesis is on utilizing the last dependency.

Power Flow Controllers (PFCs)

The most widely used PFC technologies include tap-changing and phase-shifting transformers, switchable shunt units, synchronous condensers, different types of flexible ac transmission system devices (FACTS), and distributed FACTS (DFACTS). PFCs, including voltage regulating transformer (VRT), tap changing transformer (TCT), static var compensator (SVC), static synchronous compensator (STATCOM), control the power flow by voltage regulation. In contrast, phase angle regulators (PARs) and phase-shifting transformers (PSTs) control the power flow by phase angle regulation. Thyristor controlled series capacitor (TCSC) falls under the FACTS device controlling power flow by series reactance regulation. For the first time in the United States, the Tennessee Valley Authority (TVA) at the Sullivan substation in North-Eastern Tennessee commissioned STATCOM using gate-turn-off thyristors (GTO) valves in 1995. It offered an excellent viability test of this kind of equipment application in high power transmission systems [3], [4].

The FACTS devices can also be categorized as follows:

- First-generation FACTS devices: It includes devices like static var compensator (SVC), Thyristor switched capacitor (TSC), and Thyristor switched reactor (TSR). The first generation FACTS devices provide reactive power compensation and voltage regulation with little dynamic and transient capability by switching on/off or stepwise control.

- Second-generation FACTS devices: It includes devices like Thyristor controlled series capacitor (TCSC), STATCOM, and Static synchronous series compensator (SSSC). It has continuous control to provide the functionality of reactive and real power compensation, voltage or current regulation, and oscillation damping with limited dynamic and transient capabilities.

- Third-generation FACTS devices: This generation of FACTS devices includes Unified power flow controller (UPFC) and Interline power flow controller (IPFC), which have a complete and continuous power control, voltage/current control, oscillation damping, fault current limiting with fully dynamic and transient capability.

The FACTS-based technologies do not provide complete network controllability because of either lack of functionality and flexibility or high costs and relatively low reliability. The main impeding factor for widespread FACTS devices deployment and adaptation is the cost of manufacturing, siting, equipment-housing, installation, and other auxiliary services. According to an internal ORNL document from 2013, the cost of a first-generation FACTS device lies at \$15/kVA-\$25/kVA, while the second-generation FACTS devices cost \$50/kVA-\$100/kVA; similarly, the cost range of third-generation FACTS devices was reported to be \$100/kVA-\$300/kVA. Therefore it is urgent to identify some advanced but technically and economically feasible technologies for power flow control without losing functionality.

Among the alternative solutions, the reactors fall into the category of electromagnetic devices. The magnetic characteristics with electric supply dictate its working. It holds for both fixed and flexible reactors. These traditional technologies are being used in power systems for a long time, and until recently, it has not seen significant innovation compared to other technologies. The same documentation from ORNL (2013) estimates the magnetic amplifier-based power flow controller (MAPFC)– a variable reactance electromagnetic device with a structure similar to power transformers costs lower than $5/kVA, which is even lower than the most inexpensive FACTS controllers. And it is possible to achieve the functionality of some of the advanced FACTS devices like STATCOM and SSSC with the combination (parallel/series) of variable reactance electromagnetic devices like continuously variable series reactor (CVSR) and capacitors without any voltage source converter (VSC). Therefore, the reactance variation option with reactors for power flow control is viable and needs further investigation.

The focus of the thesis is to explore the non-FACTS-based reactance variation option (electromagnetic devices) for active power flow control with the power inductors. Hence other options for power flow control are not discussed.

A 3-bus example power system is shown in Figure 1.1 to demonstrate the power flow control capabilities of PFCs by controlling their reactance according to (1.1). In figure, a load (100 MW) at bus 3 is fed from a generator at bus 1. There are multiple paths for the power flow: line13 and line123 (line12+line23). All of the lines are considered to have the same power flow capability (MVA limits) and reactance per unit length. However, line13 is the short impedance path compared to the other option. The details of the power system are not shown to keep the model simple. This model has been built using the PowerWorld simulator.

In the base case (Figure 1.1), it can be seen that line13 is overloaded while the power flow through the other parallel line is well below the power flow capability (thermal) limit. It is because more
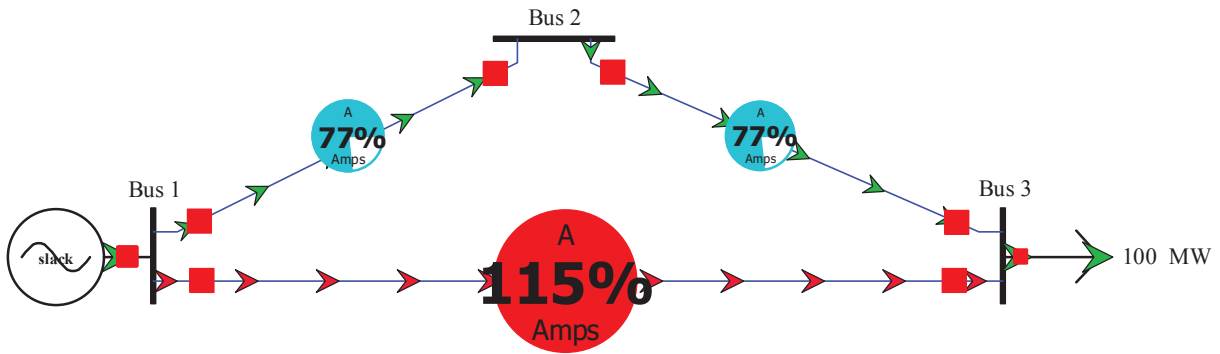
Figure 1.1: Simple 3-bus power system

current flows through the low impedance path, line13. This scenario is undesirable as it can hinder consumer access to lower-cost generation. A PFC is placed in the overloaded line with a series reactance (shown in Figure 1.2) to solve the congestion issue. By doing so, the loadings of all the lines were kept within limits. The additional reactance balances the impedance along both paths to the load in the network, and power flow occurs equally.
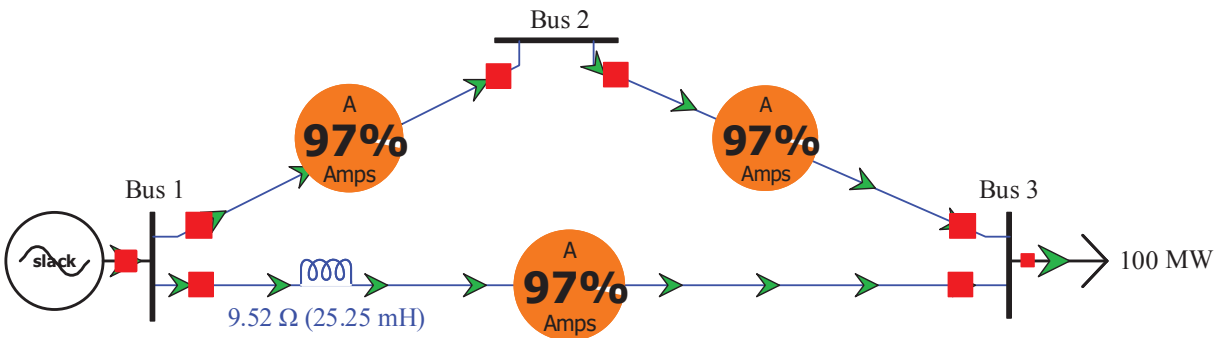
Figure 1.2: Congestion management with PFC with series reactance

A second scenario is considered in Figure 1.3, where bus 3 load is redistributed to a load of 20

MW at bus 2 and 80 MW at bus 3, and the PFC is taken out of service. The resulting power flow is suboptimal as line13 exceeds its power flow limit.
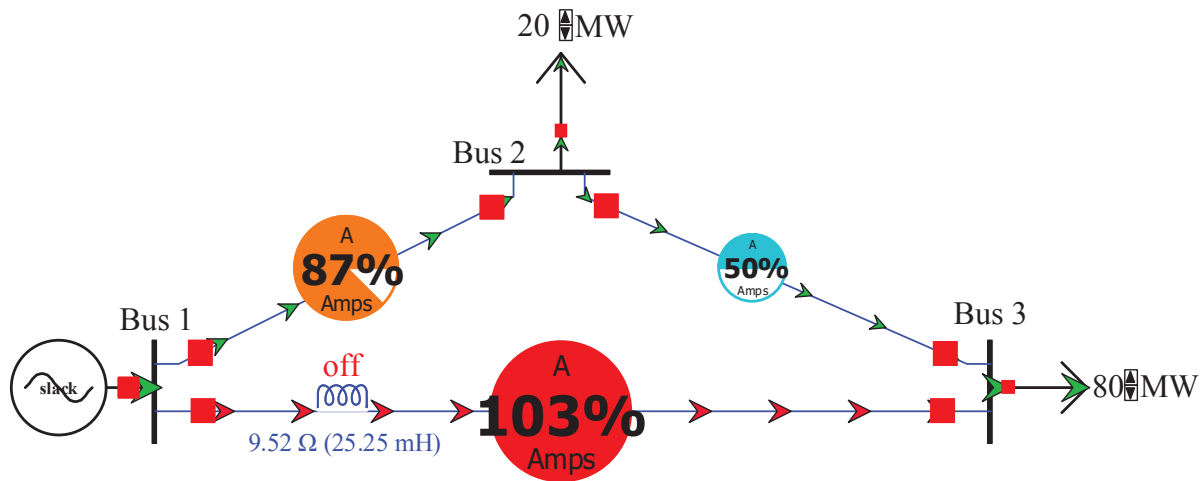
Figure 1.3: Load redistribution in 3-bus power system without series reactor

Then the PFC is brought back to the service, and the resulting power flow is shown in Figure 1.4. Again the power flow is suboptimal, with line12 exceeding its power flow limit.

The congestion issue can be solved simply by reducing the reactance of line13 by taking some reactances offered by PFC out of service. As shown in Figure 1.5, line loadings of all lines are kept within limits while all system loads are supplied.

From the example scenarios presented here, it can be concluded that an optimal power flow (OPF) control can be achieved by changing a line reactance. To this end, it is preferred to have a PFC capable of providing variable reactance.
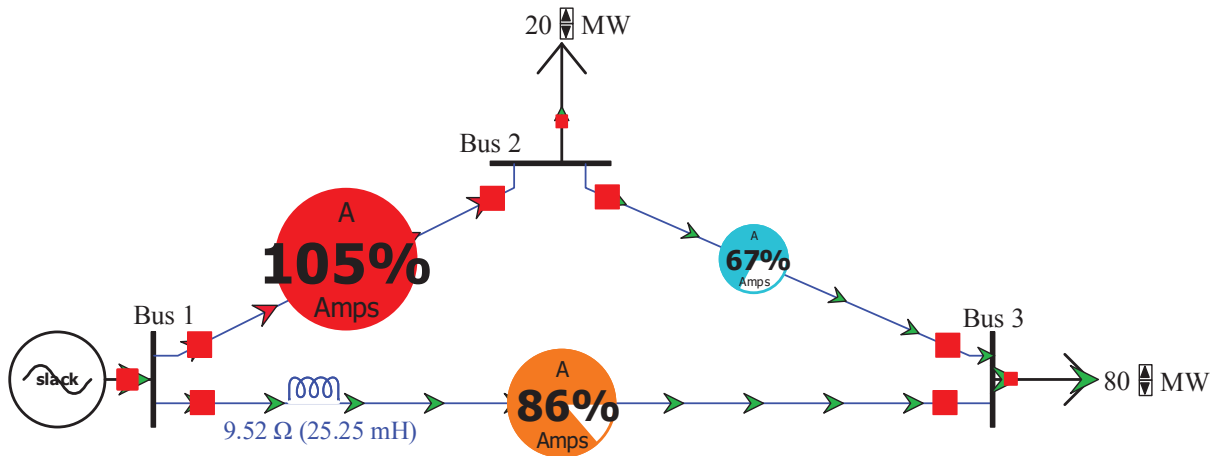
Figure 1.4: Load redistribution in 3-bus power system with series reactor
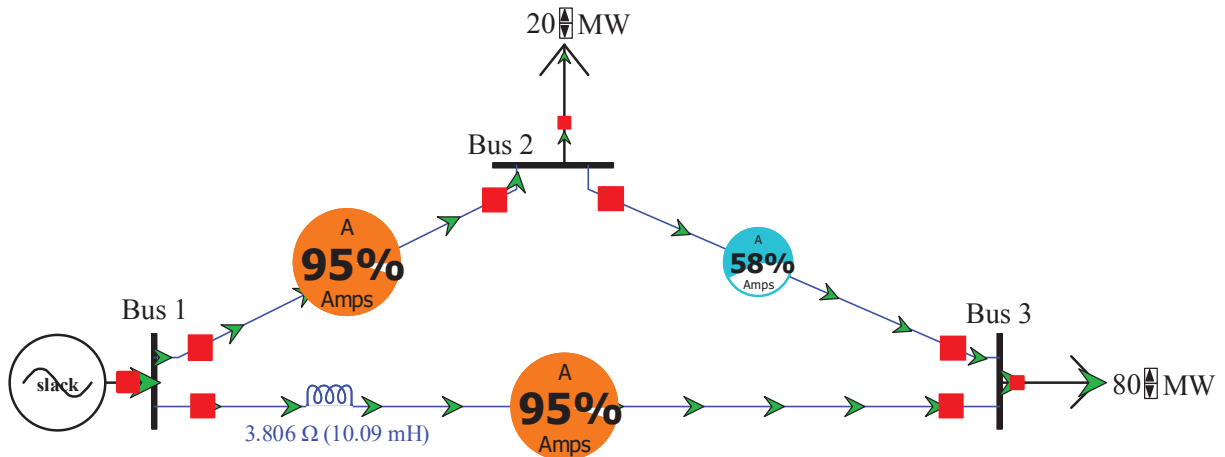
Figure 1.5: Congestion management by keeping some reactance of PFC out of service

Power Reactors

Inductors, commonly referred to as reactors in power engineering, are one of the basic power system elements wildly used in many applications, either as stand-alone devices or as integral compo-

nents in others. They provide some of the simplest yet efficient, robust, and cheap solutions for a wide range of problems in power systems. Compared to reactors, FACTS offer better control and flexibility. However, the converter complexity and semiconductor ratings significantly increases the cost of FACTS devices. Also FACTS devices have low reliability as single component failure can cause overall system to stop working. DFACTS tries to solve some issues with FACTS but faces the problem of requiring complex communication and coordination. Inductors are used in power systems as fault and load current limiters, reactive power compensators, harmonic filters, transient dampers, load balancers, and more. There is a limited number of fixed, series-connected reactors used for power flow control applications [5], [6].

The main reason for the limited use has been the lack of flexibility. Reactor can be a superior alternative to expensive FACTS devices with limited functionality for adequate and optimal control of ac currents in a power system. Based on the application, they can be connected either in series or in shunt with the network. They can further be categorized into dry-type and oil-immersed type depending on the voltage level and power rating. Among the different combinations, the usual practice is to make dry-type reactors with air-cores and oil-immersed types with ferromagnetic cores [7]–[9]. Powdered core reactors, which are manufactured by the compression of the very fine particles of the magnetic materials, are preferred for high-reliability military and space applications because they are robust against shocks, vibrations, and nuclear radiations. Also, flux containment is better in powdered core compared to the ferromagnetic cores [10].

The reactors can be categorized as shown in Figure 1.6 according to relevance to the work presented here.

The air-core reactors are the simplest of all, with only two states, either on or off. In air-core re-actors, the magnetic field is not constrained and occupies the space around it without iron cores. An accurate magnetic field mapping is necessary for magnetic clearance analysis and substation

9
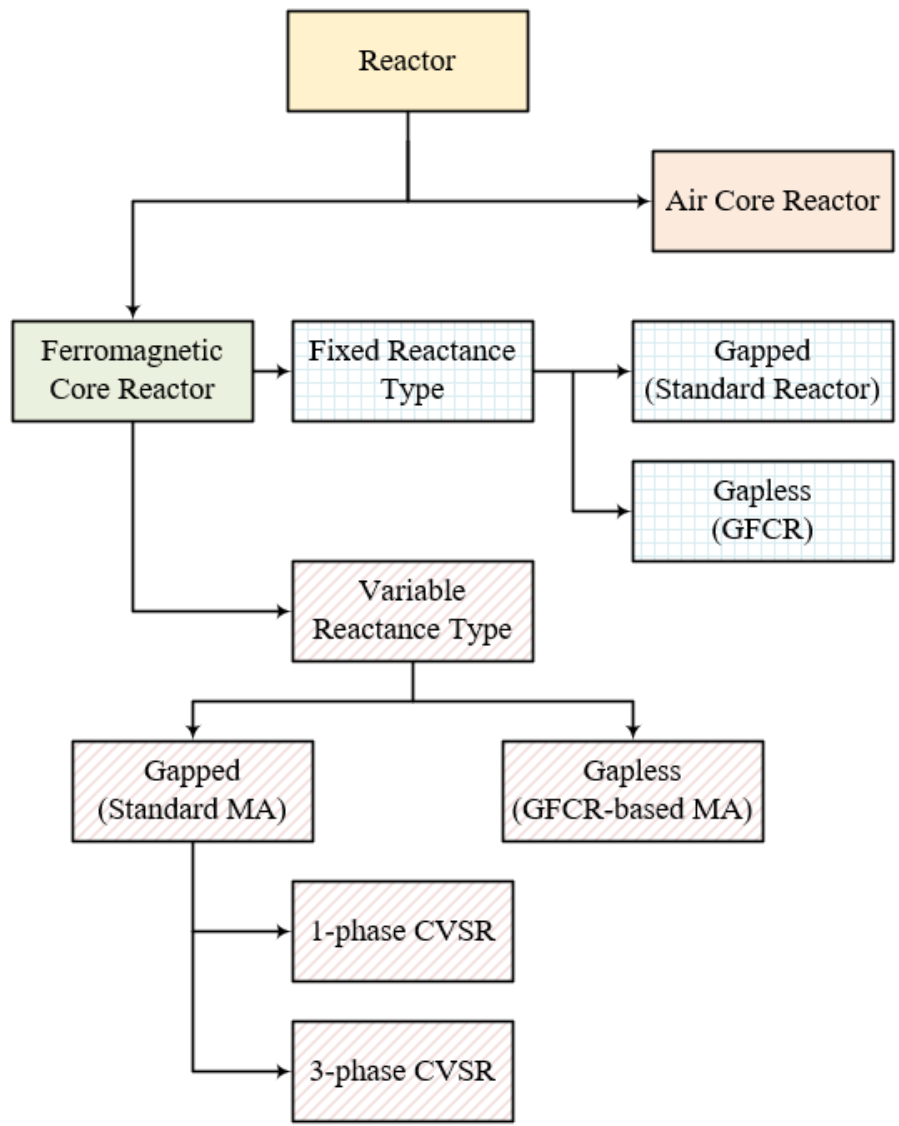
Figure 1.6: Reactor classification

personnel exposure assessment. Great care must be taken to ensure limited eddy current-induced heating in adjacent objects. Also, the effects of the stray magnetic field must be considered in the bus support and reactor structural support [5]. IEEE standard C57.16 [11] describes the requirements, terminology, and test code for dry-type air-core series-connected reactors.

Since the air-core reactors are out of the scope of the work, they will not be discussed throughout the thesis.

Some of the issues of the air-core reactors can be avoided by using a ferromagnetic core. It provides a controlled path for the flux flow. However, its operation is nonlinear. The characteristics of a magnetic material dictate the operation.

The ferromagnetic core reactors can be further divided into fixed reactance and variable reactance type. The fixed reactance type reactors operate in either on or off states offering a single effective reactance. However, the variable reactance type reactor offers the continuous variation of the reactance utilizing some unique bias supplies. The gapped type of reactor is the standard one; it has non-ferromagnetic gaps in its core. Because of the gaps, the reactor produces humming sound and vibration, the utilization of ferromagnetic material is suboptimal, and as a result, the reactor is bigger, expensive, and havier. These issues are avoided with the novel gapless ferromagnetic core reactor (GFCR). It requires a unique connection of the ac windings around the core. Both standard gapped and GFCR offer a constant reactance.

By applying the principles of magnetic amplifier (MA) technology, the reactance of the ferromagnetic core reactors can be made variable. These reactors are also dubbed as continuously variable series reactors (CVSRs). The variable reactance is obtained by the magnetic saturation control of the ferromagnetic core, which is achieved by applying specially arranged bias DC supplies. This technology can be applied to GFCR to produce variable reactance GFCR-based MA. It avoids the issues of air-gap in the core and at the same time produces a variable reactance. The initial design of the MA was for single-phase applications. However, to avoid using a bank of three single-phase CVSRs for three-phase applications, novel three-phase CVSRs are presented here. The three-phase CVSRs are favorable in terms of economics and space requirements.

In combination with other measures, switchable series reactors (fixed or variable) become an at-

tractive power flow control alternative.

Dissertation Overview and Contributions

The remainder of the thesis is organized as follows. A brief review of research studies on the magnetic amplifier (MA) technology, its application in power flow control, and magnetic equivalent circuit (MEC) based analytical approach for an electromagnetic device modeling is provided in chapter 2.

Chapter 3 focuses on the finite element analysis (FEA) based numerical analysis of electromagnetic devices. A commercially available electromagnetic field simulation software is used to perform the FEA simulations of electromagnetic devices presented in this dissertation. This section lays out the detailed steps to carry out such simulations with some theoretical background. It also describes several toolboxes and solution types for various simulation needs.

In the next chapter, a standard ferromagnetic core reactor with an air gap is introduced, followed by its modeling and design optimizations. The fringing permeance around the air gap is introduced to improve the accuracy of the presented model. Later, the analytical model is used to optimize the design of the reactor. Both single objective (SO) and multi-objective (MO) optimization examples are provided to demonstrate the applicability of the proposed model.

Data-driven approaches for magnetic amplifier (MA) characterization are introduced next. Two frameworks are presented for the accurate reactance prediction based on the historical data. In both approaches, the data set is obtained from FEA simulations keeping MA design parameters constant while varying the excitations (AC and DC). In the first framework, the artificial neural network (ANN) is trained with data set to predict the effective MA reactance. In this case, ANN works as a black box without any information about input-output dependencies. In the second framework,

the physics of the MA aids the data-driven approach to accurately predict the reluctance of a simplified MEC, which then gives the accurate analytical method for reactance prediction. The ANN performance matrices support the applicability of the proposed approaches.

Chapter 6 introduces the three-phase variants of the continuously variable series reactor (CVSR) to relieve the overloading of the distribution transformers. With the unique connection of the AC and DC coils, the reactance of CVSR could be changed uniformly for all phases. Two approaches are introduced to control the non-uniform saturation of the cores: heterogenous core material mix with uniform dimensions and homogenous core material with non-uniform dimensions. Analytical models are presented for both of the cases, which are later verified with FEA simulations.

Chapter 7 introduces a novel gapless ferromagnetic core reactor (GFCR). The issues with the air gap in the standard ferromagnetic core reactor are avoided with GFCR. The unique placement and connection of the AC coils give rise to a virtual air gap. An analytical model is presented and validated for the GFCR. Furthermore, the equivalent GFCR reactance variation with the physical distance between AC windings is also analyzed.

The following chapter discusses the potential application of such varying reactance devices in the optimal power system operation problem. The reactance change makes the variable reactor allocation problem a mixed-integer non-linear program (MINLP) even though it is incorporated within a DC optimal power flow. This MINLP form of the problem is an NP-hard problem that is challenging to solve. We propose a new bitwise mixed-integer linear program (MILP) formulation of the reactor allocation problem, free of hard assumptions. The changing susceptance in the system is modeled with parallel branches with adequately selected incremental susceptance values. We comparatively demonstrate this approach with state-of-the-art techniques on a commonly used power system test case, and results are also presented.

The last chapter of this dissertation summarizes the research contributions and future work direc-

tions.

CHAPTER 2: LITERATURE REVIEW

An in-depth review of magnetic amplifier (MA) technology and electromagnetic device analysis techniques are covered in this chapter. The magnetic equivalent circuit (MEC) based analytical method, and finite element analysis (FEA) based numerical method are critiqued. The novel electromagnetic devices discussed throughout the thesis are modeled using MEC and later verified using FEA. A large portion of the thesis is dedicated to the extension of MA-based technology. The three-phase variants of MA are put forward for the first time. Later a MA technology modification is introduced that has improved efficiency for some applications– one of which is discussed in detail. Because of the deductions mentioned above, the topics reviewed in this chapter are relevant.

The traditional fixed reactance type reactors like air-core reactors and gapped ferromagnetic core reactors are well known because of the extensive research and publications in these areas. However, the variable electromagnetic reactors with the aid of control circuits are not common. Therefore, in this chapter, only the special kind of variable series reactor technology is discussed.

Magnetic Amplifier (MA)

Historical Perspective

The magnetic amplifier (MA), also known as the saturable reactor or the transductor, has been around for a long time; C.F. Burgess and B. Frankenfield first introduced it in 1901. However, no consensus can be found about the inception of this technology, as some articles point to the MA application as early as the late 1800s. The use of various forms of DC controlled saturable reactors to regulate the electric circuit was disclosed for the first time in [12]. In the early days,

15

MA was used in electric machinery and in theater lighting. Mainly the technology was used as a static control instrument for rotating equipment. There was a steady increase in the scientific interest towards magnetic amplifier technology, mainly for the applications in low power control, communication, and sensor systems, until the mid of the century [13]. The two World Wars brought this technology to the pinnacle of its development, especially WWII, when used to control gun turrets, gun stabilizers, long-range rocket control systems, auto-pilot systems, missile guidance, and various industrial applications. Because of their little maintenance, rigidness, and ability to handle very high currents, they were also used in computing machines, electric brakes for trucks and locomotives, and high voltage power systems [14], [15]. Even though MA was originated in the USA, the credit for its adoption and development goes to the Germans. German scientists' contributions include improvements in efficiency and response time, reduction in size and weight, and broadening the field of applications made possible by introducing novel rectifiers and improved magnetic material processing. Once solid-state semiconductor technology was developed, it took over almost all applications, and the MA technology fell into oblivion.

Figure 2.1 summarizes the chronological evolution of magnetic amplifier.

Magnetic Amplifier Fundamentals

The MA consists of electric and saturable magnetic circuits so interlinked that an independently applied magnetization controls an ac circuit's reactance. It uses the principle of saturation control with the help of an additional dc control bias supply. This power control device is connected in series with the load to be controlled. The control is achieved by varying the impedance, which increases or decreases the total load. The impedance to the flow of ac is affected by changing the degree of saturation with a relatively low amount of dc through a separate winding on the same core. The independent and simultaneous magnetization of the core by periodically varying and

16
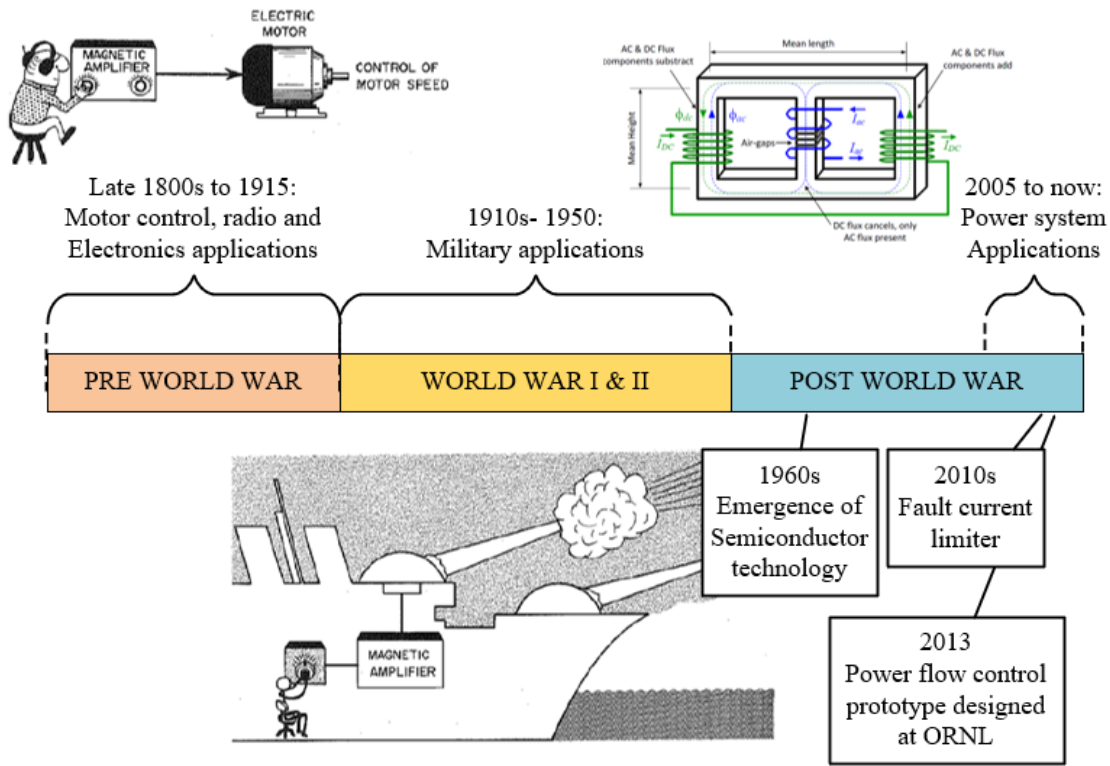
Figure 2.1: Evolution of magnetic amplifier adopted from [15]

unidirectional magnetomotive forces (MMFs) is the working principle of MA[16]. An unsaturated core has a relatively high impedance to ac. In contrast, a saturated core acts effectively as an air core, with practically no impedance. "Technically, it may be described as essentially a device which controls the ac reactance of a coil by controlling the effective permeability of the magnetic material on which the coil is wound" [14]. The use of various forms of DC-controlled saturable reactors to regulate the electric circuit was disclosed for the first time in [12].

A simple saturable core reactor is shown in Figure 2.2. Direct current source, magnetic core with windings, and alternating current source are the essentials of a saturable reactor. The flow of current from a coil wound on a magnetic core can be changed by varying the saturation of the core.
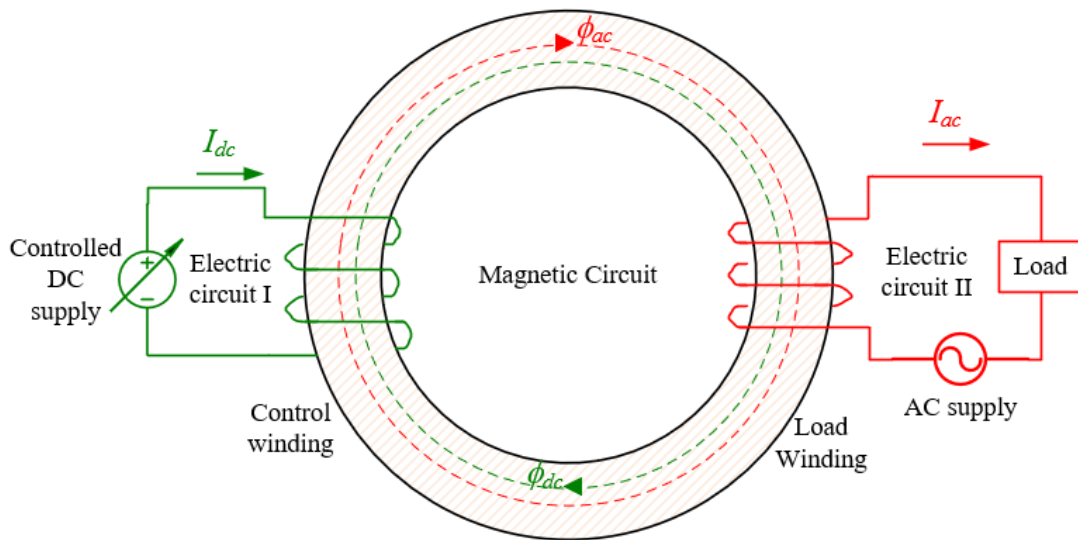
Figure 2.2: Simple saturable reactor adopted from [15]

With the two electric circuits connected by a magnetic circuit, the characteristics of any one of the circuits affect the operation of all the other circuits. A DC in the control loop flows through the control winding with N_1 turns to establish the magnetomotive force F_c. I_{DC} sets up a dc flux in the magnetic circuit loop. This flux is constant in magnitude and direction. In the load loop where the AC source is connected, AC flows through load winding with N_2 turns. Since the current is alternating, the flux set up in the magnetic circuit loop is constantly changing in magnitude and direction. The combination of the fluxes results in cyclical saturation and desaturation of the core. It causes the changing inductive reactance in the load winding. According to the strength of the DC flux, it controls the reactance of the load winding.

The simple saturable reactor operation can be grouped into:

- Zero DC in the control loop: The load winding inductive reactance (X_L) is maximum.

18
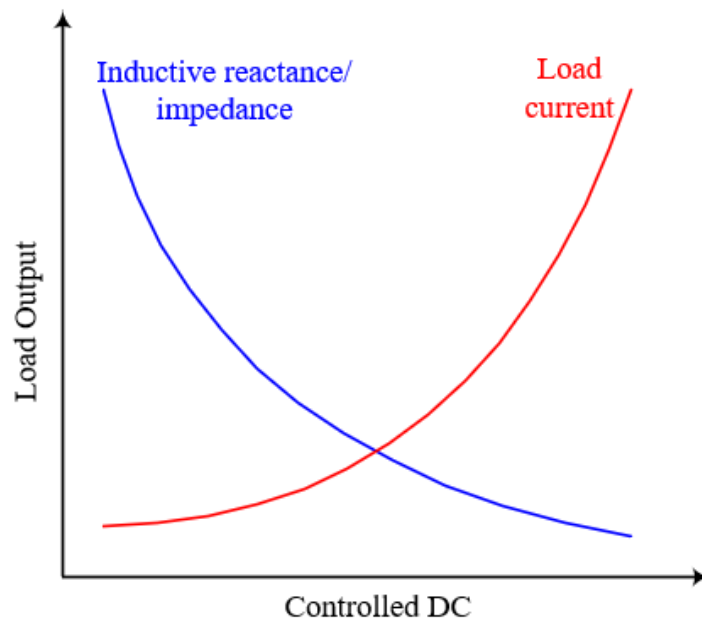
Figure 2.3: Input to output relationship

Therefore the power transferred to the load is minimal.

• Increased DC in control loop: When AC and DC fluxes are superimposed, the collective
result is the saturation of the core. When the core is near saturation or fully saturated, the
inductive reactance is significantly reduced. A large AC is allowed to flow through the load
with the reduced reactance resulting in maximum power transfer.

The operation of the saturable reactor is graphically shown in Figure 2.3.

The advantages of magnetic amplifiers are [15]:

1. Stepless uniform control without interrupting power in the main circuit

2. Rugged: can withstand extreme heat, dust, moisture

3. High power gain: large amount of power can be controlled by small amount of DC power

4. Low noise

5. High efficiency with low internal power loss

6. Low cost

7. High reliability

8. Low maintenance

Some disadvantages of magnetic amplifiers are [15]:

1. Stability: additional stabilizing circuits are generally required

2. Impedance range: impedance can not be increased to infinity or decreased to zero

3. Sensitivity and distortion: the output of magnetic amplifier can be a highly distorted wave-form, resulting in harmonics issues

A simple schematic of a more common single-phase MA configuration with a multi-legged, gapped ferromagnetic core is shown in Figure 2.4. It has a symmetrical design with three ferromagnetic legs: outer legs are gapless while the central leg is gapped. The air gap is in the middle of the central leg, underneath the AC winding, which is connected to the AC circuit.

The MA core is made up of the material with high permeability that acts as a perfect conductor for magnetic flux. A MA configuration differs from a single-phase ferromagnetic inductor by the DC bias windings on the outer legs. In the two bias windings, the controlled DC is supplied so that there is constant flux flow on the external structure of the reactor. The interaction of the AC (red) and DC (black) flux guarantees the continuous variation of the reactor impedance. For each
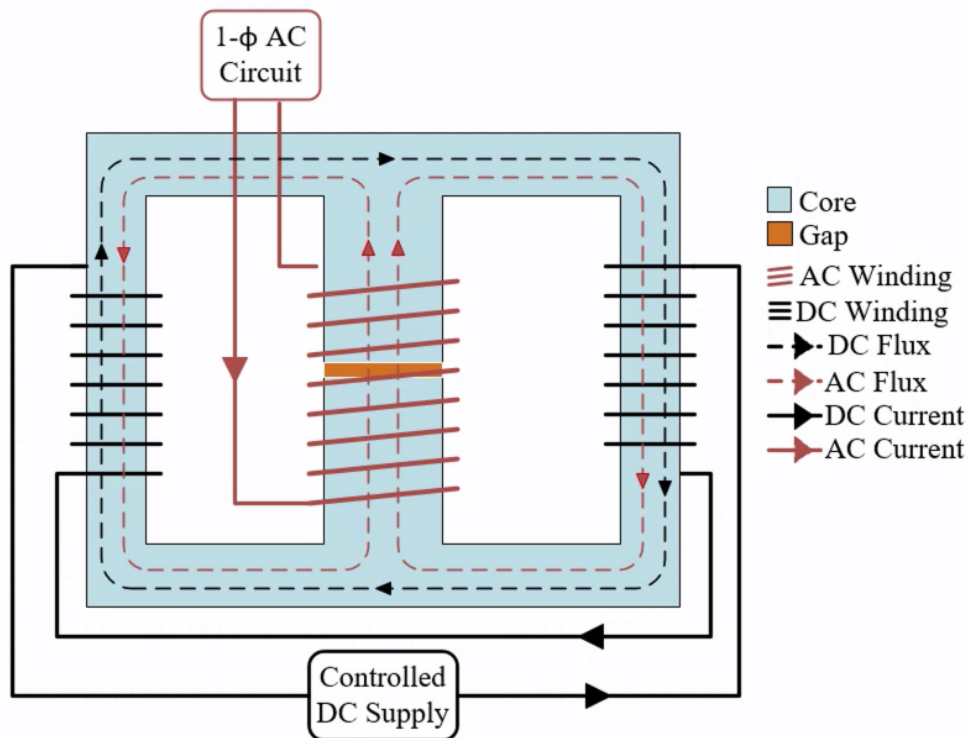
Figure 2.4: Magnetic amplifier configuration adopted from [17]

half-cycle of AC supply, AC and DC fluxes are in the same direction in one of the outer legs and opposite in the other. It causes one leg to be more saturated than the other. With high DC bias, the compound effect is that the effective reluctance of MA gets increased while the AC reactance decreases. For simplicity, the ferromagnetic core has been considered solid, while it is always laminated in practice to reduce the core loss. Similarly, the aggregation of the non-ferromagnetic material gaps has been represented by a single air gap.

Power System Applications

Recently MA technology is being researched worldwide for their future commercial application in the power system. [18] summarizes the applications of a saturable core reactor (SCR) in the power system. One of the more comprehensive research and development (R&D) projects involving SCR in the power system has been the fault current limiter (FCL). The recent development in the power electronics and high-temperature superconductor (HTS) technology has helped tremendously to realize this application. FCL changes the impedance non-linearly between low and high values. The reactance of the FCL is directly proportional to the relative permeability of the core used and the slope of the nonlinear steel characteristics. The nominal operation of the FCL is in the saturation region, where the impedance is minimal. The fault current through the AC winding takes the core out of the saturation to the linear region increasing the impedance of FCL [19]–[23]. FCL in the electrical transmission and distributions system for the transient and steady-state is investigated in [24] with bias provided through Ag-clad HTS winding. Furthermore, [23] provides an insight into the development and testing of a compact saturable core HTS FCL for application in transmission networks. It introduces a unique three-phase FCL structure with a single cryostat containing the HTS DC bias and six ac coils located on the outer limbs of the iron core spaced equidistantly.

In [25]–[27], Dimitrovski, et al. introduce the application of the SCR technology for the power flow control, their impact on distance protection, and SCR optimal allocation for transmission system expansion planning. [28] further investigates the application of MA-based power flow controller (MAPFC) to suppress inter-area oscillation and improve system stability of an interconnected power system. SCR is superior to the flexible AC transmission system (FACTS) in terms of cost and durability for the application in the meshed power systems. More exotic designs of the three-phase continuously variable series reactor (CVSR) arrangements have recently been put

22

forward in [8], [29] for the application in distribution systems.

Apart from the applications mentioned above, the MA technology has potential in various electrical system applications. For wireless power transfer (WPT) based on magnetic resonant technology, applicable for electric vehicle (EV) battery charging, two SCRs can change the operating and resonant frequency of the transmission and reception circuits, respectively, to allow high-efficiency energy transfer [30]. An SCR-based adjustable reactor is an attractive option for arc-quenching in the presence of fault current [31]. The SCR-based power supply of electronic flight control systems is considered attractive technology in more electric aircraft (MEA) systems due to the possibility of achieving compact, robust, and highly reliable design [32]. Reactors based on the principles of MA like magnetic controllable reactors (MCRs) and controllable reactors of transformer type (CRTs) are considered superior to the conventional methods for reactive power compensation of high voltage long-distance transmission lines [33].

Electromagnetic Device Modeling Techniques

The prevalent methods applicable for the detailed analysis of an electromagnetic device can be categorized into the following.

Numerical Methods

The finite element analysis (FEA) is the most accurate tool for calculating the complicated flux flow within the device, especially with multiple excitations. The need for high computational resources (time and cost) and the lack of closed-form solutions are the main drawbacks of the FEA method. Even though the computational resource need has been reducing significantly in recent times, it is still not considered convenient for automated design and optimization [34]–[36]. Therefore FEA

23

can be used to validate other methods with less computational requirements. And the combination of FEA with other methods can result in a better understanding of the system and may give rise to novel analysis techniques. A field-circuit modeling method for multi-stage saturable magnetically controlled reactor (MCR) is proposed in [37], which combines the detailed electromagnetic field simulation (FEA) with external systems through dynamic model creation. However, this method's simulation time depends on the field simulation, which requires high computation resources. The communication step between the field simulation and the external circuit must be small enough to generate better results. Also, it faces convergence issues and significant cumulative errors.

Magnetic Equivalent Circuit (MEC) based Analytical Method

The magnetic equivalent circuit (MEC) is an analytical approach for analyzing a power magnetic device based on design inputs, geometry, and material specifications. In a semi-automated design process, MEC can serve as a valid starting point and they are preferred method [38]. Among different analytical approaches, the MEC-based approach is straightforward for equivalent inductance calculation of magnetic devices. The moderate computational effort, acceptable accuracy, and flexibility in the design of MEC makes it a good compromise solution for design purposes between the FEA and lumped electrical parameter models based on empirical expressions [39]. However, it's a coarse approximation technique that requires a significant level of engineering judgment and a considerable amount of problem understanding to achieve accurate results [40]–[42]. It represents a magnetic device as the combination of magnetomotive forces (MMFs) representing windings and lumped reluctances representing both linear and nonlinear flux flow paths.

CHAPTER 3: METHODOLOGY

Magnetic Ohm's Law

The magnetic Ohm's law relates the magnetomotive force (MMF) drop and the flux flow. To establish the relationship, let us consider a magnetic material (cylindrical) as shown in Figure 3.1. In the figure, the MMF drop across the length of material is F, while the flux flow through the material is Φ. The length of the material is l, and the area of a uniform cross-section material is A. It is assumed that there is no flux leaving along the length of the material, which means the flux can enter and leave the material through the end cross-sections only.
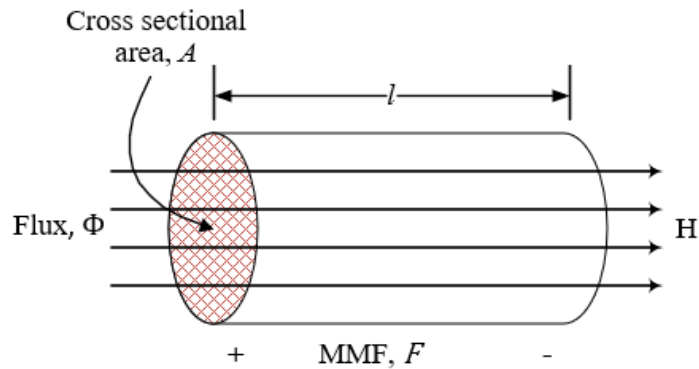
Figure 3.1: Fields in a magnetic core piece

Considering the field intensity to be uniform, then the MMF drop across the material can be expressed as

$$F = Hl \tag{3.1}$$

Here H is the field intensity in the indicated direction. Assuming the flux density B is uniform, the flux into the surface may be expressed as

$$\Phi = BA \qquad (3.2)$$

From (3.1) and (3.2),

$$F = R\Phi \qquad (3.3)$$

Here R is the reluctance of the material, which can be expressed as

$$R = \frac{l}{\mu A} \qquad (3.4)$$

where μ is the permeability of the material.

Alternatively, the equivalent relations to (3.3) and (3.4) can be given by (3.5) and (3.6) respectively.

$$\Phi = PF \qquad (3.5)$$

where P is referred to as the permeance of the material, which can be expressed as

$$P = \frac{A\mu}{l} \qquad (3.6)$$

Magnetic Equivalent Circuit (MEC) Construction

The first step in MEC formation is to select node locations that break the circuit into regions that may be treated as lumped reluctance or permeance (linear/nonlinear). There is no unique choice for nodes; however, a tradeoff exists between the number of nodes and the accuracy of the representation. Then the nodes are connected with the circuit elements representing reluctance and MMF sources [43]. These circuit elements are described below.

Magnetomotive force (MMF)

In MEC, the current flowing through the coils is represented by the MMF source. For a coil with N number of turns with i current flowing through it, the corresponding MMF source in MEC is the multiplication of two quantities.

$$F = Ni \qquad (3.7)$$

Reluctances

Core-Piece Reluctance

These are the reluctances corresponding to the magnetically nonlinear material pieces. The nonlinearity comes from the magnetization characteristics (B-H curve) of the core material. While using the magnetic Ohm's law, (3.4), for core piece reluctance calculation, the length and the cross-section of the element are given as the parameters. However, absolute permeability is a nonlinear function, and it requires a nonlinear solution technique.

The complexity of describing magnetic characteristic for the ferromagnetic material, the relationship between the magnetic flux density (B) and the magnetic field intensity (H), can be reduced by ignoring the hysteresis effect. The characterization of non-linearity of the anhysteretic B-H curve is among the key factors in calculating the reluctances of the ferromagnetic branches.

In the absence of a magnetic material, the relation between flux density B and field intensity H is

$$B = \mu_0 H \tag{3.8}$$

where μ_0 is the permeability of free space ($4\pi \times 10^{-7}$ Henries/meter).

However, the relation between B and H in the presence of magnetic material is:

$$B = \mu H \tag{3.9}$$

In (3.9), μ is total magnetic permeability, which can be expressed as:

$$\mu = \mu_0 \mu_r \tag{3.10}$$

Here μ_r is the relative permeability. One approach to express the non linear characteristics of a magnetic material is to express permeability as a function of either B or H with some permeability function parameters. The former is preferred when MEC is formulated in terms of mesh equations. In MEC, to indicate the nonlinear nature of core-piece reluctance, they are often represented as a function of flux flowing through them. So that the reluctance expression for a core-piece i with length l_i and cross-sectional area A_i becomes

$$R_i(\phi_i) = \frac{l_i}{\mu_B(B_i)A_i} \tag{3.11}$$

The process to find the permeability as a function of respective flux densities is described in [43] and summarized in [9] by (3.12) and (3.13). This branch linearization procedure is a part of the iterative circuit solution, which will be discussed later.

$$\mu_B(B) = \mu_0 \frac{X(B)}{X(B) - 1} \tag{3.12}$$

where,

$$X(B) = \frac{\mu_r}{1 - \mu_r} + \sum_{k=1}^{K} \left\{ \alpha_k |B| + \frac{\alpha_k}{\beta_k} log \left(\frac{e^{-\beta_k \gamma_k} + e^{-\beta_k |B|}}{1 + e^{-\beta_k \gamma_k}} \right) \right\} \tag{3.13}$$

Here α, β and γ are the permeability function parameters and k is the index for magnetic function parameters. The function parameters are found experimentally and are available for several materials in [44]. Due to the varying nature of the permeability, the magnetic analogy deviates from its electric counterpart and requires special attention during calculations [45].

Leakage Reluctance

In a magnetic circuit, the flux that flows outside of the intended path or the flux that does not have its complete path within the core is known as the leakage flux [43], [46]. The flow of the

flux outside of the ferromagnetic core is mainly due to the relatively small (order of thousands) permeability difference between the core and the non-ferromagnetic medium (air). In an electric circuit, the conductance difference between the conductor and the external environment is normally very large. Therefore, the issue of leakage electric current is almost nonexistent in electric systems. This is not the case with magnetic circuits.

The leakage reluctances are assumed to be independent of the fluxes through them and constant, as are the air-gap reluctances. Calculations of the former start with finding the corresponding permeances first and then reciprocating them to obtain the reluctances. Therefore, R_x and P_x are used in the sequel to indicate the reluctance and the permeance of element x of the MEC, respectively.

The inherent assumptions associated with the leakage reluctance calculation are:

1. The MMF drops across all the portions of the path in the the core material is insignificant because the permeance of the core is very high compared to the permeance of the air;

2. The magnetic field intensity along the leakage paths is constant.

The reluctances are calculated by, first, finding permeances using energy equations in magnetically linear systems. The energy stored in a magnetically linear inductor can be expressed as:

$$E = \frac{1}{2} P_l N^2 i^2 \tag{3.14}$$

Here, P_l is the leakage permeance.

On the other hand, the energy stored in a linear magnetic material and spatially varying fields is

given with:

$$E = \frac{1}{2}\mu_0 \int_V H^2 dV \tag{3.15}$$

where μ_0 is the permeability of free space and dV is volumetric integration variable over the volume of the leakage path. From (3.14) and (3.15), the permeance is found to be:

$$P_l = \frac{\mu_0}{(Ni)^2} \int_V H^2 dV \tag{3.16}$$

While calculating leakage permeance of equation (3.16), the flux intensity (H) calculation is based on Maxwell's fourth equation (Ampere's law). This equation relates the electric current following in the coil and the magnetic field wrapping around it. The ampere's law can be given by either (3.17) or (3.18).

$$\nabla \times H = \frac{\partial D}{\partial t} + J \tag{3.17}$$

$$\oint H.dl = I_{enclosed} \tag{3.18}$$

In (3.17), D is electric charge density and J is current density. And in (3.18), $I_{enclosed}$ is the total current inside the closed loop.

MEC Solution

A meshed circuit analysis based on Kirchhoff's laws from electric circuits can be adopted to solve the proposed MEC once each MEC element is determined. In mesh analysis, a system of equations in the form of (3.19) is solved.

$$R_N \Phi_N = F_N \tag{3.19}$$

Here, $R_N \in \mathbb{R}^{N_m \times N_m}$ is the network reluctance matrix, $F_N \in \mathbb{R}^{N_m}$ is the MMF matrix, and $\Phi_N \in \mathbb{R}^{N_m}$ is the vector of loop fluxes, where N_m is the number of mesh equations. Once the individual reluctance is computed, the network reluctance matrix is formed with the help of the loop incidence matrix (T). The solution of the mesh analysis is the loop fluxes, which can be converted easily into branch fluxes [8].
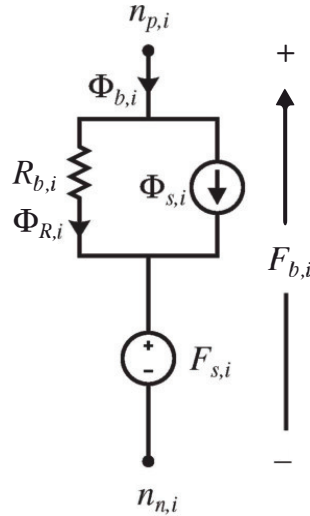
Figure 3.2: Standard branch adopted from [43]

32

Standardization of each branch that connects two nodes is beneficial in magnetic circuit solutions. A standard general branch used for the meshed circuit analysis is shown in Figure 3.2. In figure, $\Phi_{b,i}$ denotes the flux going through the branch connecting $n_{p,i}$ and $n_{n,i}$, $\Phi_{s,i}$ indicates flux source, $R_{b,i}$ is the reluctance, and flux through it is $\Phi_{R,i}$. MMF source represents the winding, and flux source represents a permanent magnetic material.

Therefore the MMF drop across the branch can be given by:

$$F_{b,i} = R_{b,i}(\Phi_{b,i} - \Phi_{s,i}) - F_{s,i} \tag{3.20}$$

The electromagnetic devices discussed throughout the thesis do not contain permanent magnet materials; therefore, the flux source component can be omitted.

Since the reluctance matrix contains both linear and nonlinear components, a nonlinear iterative mesh analysis technique is adopted. The flowchart in Figure 3.3 summarizes the iterative steps. It uses a version of Newton-Raphson algorithm for the system of mesh equation solution.

The iterative process starts with the initializations for each of the MEC branch's flux densities (usually $B_i = 0$), error, and iteration limits. Through this process, the branch fluxes and flux densities are updated continuously. Here, the relative error between the branch fluxes between two consecutive iterations and the number of iterations are the stopping criteria for the iteration, except for the first iteration. For each iteration, the permeability is continuously updated for nonlinear components, and based on that, the reluctances are calculated. After reluctance calculation, the mesh equations are solved to find out the loop and branch fluxes and based on stopping criteria, branch flux densities are updated again.

Start

Initialization — Flux density $(B_i)= 0$, Error $=0$, Define Iteration limit

Is iteration $=1$ or (Error> 0 & iteration $<$ iteration limit) ?

NO → Output R_i → Stop

YES

$\mu_B(B)$ Calculation — Using (3.12) and (3.13)

Branch Reluctance (R_i) Calculation — Using $\mu_B(B)$ in (3.11)

Branch Standarization — Format:

Node P — F_s — R_b — Node N

Mesh Analysis — Solve for branch fluxes $F = R\Phi_b$

Calculate error, e & update iteration — $e = K\,|\Phi_b(k+1) - \Phi_b(k)|$
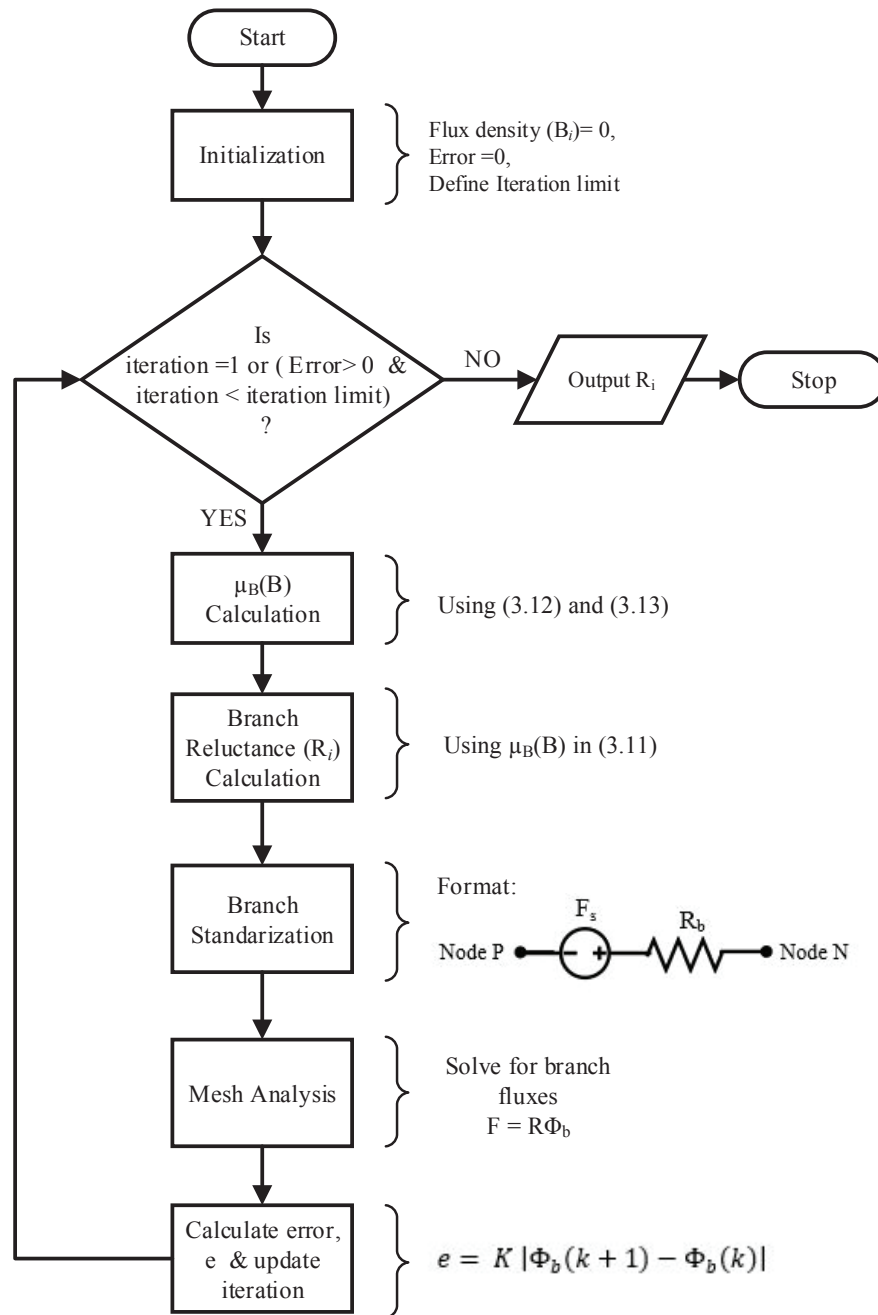
Figure 3.3: Iterative non-linear reluctance calculation flowchart

Equivalent Inductance Calculation

The inductance of the reactor describes the nature of the device and possible applications associated with it and, as such, it can be used for model validation. The inductance indicates the relationship between the flux linkage (λ) and the current (i) in the winding of a magnetic device. The apparent and incremental inductance are both used to describe that relationship. The apparent inductance (L_{app}) is the slope of the line connecting the operating point to the origin, while incremental inductance (L_{inc}) is the slope of the line tangent to the curve at the operating position in flux linkage versus current curve [29], as described in Figure 3.4 and (3.21).
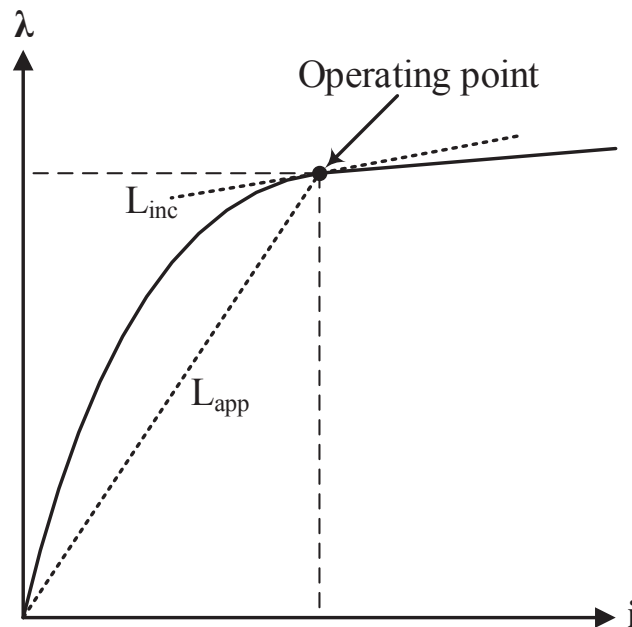
Figure 3.4: Current vs. Flux linkage

$$L_{app} = \frac{\lambda}{i} \tag{3.21a}$$

$$L_{inc} = \frac{\mathrm{d}\lambda}{\mathrm{d}i} \tag{3.21b}$$

Generally, the apparent inductance is higher than the incremental inductance. But for a magnetically linear system, both of the inductances are the same. For a multi-winding magnetic non-linear system, the differential inductance is used for more precise analysis [43].

In an MEC, if ϕ_i is the flux through branch i, and R_i is the reluctance of that branch, the total energy dissipated within the whole circuit is:

$$E = \frac{1}{2} \sum_{i=1}^{n} \phi_i^2 R_i \tag{3.22}$$

where n is the total number of branches in the MEC. The energy stored in an inductor based on the current and voltage relationship is:

$$E = \frac{1}{2} L i^2 \tag{3.23}$$

Using the energy conservation between (3.22) and (3.23), the inductance of a magnetically linear system is found to be:

36

$$L = \frac{1}{i^2} \sum_{i=1}^{n} \phi_i^2 R_i \tag{3.24}$$

In (3.24), L indicates the inductance. Also, if the MEC can be simplified to a Thevenin equivalent circuit with one MMF source and an equivalent reluctance ($\mathcal{R}_{eq}$), then the inductance can be expressed as:

$$L = \frac{N^2}{\mathcal{R}_{eq}} \tag{3.25}$$

For a device with multiple windings, the equivalent inductance must consider the self and mutual inductances, which relate to how excitation supplied to a winding causes the voltage to be induced at the same and another winding, respectively.

MEC Validation

The inductance of an electromagnetic device can be calculated using a proposed MEC and the FEA method for the full range of excitation variations. The comparison of inductance values from both approaches is used to validate any proposed MEC throughout the thesis with the help of a representative case study. The relative error between the inductance values obtained using MEC and 3-D FEA serves as a criterion for the proposed model's validity.

Reactance Calculation

For a 60 Hz system, an reactor's inductive reactance can be expressed as:

$$X_L = 120\pi L \tag{3.26}$$

Electromagnetic Device FEA Modeling

Introduction to FEA

The finite element method (FEM) or finite element analysis (FEA) is a numerical method for solving engineering and mathematical physics problems. Typical areas of interest include structural analysis, heat transfer, fluid flow, mass transport, and electromagnetic potential. The FEM has its origin in the field of structural analysis. Only after 1968, the use of this method for electromagnetic problems was started.

Governing equations and boundary conditions can express many engineering phenomena. Usually, they are called boundary value problems. The governing equations are often partial differential equations (PDEs) or ordinary differential equations (ODEs). FEA is a numerical method used for solving a set of related differential equations by approximating continuous field variables as a set of field variables at discrete points (nodes). Generally, the variational technique or weighted residual technique is used to convert the governing equations into an integral form.

In FEA, the first step is dividing the entire domain into many small, simple elements. Over a typical element, a suitable approximation is chosen for the primary variable of the problem using interpolation functions or shape functions. Usually, polynomials are chosen as the shape functions.

Only a finite number of elements and an expression with only a finite number of terms are used to make the problem tractable. Therefore the FEA solutions are always approximate.

In the next step, the approximation for the primary variable is substituted into the integral form. If the integral form is of variational type, it is minimized to get the algebraic equations for the unknown nodal values of the primary variable. If the integral form is of the weighted residual type, it is set to zero to obtain the algebraic equations. In each case, the algebraic equations are obtained element wise first (called the element equations), and then they are assembled over all the elements to obtain the algebraic equations for the whole domain (called the global equations). The adjacent elements have to share the same degree of freedom at connecting nodes to achieve compatibility. By connecting elements, the field variable becomes interpolated over the entire domain in a piecewise fashion.

Advantages

The advantages of using FEA are:

(a) Can solve analytically intractable problems.

(b) The software enables a user to solve complex problems without detailed knowledge of math and physics behind the problem.

(c) The FEA more naturally accounts for inhomogeneity in problems.

(d) Can work with very complex geometries.

(e) Boundary conditions can very quickly be imposed in a FEA.

(f) The systematic generality of the method makes it a versatile tool for a wide range of problems.

Disadvantages

However, the FEA also has some disadvantages, which are:

(a) For some non-linear problems, the FEA technique is prone to convergence issues.

(b) In some scenarios, the solutions obtained from the FEA can be less accurate than the solutions obtained from other techniques.

(c) Due to many equations, the computational speed and computational power requirements are worse than other techniques.

(d) Being a numerical method, it does not give the functional relationship between the inputs, parameters, and outputs of the system/device. Hence, other solutions are required to see various dependencies needed to improve or optimize the design.

The mathematical foundation behind FEA can be described with the following steps:

1. Discretization/ Mesh generation/ Grid generation: A significant problem solution region is subdivided into smaller, simpler, non-overlapping parts called finite elements. The shape of those elements could be different to minimize the difference between the actual boundary area and the total boundary covered by all the elements. The subdivision of a whole domain into simpler parts has several advantages, including: (i) accurate representation of complex geometry, (ii) inclusion of dissimilar material properties, (iii) straightforward representation of the total solution, and (iv) capture of local effects.

2. Element solution: Some simple governing equations are applied to find the selected entity solutions for each element.

3. Elements assembling: Next step is to assemble all the elements in the solution region creating a more extensive system of equations that model the entire problem. The selected entity's distribution is considered continuous across inter-element boundaries.

4. Solving the resulting equations: Once all the elements are assembled, the resulting system is solved with inter-element relationships preserved.

Solution Steps

The major steps while performing electromagnetic analysis using a commercial electromagnetic field analysis software based on FEA are:

(A) Model creation: A two-dimensional (2-D) or three-dimensional (3-D) model of the device of interest can be created according to the accuracy need and computational resources available, with the former being less accurate and computationally intensive than the latter. All the electromagnetic systems elements are modeled, including the core, coils, and region around them with their characteristics.

(B) Boundary definition: This step creates the boundary between each element and defines the entire system region where the solution is needed. The boundaries can be different, including insulating, symmetry, master/slave, and more.

(C) Mesh creation: The system under consideration is divided into small elements. It is possible to perform the divisions for each element based on its structure complexity, size, and influence on the solution. Based on the solution type, the adaptive meshing of the system could be generated automatically.

(D) Excitation definition: The sources of flux creation within the system is defined here. They can be of current type, voltage type, or external type that allows the system to be connected

with another system. Depending on the solution type selected, the excitations could be static or dynamic.

(E) Analysis setup: It is an essential step that controls design settings (apparent or incremental inductance), dynamic setup (step and stop time), solver types, number of passes, convergence standard, and more.

Software Utilized

The following software tools are used for the works presented in the dissertation.

(i) MATLAB[1] for iterative MEC solution implementation.

(ii) MATLAB based toolboxes:

    (a) YALMIP[2] toolbox for reactor design optimization,

    (b) Genetic Optimization System Engineering Toolbox (GOSET)[3] for multi-objective design optimization,

    (c) MATPOWER[4] for power system simulation and optimization,

    (d) Deep Learning Toolbox[5] for artificial neural network (ANN) implementation.

(iii) ANSYS Maxwell[6] for electromagnetic field simulation of power magnetic devices.

---

[1] https://www.mathworks.com/products/matlab.html

[2] https://yalmip.github.io/

[3] https://engineering.purdue.edu/ECE/Research/Areas/PES/Software/genetic-optimization-toolbox-2.6

[4] https://matpower.org/

[5] https://www.mathworks.com/products/deep-learning.html

[6] https://www.ansys.com/products/electronics/ansys-maxwell

(iv) Symbolic computation software, Wolfram Mathematica®[7] for an approximate analytical expression derivation.

(v) Pyomo[8]–Python based optimization modeling language for optimal power flow implementation.

(vi) Power World Simulator[9] for a power system visual representation.

---

[7]https://www.wolfram.com/mathematica/

[8]http://www.pyomo.org/

[9]https://www.powerworld.com

CHAPTER 4: SPECIAL FERROMAGNETIC CORE REACTOR MODELING AND DESIGN OPTIMIZATION

This chapter is based on the following published works:

S. Pokharel and A. Dimitrovski, "Analytical Modeling of A Ferromagnetic Core Reactor," in *IEEE PES North American Power Symposium (NAPS)*, Wichita, KS, Oct. 2019;

S. Pokharel and A. Dimitrovski, "Ferromagnetic Core Reactor Modeling and Design Optimization," in *Advances in Science, Technology and Engineering Systems Journal*, vol. 6, no. 1, pp. 810-818 (2021).

Introduction

A simple schematic of a special single-phase $(1 - \Phi)$ ferromagnetic core reactor derived from a standard three-phase ferromagnetic core reactor (shown in Figure 4.1) for use in power systems is shown in Figure 4.2. Removal of non-ferromagnetic gaps and the windings from the outer legs of the three-phase reactor converts it into a unique single-phase reactor.

In the Figure 4.2, the black arrow represents the current (I_{ac}) direction, red arrows indicate the flux (ϕ_{ac}) flow and ac winding has N_{ac} turns.

The reactor has symmetrical design with air gaps in the middle of the central core leg, underneath the AC winding connected in series with the ac circuit. The core of ferromagnetic reactor is made of material with high permeability that acts as a very good conductor for magnetic flux. The permeability of the magnetic core dictates its ability to conduct and concentrate the flow of the magnetic flux and, consequently, the inductance of the reactors. As is well known, the relationship between the flux flow within the ferromagnetic core and the current flow in the winding
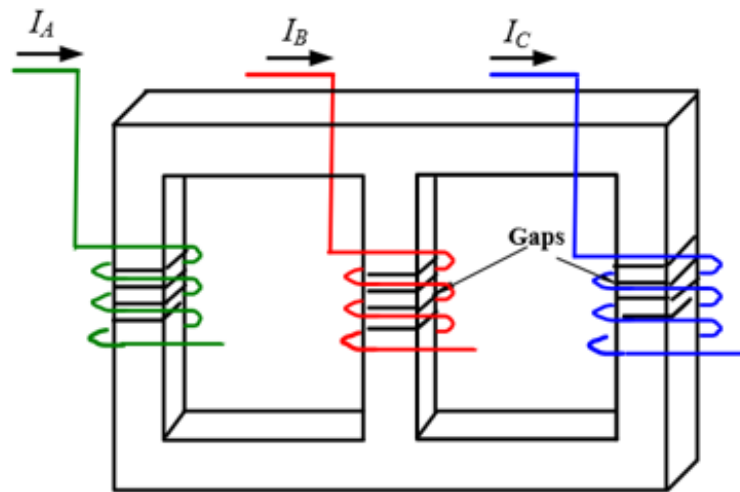
Figure 4.1: Standard three-phase ferromagnetic core reactor
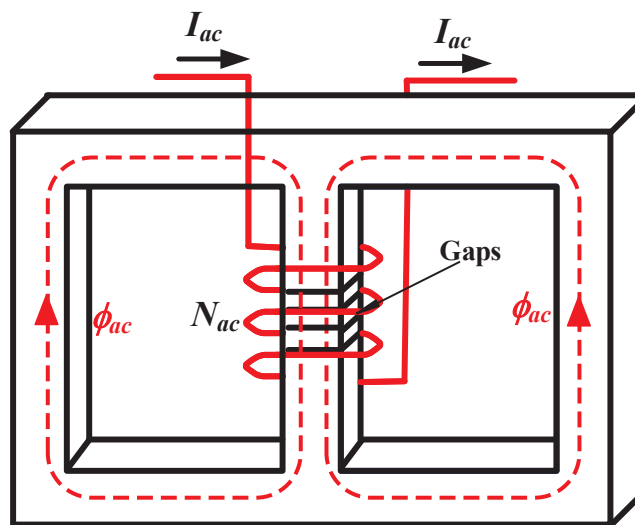
Figure 4.2: Special single-phase ferromagnetic core reactor

of an electromagnet is nonlinear: the rate of change of the flux with the increase of the field strength changes from modest, at the very beginning, to rapid in the operating region, to low

when the core is saturated. After saturation, further increase of current generates a minuscule increase in flux. Generally, operation of power magnetic devices in the saturation region is not recommended because of the increased losses and possible hazardous conditions due to much increased magnetization current.

A laminated ferromagnetic core is used to reduce core losses to a significant extent. It is also a common practice to put non-ferromagnetic gaps in the ferromagnetic core with magnetic properties just like free space to prevent the reactor from saturation from normal operating currents. With air-gaps, the effective permeability of the core and, consequently, the inductance of the device is reduced. But the presence of the dominant reluctance in the magnetic circuit improves the usable range of operation in the power system. The air gaps play a vital role in making the flux less sensitive to environmental changes like temperature. The reactor designer needs to select an adequate air-gap length which will strike a balance between avoiding saturation and the imposed constraints, in order to achieve the desired value of the inductance [9].

The main contributions of this chapter are:

1. An analytical model for a special single-phase ferromagnetic core reactor is proposed and validated.

2. The accuracy of the proposed model is improved by including the fringing flux effect.

3. Design optimization problems (single objective and multi-objective) are formulated and solved by applying the presented model.

MEC based Analytical Model

The front view of a simple gapped inductor with its dimensions is shown in Figure 4.3.
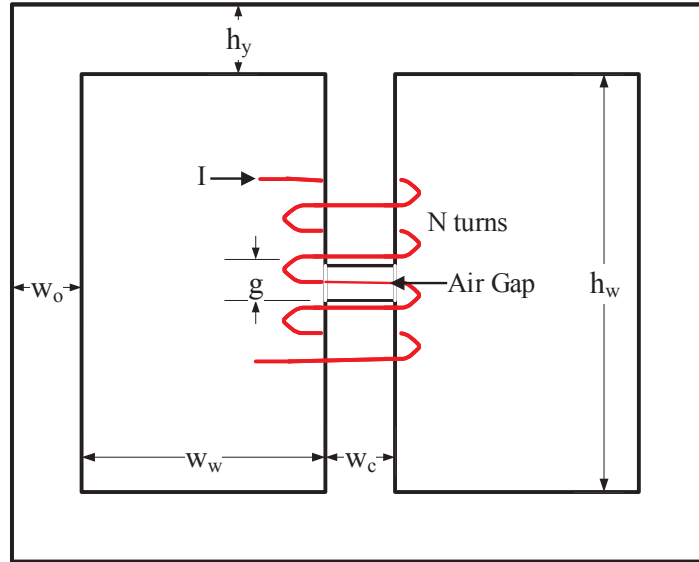
Figure 4.3: Front View of Reactor

Because of the presence of the air-gap in the core, the winding leakage flux becomes non-dominant for the magnetostatic characterization of the device. Therefore, an arbitrary choice of the winding configuration is made. The reactor features two windows of width w_w and height h_w. w_o and w_c are the widths of outer and central leg respectively. The central core has an air-gap of height g which extends d_c into the page, which is the same for the rest of the device as well. The height of the yoke of the reactor is denoted by h_y.

The proposed MEC of the reactor is shown in Fig. 4.4.

The reluctances and MMF in the MEC correspond to exact details of the reactor geometry. The winding around the central core represents the MMF source $F = NI$. Here, N is the number of turns and I is the current through the winding. In the figure, loop fluxes are represented by ϕ_1 and ϕ_2, making the inner leg branch flux to be $(\phi_1 - \phi_2)$ in the specified direction.
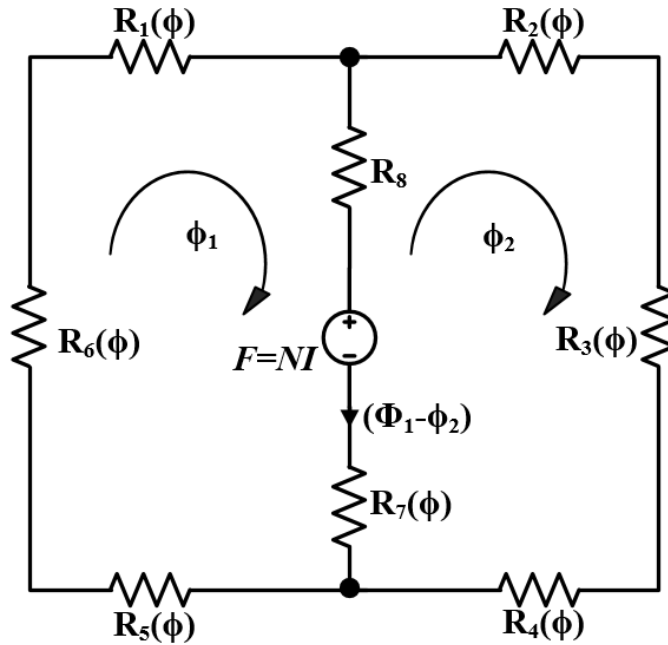
Figure 4.4: Magnetic Equivalent Circuit

Core-Piece Reluctances

The reluctances of the ferromagnetic core materials are represented by $R_1 - R_7$ which are a function of the magnetic flux through the respective elements. The core-piece reluctances are inherently non-linear, and are dependent on the core material, core geometry, and the current through the winding. Due to the symmetrical nature of the device, the representative reluctances of the core

material based on (3.11) are as given by:

$$R_1(\phi) = \frac{2w_w + w_o + w_c}{2d_c h_y \mu_B(\frac{\phi}{d_c h_y})} \tag{4.1a}$$

$$R_3(\phi) = \frac{h_y + h_w}{d_c w_o \mu_B(\frac{\phi}{d_c w_o})} \tag{4.1b}$$

$$R_7(\phi) = \frac{h_y + h_w - g}{d_c w_c \mu_B(\frac{\phi}{d_c w_c})} \tag{4.1c}$$

Here, $R_1(\phi) = R_2(\phi) = R_4(\phi) = R_5(\phi)$ and $R_3(\phi) = R_6(\phi)$.

Air-Gap Reluctance & Fringing Effect

The reluctance R_8 in the MEC model shown in Figure 7.5 corresponds to the reluctance of the air-gap. This reluctance is independent of the flux through it and constant. According to (3.4), the air-gap reluctance can be expressed as:

$$R_g = \frac{g}{d_w w_c \mu_0} \tag{4.2}$$

The reluctance in (4.2) assumes the streamlined flux flow across the core cross-section above and below the air-gap. But, there are portions of the flux that take paths in proximity of the corners of the gap spreading in all directions. This flux is called the fringing flux. The fringing flux causes the effective reluctance of the air-gap to reduce as the cross-section area effectively increases. In order to maintain the high accuracy of the MEC, the fringing flux should be incorporated into the air-gap flux.

Considering the uniform flux flow from node surfaces N_A to N_B along the length of the path as

49
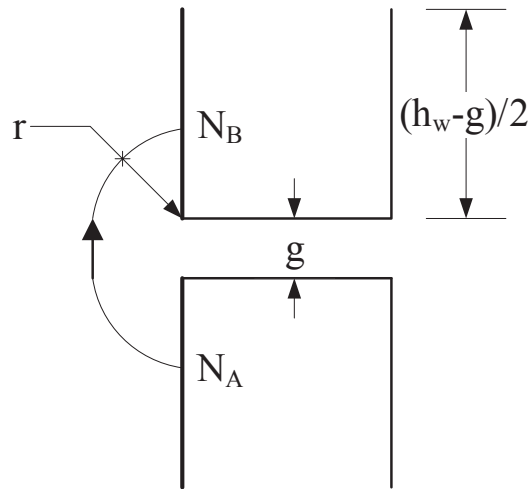
Figure 4.5: Fringing Permeance Calculation

shown in Figure 4.5, the Ampere's law gives:

$$H(g + \pi r) = F \tag{4.3}$$

where, H is magnetic flux intensity and F is the magnetomotive force source. The flux density can be expressed as:

$$B = \frac{\mu_0 F}{(g + \pi r)} \tag{4.4}$$

The flux leaving the surface of node A:

50

$$\phi = \int B dS = \int_0^{(h_w - g)/2} \frac{\mu_0 F}{(g + \pi r)} d_c dr \qquad (4.5)$$

The fringing flux associated with the indicated path is:

$$\phi = P_{fring} F \qquad (4.6)$$

Where, P_{fring} is the fringing permeance. Comparing equations (4.5) and (4.6):

$$P_{fring} = \frac{\mu_0 d_c}{\pi} log \left\{ 1 + \frac{\pi(h_w - g)}{2g} \right\} \qquad (4.7)$$

As the depth and the width are uniform throughout the reactor, the total permeance due to fringing is four times the P_{fring}. Therefore, the air-gap reluctance is:

$$R_{air-gap} = R_8 = R_g || \frac{1}{(4P_{fring})} = \frac{R_g}{1 + 4R_g P_{fring}} \qquad (4.8)$$

MEC Validation

The proposed MEC of the reactor is verified by comparing the equivalent inductances obtained from MEC using MATLAB, and the FEA based approach using ANSYS Maxwell.

Table 4.1: Gapped core reactor parameters

Parameters	Symbol	Value
Window height	h_w (m)	0.374
Window width	w_w (m)	0.056
Leg width	$w_o = w_c$ (m)	0.076
Yoke/base height	h_y (m)	0.076
Core depth	d_c (m)	0.076
Number of turns	N	39
Rated current	i (A)	$25\sqrt{2}$

A single-phase reactor is considered with parameters as shown in Table 4.1 for the MEC validation purpose.

A set of magnetic core materials (Si-Fe) is considered with accompanying qualities (relative permeability, permeability function parameters, and maximum flux densities) extracted from [47]. The magnetic properties (B-H curves) for these materials generated according to [44] are shown in Figure 4.6.

For both linear and non-linear regions of the magnetization characteristics of Si-Fe, it is clear that the anhysteretic curve of Hiperco50 is considerably different from the others, as can be seen in Figure 4.6.

Figure 4.7 shows 3-D FEA results for the reactor with the Si-Fe Hiperco50 core with the parameters from Table 4.1. The adaptive meshing has been applied to the model to make the simulation more accurate. The figure also shows the flux density distribution throughout the core, and it can be seen that the middle leg has the highest flux density.

For every core materials from the group, the inductances using both approaches and relative error between them are summarized in Table 4.2. The errors are within 1% for each of the materials. This minimal range of errors across a group of Si-Fe materials confirms the accuracy of the proposed
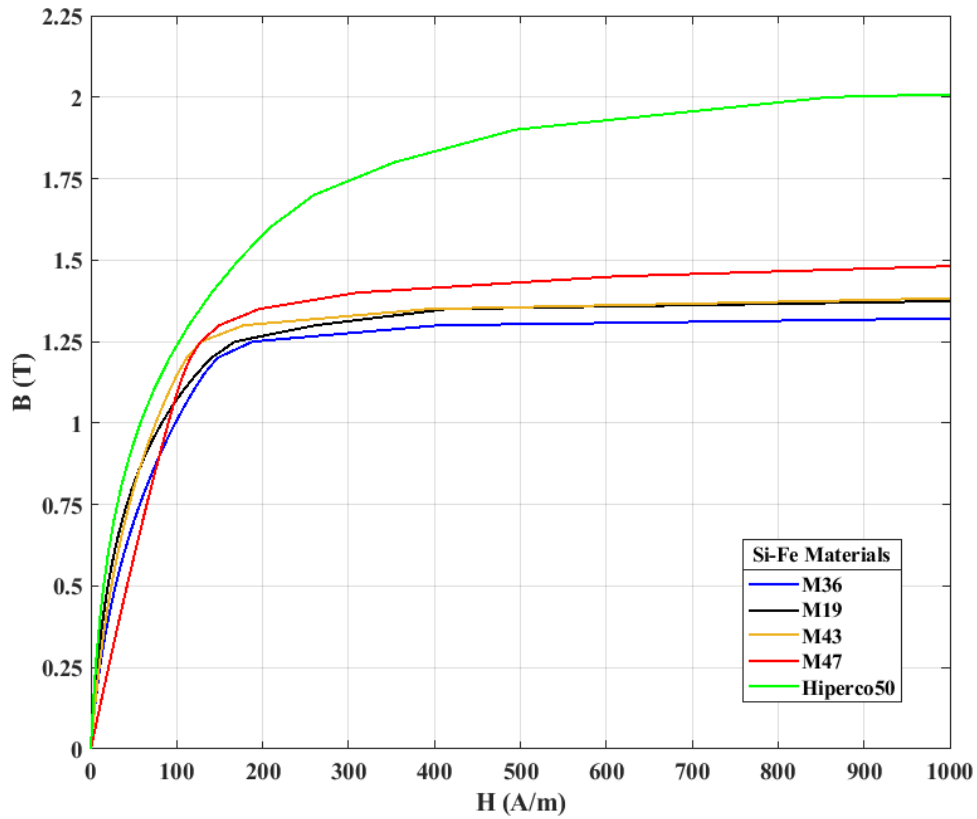
Figure 4.6: B-H Characteristics

MEC.

Reactance Calculation

A circuit reduction on MEC can be applied to obtain the equivalent reluctance of the reactor, as shown in Figure 4.8.

As the design of the reactor is symmetrical, a circuit simplification by the parallel combinations of the reluctances corresponding to the yoke and vertical leg transforms the MEC from Figure 4.4 to Figure 4.8a. Furthermore, the series reluctances in a single loop MEC in Figure 4.8a can be

(a) Adaptive mesh plot   (b) Flux density plot
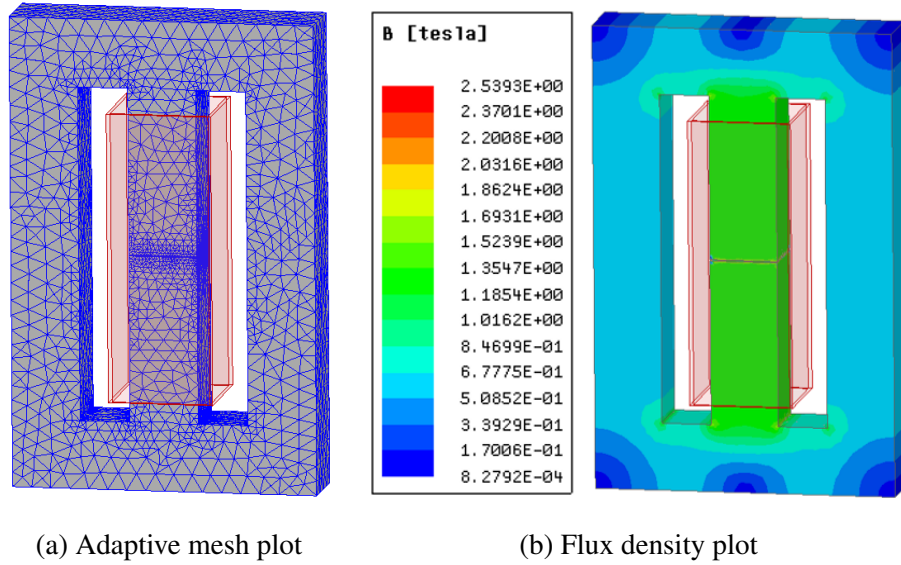
Figure 4.7: FEA simulation Results for Si-Fe Hiperco50 core

Table 4.2: Inductance comparison

Si-Fe Materials	Inductance (mH)		% Error
	MEC	FEA	
M19	7.853	7.880	0.348
M36	7.905	7.871	-0.427
M43	7.910	7.935	0.310
M47	7.831	7.904	0.925
Hiperco50	8.012	8.081	0.850

combined to achieve the simplest MEC as in Figure 4.8b. Accordingly:

$$\mathcal{R}_m = R_y(\phi) + 0.5R_l(\phi) + R_7(\phi) + R_8 \tag{4.9}$$

In Figure 4.8, $R_y \equiv \{R_1 = R_2 = R_4 = R_5\}$ and $R_l \equiv \{R_3 = R_6\}$. A further break down of (4.9) for a linear operation region (in the magnetization characteristic curve) returns:

54

(a) Step I

(b) Step II
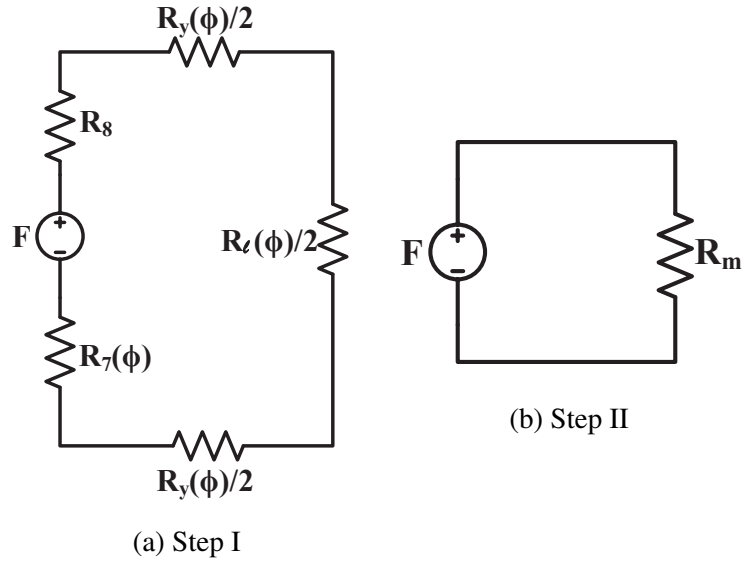
Figure 4.8: MEC reduction

$$\mathcal{R}_m = \frac{6.25 \times 10^5 g}{0.7854 d_c w_o + g d_c log\left(-0.5708 + \frac{1.5708 h_w}{g}\right)} + \frac{X\left\{-h_y g + w_o(w_o + w_w)\right\} + Y h_y(h_y + h_w)}{d_c h_y w_o}$$

(4.10)

A symbolic mathematical computation program called MATHEMATICA has been used to obtain this simplified expression. For different core materials, the coefficients X and Y in (4.10) are summarized in Table 4.3.

Table 4.3: Reactance coefficients

Si-Fe Materials	Coefficients	
	X	Y
M19	44.324	66.486
M36	58.996	88.494
M43	51.342	77.012
M47	86.369	129.554
Hiperco50	36.473	54.710

Design Optimization

Single Objective Optimization

An example of a single objective optimization problem is set up using the expression for the reactance of the reactor. The use of minimal material for the core is the objective while complying with several design constraints. Here, it is assumed that the reactor core is made up of Si-Fe M36 material. The design constraints include the target reactance, flux density limits for each element of MEC ($n = 8$), and minimum and maximum limits for the design parameters. The design parameter vector (4.12) consists of all design parameters. Their ranges and the initial points are summarized in Table 4.4. The complete single objective design optimization formulation is given by (4.11).

$$\min_{\mathbf{X}} \quad V = d_c\{2h_w w_o + w_c(h_w - g) + 2h_y(2w_w + 2w_o + w_c)$$

$$\text{s.t.} \quad X_L = x_{design},$$

$$B_k \leq B_{max}, \ \forall k \in n,$$

$$\mathbf{x}_{min} \leq \mathbf{X} \leq \mathbf{x}_{max}$$

(4.11)

In (4.11), $B_{max} = 1.25\,T$ is the maximum flux density in the linear region of the B-H curve for

Table 4.4: Domain of design parameters

Parameters	$\mathbf{x}_{min}$ (m)	$\mathbf{x}_{max}$ (m)	$\mathbf{x}_{initial}$ (m)
w_o	0.0762	0.1016	0.0889
w_w	0.0559	0.0762	0.0635
h_y	0.0762	0.1016	0.0889
h_w	0.3739	0.5080	0.4572
d_c	0.0762	0.1016	0.0889
g	0.0015	0.0023	0.0020
w_c	0.0762	0.1016	0.0889

Table 4.5: SO optimization results

Parameters	Value (m)	Parameters	Value (m)
w_w	0.0559	$w_o = w_c$	0.0762
h_y	0.0762	h_w	0.3739
g	2.286×10^{-3}	d_c	0.0762

Si-Fe M36, and $x_{design} = 2\,\Omega$.

$$\mathbf{x} = \begin{bmatrix} w_o & w_w & h_y & h_w & d_c & g & w_c \end{bmatrix}^T \tag{4.12}$$

There are multiplications of decision variables in the objective function, making the optimization a nonlinear program (NLP) problem. A nonlinear solver called 'Knitro' with YALMIP toolbox from MATLAB® has been used to solve this optimization problem. Table 4.5 summarizes the optimization results.

The optimal (minimum) ferromagnetic core material volume is found to be $1.0452 \times 10^{-2} m^3$. An approximate 'back-of-the-envelope' calculation for the volumetric minimization of the reactor with some educated guess regarding the constraints verifies the presented results. The air-gap (g) is very sensitive towards the reactance and the flux density in the core; however, it has a minimal
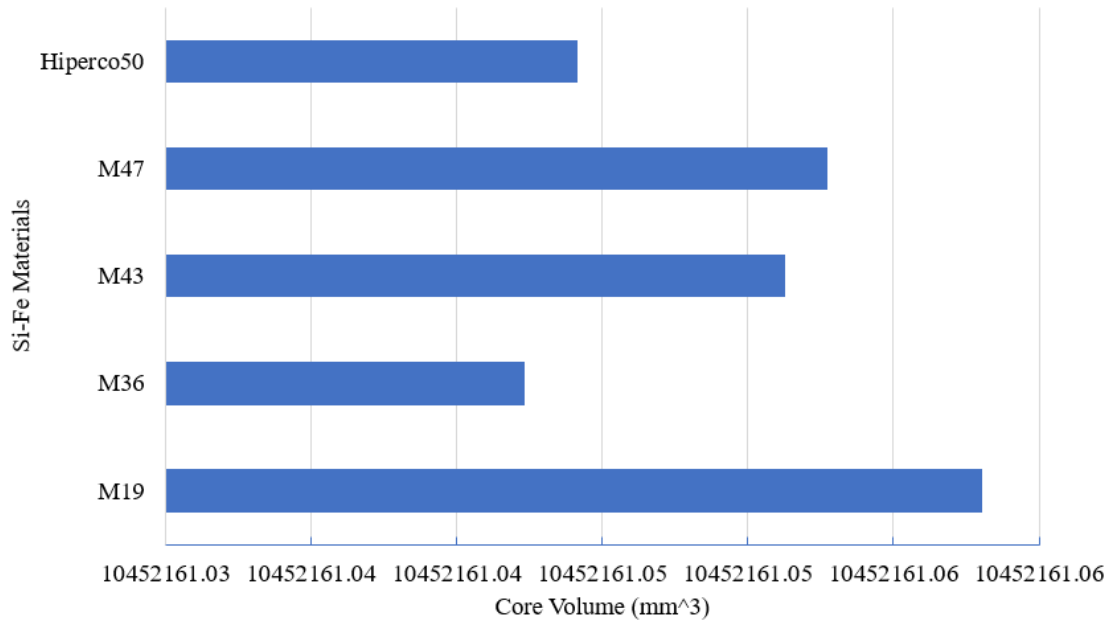
Figure 4.9: Optimal core volume comparison

impact on the reactor's total ferromagnetic volume. Therefore, the constraint set **x** other than g can be guessed towards the minimum limit to get the minimum ferromagnetic volume. If **x** is chosen to be x_{min}, the ferromagnetic volume would be $1.0457 \times 10^{-3} m^3$.

The optimal ferromagnetic volumes for different Si-Fe materials are summarized in Figure 4.9. In the figure, the ferromagnetic volumes are very near each other; however, the price difference between the materials will impact material selection.

Multi Objective Optimization

Reactance is the most important characteristic of the ferromagnetic core inductor. In addition to the core material volume minimization, an additional objective of reactance maximization is introduced here. The multi-objective (MO) optimization searches a vast design space and is quite

58

effective in finding optimal machine designs. An evolutionary population-based genetic algorithm [48] is implemented to solve a MO reactor optimization problem. A genetic algorithm (GA) can find multiple solutions from a population of solution candidates in one execution, which is not possible with classical optimization [49].

The goal of this design example is to come up with a single-phase power reactor design that has a reactance of at least X_{min}, and maximum ferromagnetic core flux density below B_{max}. It is desirable to minimize the reactor's ferromagnetic core material volume and maximize the reactance at the rated system conditions. The complete MO problem formulation is given by (4.13).

$$
\begin{aligned}
\min_{\mathbf{X}} \quad & \begin{bmatrix} V & \dfrac{1}{X_L} \end{bmatrix} \\
\text{s.t.} \quad & X_L \geq X_{Lmin}, \\
& B_m \leq B_{max}, \\
& \mathbf{x}_{min} \leq \mathbf{x} \leq \mathbf{x}_{max}
\end{aligned}
\tag{4.13}
$$

The ferromagnetic core material used in this optimization problem is the same material used for single objective optimization problem described in the previous section (Si-Fe M36). The optimal reactor would have a reactance of at least $1.5\,\Omega$ (X_{min}) and the flux density of the $1.25\,T$ (B_{max}) so that the operation of the reactor is within the linear region of the characteristics curve of the selected core material for the rated supply. In (4.13), the flux density has been bounded only for the middle leg flux density because it is the dominant flux density region. The gapped middle leg flux density can be approximated by:

$$
B_m = \frac{\phi_m}{A} = \frac{Ni}{\mathcal{R}_m A} \approx \frac{\mu_0 Ni}{g}
\tag{4.14}
$$

The parameter bounds are the same as in the previous section, given in Table 4.4. The free parameter vector is represented by (4.12). The symbols in parameter vector are as defined in Table 4.1. It is assumed that the window spaces are sufficient for the winding.

The fitness function for the MO optimization problem can be defined as:

$$f = \begin{cases} \varepsilon(\bar{c} - 1)[1 \ \ 1]^T, & \bar{c} < 1 \\ \left[\frac{1}{V} \ \ X_L\right]^T, & \bar{c} = 1 \end{cases} \tag{4.15}$$

In (4.15), ε–a small positive number (in order of 10^{-10})– does not have an influence on the optimization outcomes but is appropriate for the observation of the optimization progress.

And, $\bar{c}$ is the aggregate constraint of the MO problem, which is:

$$\bar{c} = \frac{1}{n_c} \sum_{i=1}^{n_c} c_i = \frac{c_1 + c_2}{2} \tag{4.16}$$

where, n_c is constraint number (here, $n_c = 2$). Once X_L and B_m have been evaluated using (3.26) and (4.14), constraint functions can be put together as (4.17):

$$c_1 = gte(X_L, X_{L_{min}}) \tag{4.17a}$$

$$c_2 = lte(B_m, B_{max}) \tag{4.17b}$$

where, $gte()$ and $lte()$ are greater-than-or-equal-to and less-than-or-equal-to functions, respec-

Table 4.6: Genetic algorithm parameters

Parameters	w_o	w_w	h_y	h_w	d_c	g	w_c
Encoding	log	log	log	log	log	log	log
Chromosome	1	1	1	1	1	1	1

Table 4.7: Summary of GA options implemented

GA	Elitist nondominated sorting GA(NSGA-II) [51]
Selection	Tournament selection
Death	Random replacement
Gene repair	Hard limiting
Scaling	Offset scaling

tively. These functions are defined as:

$$
\text{lte}(x, x_{max}) = \begin{cases} 1, & x \leq x_{max} \\[2ex] \frac{1}{1+x-x_{max}}, & x > x_{max} \end{cases}
\tag{4.18a}
$$

$$
\text{gte}(x, x_{min}) = \begin{cases} 1, & x \geq x_{min} \\[2ex] \frac{1}{1+x_{min}-x}, & x < x_{min} \end{cases}
\tag{4.18b}
$$

The MO optimization is carried out using GOSET [50], a MATLAB-based genetic optimization toolbox. The optimization has been performed with a population size of 1500 over 2000 generations with the specifications described by Table 4.6, and the parameter bounds given in Table 4.4.

Table 4.7 summarizes the GA options carried out in the different steps of the MO optimization.

Table 4.8: Sample design results

Parameters	Values (m)	Parameters	Values (m)
w_o	0.085	w_w	0.05589
h_y	0.076233	h_w	0.3739
d_c	0.0762	g	0.001524
w_c	0.0762		

Figure 4.10 represents the objective space at the end of the optimization, where each point represents the objectives of the corresponding design. The objective space plot is according to the fitness function definition. Therefore, reactance is plotted against the reciprocal of the ferromagnetic core material volume. The design points can be divided into nonviable, dominated, and nondominated design sets. The nonviable designs are near the origin and the negative axes of the objective space. The figure indicates the distinct design sets which are viable but dominated or nondominated.

Figure 4.11 shows only the nondominated designs with the axes representing the reactance and the material volume. This plot clearly shows the tradeoff between the objectives. A sample design on the Pareto optimal front is also indicated. The parameters representing the sample design are summarized in Table 4.8.

For the sample design, the ferromagnetic material volume is 0.011176 m^3, and the reactance of the inductor is 3.32 Ω. This reactance is above the minimum limit X_{Lmin}, and the flux density is found to be 1.137 T, which is less than the flux density limit B_{max}.

To check the validity of the sample design obtained above, a 3-D FEA model is created again with the parameters from Table 4.8. The magnetostatic analysis from FEA shows that the reactance of the sample design is 2.96 Ω, which is $\approx 12\%$ off from the MO optimization results. It is a fairly good result considering the simplicity of the model used, and more accurate than a spreadsheet-based design typically used by manufacturers.
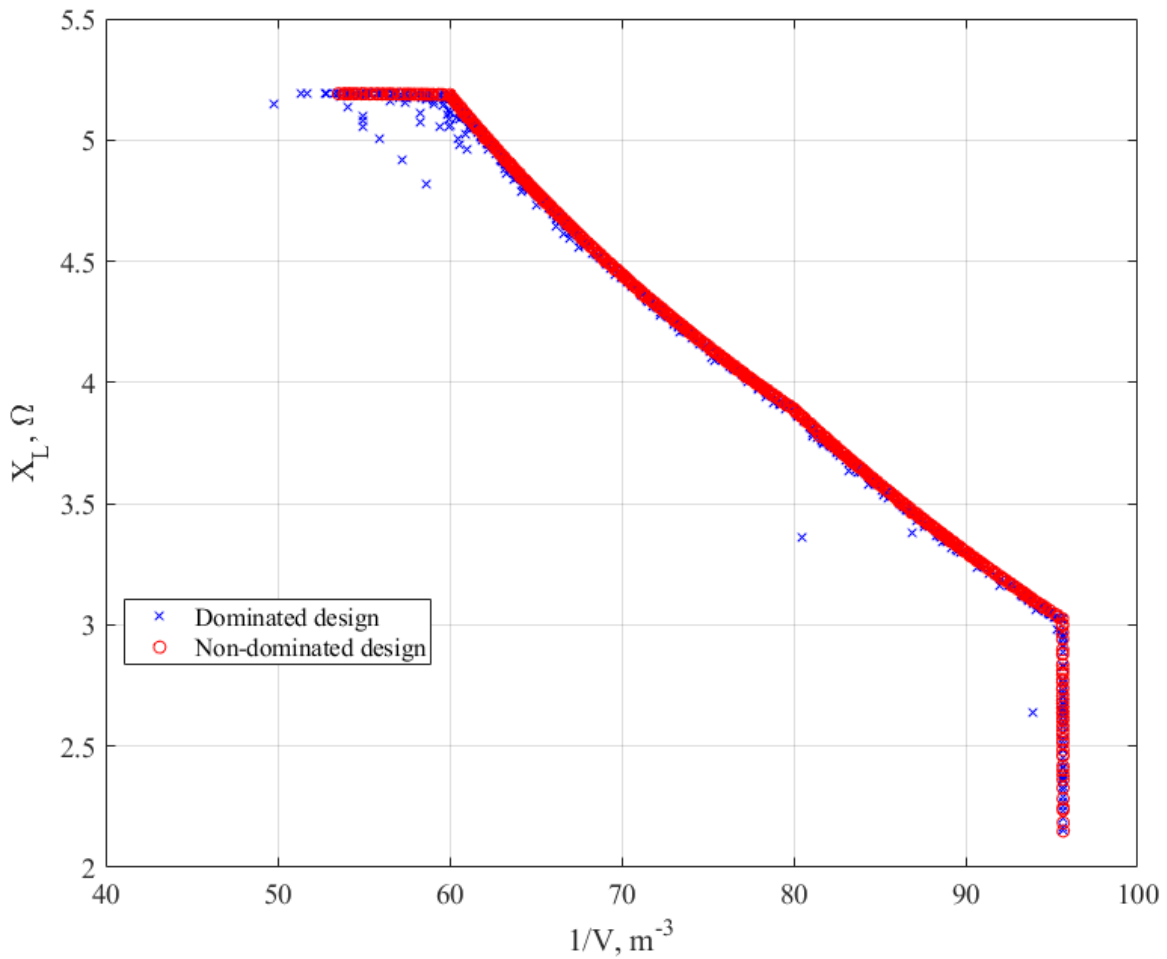
Figure 4.10: Objective design space

Conclusion

In this chapter, a systematic analytical representation was proposed for a $1 - \Phi$ ferromagnetic core air-gapped inductor based on MEC. For a set of Si-Fe materials for core, the proposed MEC was substantiated after collating the inductances obtained by using the 3-D FEA method. The minuscule error of the inductance values throughout the entire group of materials validated the proposed model. Furthermore, when the ferromagnetic core is in the unsaturated (linear) region of
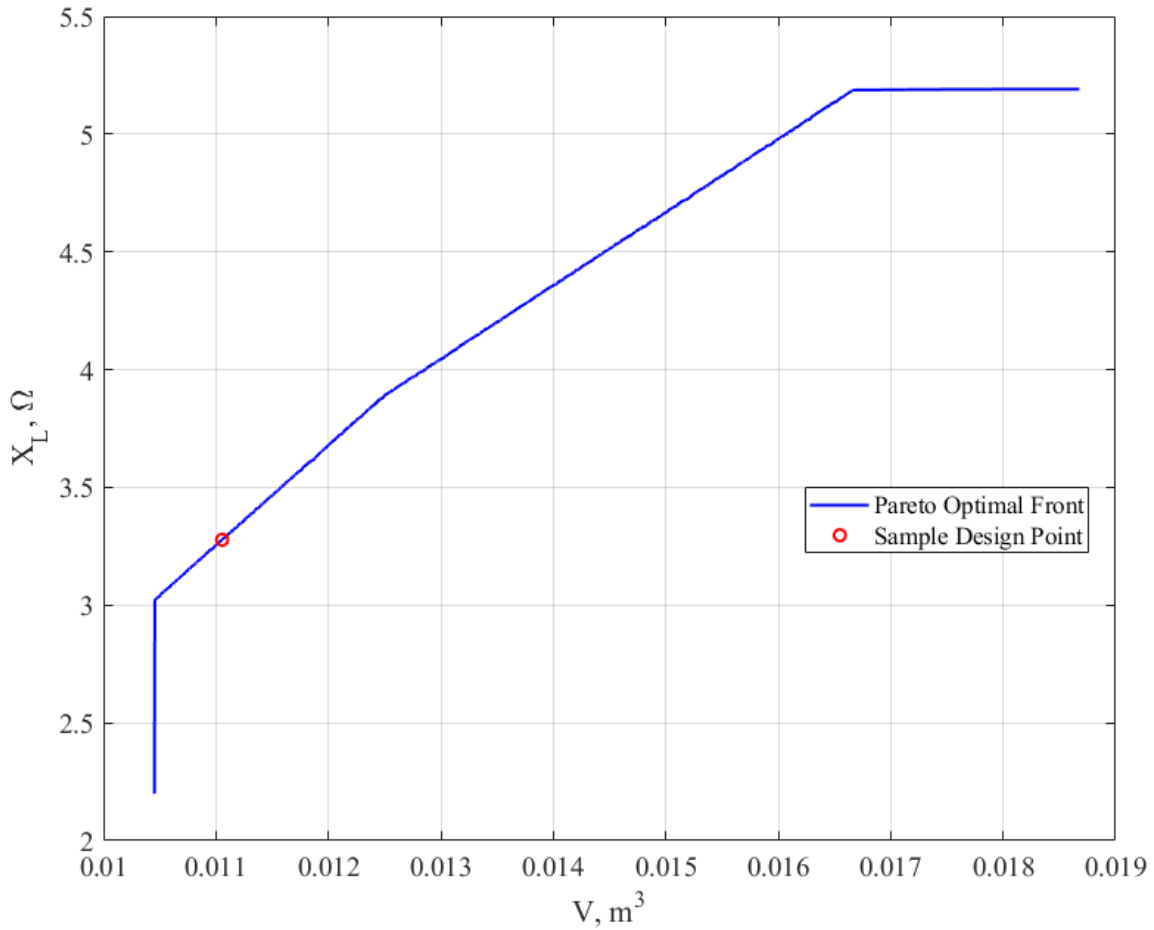
Figure 4.11: Pareto frontier boundary

the operation, an inductor reactance expression was derived as a function of design parameters. To illustrate one of the applications of the suggested systematic model, both SO and MO optimization problems were formulated and solved. They prove the MEC's applicability for obtaining optimal reactor designs for a specific application and highlight its efficiency and importance.

CHAPTER 5: MAGNETIC AMPLIFIER CHARACTERIZATION USING ARTIFICIAL NEURAL NETWORK (ANN)

Introduction

For all applications of magnetic amplifiers (MA), as indicated in Chapter 2, the supply to windings, along with the material type and core dimensions, determines the impedance of MA. As material types and sizes are constants for a MA, understanding the impacts of currents through the windings on the working of MA helps provide the case for the widespread adoption of this technology. Some numerical and analytical methods can be used to understand MA characteristics. This chapter discusses some of those methods and proposes a superior technique based on the artificial neural network (ANN), which uses the MA impedance results obtained through limited three-dimensional finite element analysis (3-D FEA) based simulations as training data. Based on a case study carried out with a sample MA, the characterization performance matrices for two distinct frameworks based on ANN are obtained and analyzed to determine the effectiveness of the proposed methods. The main contributions of this chapter are:

1. Review magnetic analysis methods applicable for MA characterization

2. Present novel ANN-based approach for MA reactance variation modeling

3. Provide unique physics informed ANN-based (PIANN) framework for MEC based analytical model accuracy improvement for MA

The chapter is organized as follows. The second section summarizes few techniques for the MA characterization. The application framework for the ANN for MA behavior mapping is provided

in the following Section, which is followed by a numerical study in Section that evaluates its effectiveness. And the last section concludes the chapter.

Magnetic Amplifier Characterization

Understanding the working of a multi-winding device like MA is essential for the exploration of its applications. The characteristics of MA are often described in terms of its inductance, and its computation is considered essential for electromagnetic field analysis. Inductance defines the relationship between flux linkages and currents, and differential inductance governs an inductor's circuit behavior [52]. For a device like MA, where there are multiple excitations, and most magnetic energy is stored in the surrounding space rather than the magnetic core, the B-H characteristics can be reduced by ignoring the hysteresis effect. The anhysteretic characteristic of magnetic material is one of its most fundamental properties and vital for magnetic analyses. The conventional methods for material characterizations like Epstine frame, single sheet tester (SST), extrapolated measurements, and toroidal samples have their drawbacks and inaccuracies. The complexities in characterization arise due to the core's saturation and its temperature dependence [53], [54]. The nonlinear material modeling are often carried out using inverse tangent functions [20], exponential functions[21], and piecewise linear functions[22], [55]. One of the efficient and accurate approaches to representing the nonlinear magnetic characteristics is to define the material permeability as a function of either magnetic flux density or magnetic field intensity with experimentally found permeability function parameters [54].

The prevalent methods applicable for the detailed analysis of MA can be categorized into the following.

Numerical Method

The description of this approach is provided in Chapter 2.

Analytical Methods

Two-Core Approach

It is a MA model approach using two magnetically decoupled cores [21], [22], [56]. It presents the most straightforward way of closed-form representation for MA. The MA, as shown in Figure 2.4, can be represented as an aggregation of two separate cores, as in Figure 5.1. Here the MA is cut symmetrically by a verticle plane into two identical cores both in geometry and material composition. The electrical representation of the two core approach is shown in Figure 5.2, which shows the magnetically decoupled cores' electrical coupling. The windings, both AC and DC, retain their configuration from the original MA.
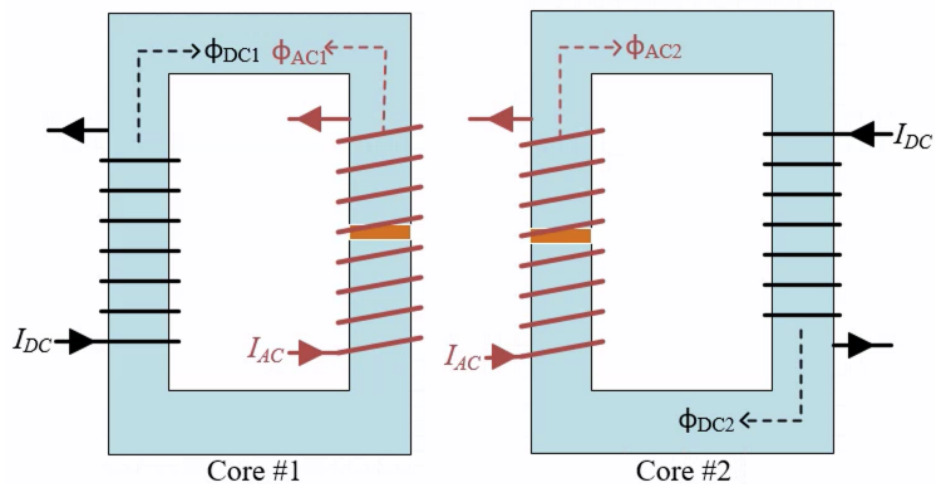
Figure 5.1: MA split into two decoupled cores
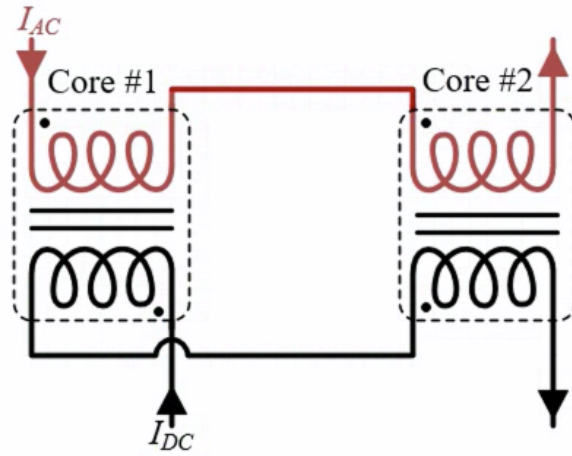
Figure 5.2: Electric circuit representation of two core model

In each core, there is a uniform flux combination of AC and DC flux components. During each AC half cycle, the AC and DC fluxes counter in one core (bulk core) and sum in the other core (boost core). Generally, the buck and boost mode results in MA's operation in linear and saturation regions of magnetic characteristics, respectively. However, depending on the application, it might differ. The operation region dictates the reactance of the MA: higher reactance in linear and lower reactance in the saturation region. The reactance offered by MA is directly proportional to the absolute permeability of the core.

The flux linkage in AC windings in both cores as the function of AC and DC can be summarized by (5.1).

$$\lambda(I_{ac}, I_{DC}) = \frac{n_{ac}A}{l}(n_{ac}I_{ac} \pm N_{DC}I_{DC})\mu_H(H) \tag{5.1}$$

In (5.1), I_{ac} = instantaneous AC, n_{ac} = number of AC turns, A= cross-sectional area of the core, l = mean magnetic flux path length, $\mu_H(H)$ = magnetic permeability as a function of flux intensity (H). Also, a simplifying assumption has been made to disregard the air-gap in the core. Here choosing one of the signs gives the flux linkage for the bulk or boost core.

68

It leads to the differential inductance of both cores as the function of AC and DC represented by (5.2).

$$L_d(I_{ac}, I_{DC}) = \frac{\partial \lambda(I_{ac}, I_{DC})}{\partial I_{ac}}$$

$$= \frac{n_{ac}^2 A}{l} \left\{ \mu_H(H) + \left(I_{ac} \pm \frac{N_{DC}}{n_{ac}} I_{DC} \right) \frac{\partial \mu_H(H)}{\partial I_{ac}} \right\} \tag{5.2}$$

In (5.2), a choice of the sign produces the differential inductance of either core 1 (negative sign) or core 2 (positive sign).

The anhysteretic representation of the parameterized permeability as a function of flux intensity can be given by (5.3) [54].

$$\mu_H(H) = \mu_0 + sgn(H) \sum_{k=1}^{K} \frac{m_k}{h_k} \frac{1}{|H/h_k|^{n_k}} \tag{5.3}$$

In (5.3), $sgn()$ is the sign function, m_k, h_k, and n_k are constants and K is the number of terms used. These parameters are found experimentally for different types of magnetic materials.

Once the inductance of individual cores is known, the inductance of MA is found by the superposition as the two AC windings are connected in series.

This approach is valid only for the linear operation of the MA without gaps in its core, which means superposition is not always useful. For a practical MA, which exploits the saturation and the gaps in a core, this method can not provide accurate results without extensive assumptions. However, it can help with the fundamental understanding of the physics behind its operation, which could serve as the starting point for the exact modeling [56].

MEC Based Model

The description of this approach is provided in Chapter 2.

Two of the many possible MECs of single-phase MA is shown in Figure 5.3, Figure 5.3a being the simplest. In Figure 5.3a, MA is represented by the combination of MMFs and reluctances of core-pieces and air-gap. Unless the leakage flux is taken care of by using some factors while calculating core reluctances, it can not fully and accurately represent the MA. While in Fig. 5.3b, the leakage flux paths are represented by the separate reluctance across each leg. The leakage reluctance inclusion makes the MEC complex, but it gives a better representation of MA. In Figure 5.3, the core-piece reluctances are indicated as a function of respective fluxes, while leakages reluctances are considered constant irrespective of the fluxes through them. The leakage reluctances in Figure 5.3b are:

- Air-gap reluctance with fringing effect ($R_g = R_8$)

- Combination of external adjacent leakage, horizontal and vertical components of slot leakage reluctances ($R_9 - R_{11}$)

The reluctance of a ferromagnetic core piece is given by (3.11), and elaboration of the components of leakage reluctance is out of the scope of the work.

The nonlinear reluctances from the MEC are found using an iterative solution approach described in [44], summarized in [9]. The main issues of modeling MA using MEC based approach are: a) the accurate leakage reluctance modeling is complex, and b) the assumption that leakage reluctances are constant for all excitation combinations is not valid for MA (with continuously changing AC and DC supplies). Based on the excitations, the flux flow changes drastically, and the leakage reluctance needs to be dynamically modeled.
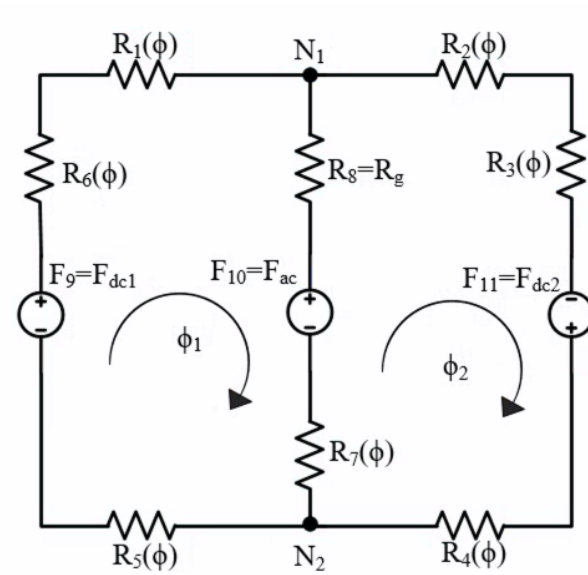
(a) Simplest MEC
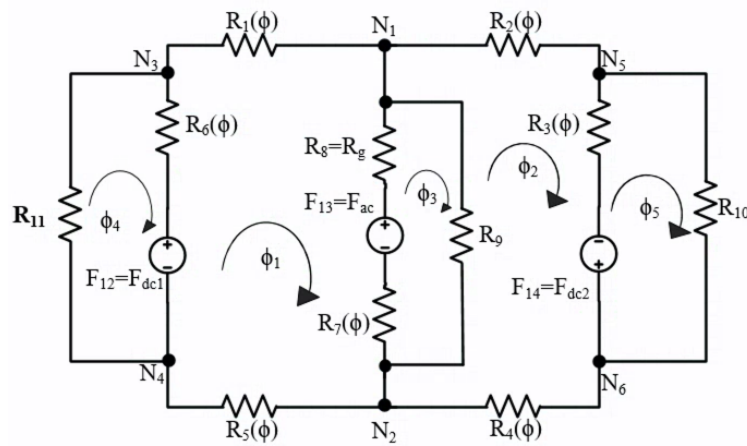
(b) Elaborated MEC

Figure 5.3: MECs for magnetic amplifier

Artificial Neural Network (ANN) Application

Recently, there has been a very high interest in applying machine learning (ML) approaches in power systems from researchers around the globe. Those power system areas include but not

limited to operation support [57], system security assessment [58]–[60], optimal power flow (OPF) [61], and many more. The application of ML for machine design can ease the laborious work of design engineers by assisting in sophisticated designs. It paves the way for generative design approaches, which has the potential to revolutionize the design engineering [62]. [63] discusses the application of AI for electrical machines monitoring and fault detection. Most of these works ignore the underlying physics resulting in the models heavily dependent on the quality and quantity of training data and complex model structure. This dependency on the training data and complex model structure can be reduced by exploiting the physics behind the model while achieving the high accuracy [64]. The neural network is able to represent complex models that form non-linear hypotheses.

The issues with previously explained methods for MA characterization can be solved or minimized by using data driven ML-based approaches. In this article, two frameworks for the MA characterization based on ANN are presented.

Some assumptions that are made for the application of the ANN are summarized below.

1. The reactances obtained from FEA are considered accurate baring it's own limitation based on the set up.

2. The maximum AC supply for its variation should be chosen in such a way that MA wouldn't go into saturation without any DC supplies.

Reactance prediction using ANN

In this framework, ANN is used as standalone for the reactance prediction of the MA for a wide range of supply variations (both AC and DC). The steps involved in this framework are summarized in Figure 5.4.

72
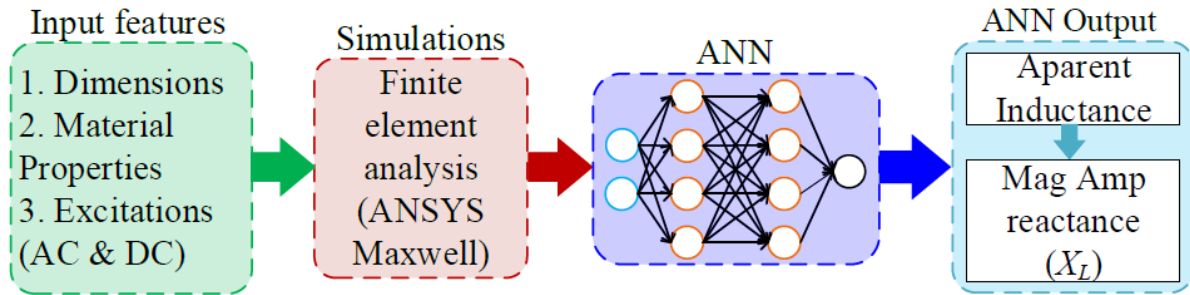
Figure 5.4: Application of ANN for reactance prediction

First, a comprehensive FEA-based model (3D-FEA) is created for a MA based on its dimensions (core, windings) and material properties (core, windings, region around MA). The AC and DC excitation variations in user defined steps are also introduced in the FEA model. The simulation of the FEA model can provide an accurate reactances for a pair of AC and DC values. These results of reactances for same physical parameters of MA can be used to train an ANN which predicts the reactance value for a select choice of excitation combinations within the whole range. This method avoids the need to run FEA models every time the reactances are needed. As the computation need for a single excitation combination simulations and a simulation with multiple excitation variations are not linear, this framework can provide huge computational advantage. Depending on the structure of the ANN, the MA reactances can be predicted with high accuracy. However, this framework works as a black-box with a pair of excitations as input and reactance of MA as output without any insights into the factors affecting the reactance variations. This drawbacks can be avoided with the following framework.
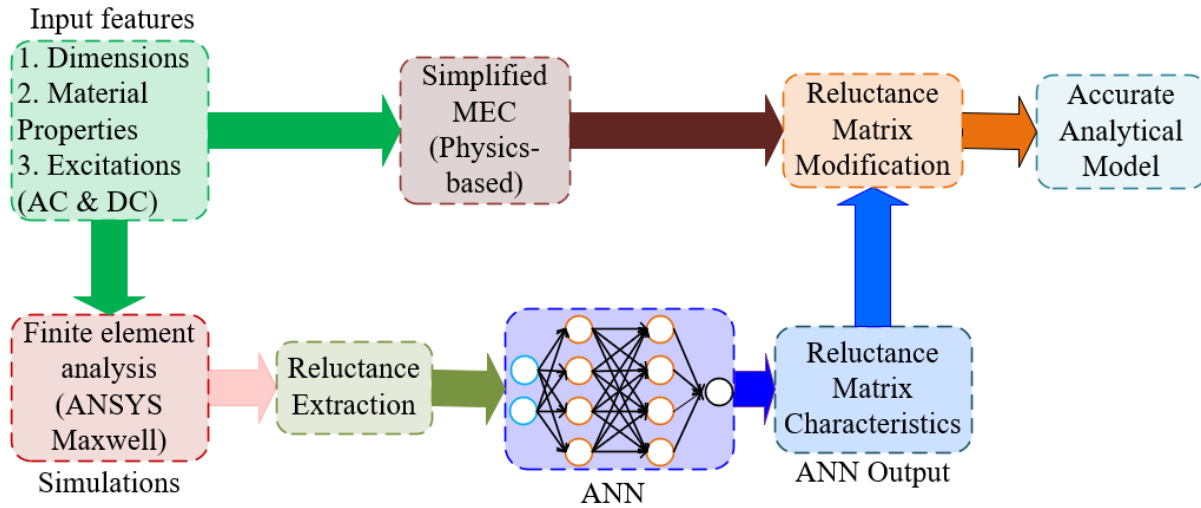
Figure 5.5: Physics-informed ANN (PIANN) for MEC accuracy improvement

Physics-informed ANN (PIANN) for MEC accuracy improvement

This framework combines the ANN results with a simplified MEC to improve its accuracy. It brings the accuracy of the FEA and closed-form solutions of MEC together for better characterization of the MA. Figure 5.5 shows various steps of this framework.

It uses two processes in parallel. Based on the physical dimensions and material properties, an FEA and a simplest MEC (as shown in Figure 5.3a) are created. As in the previous framework, the FEA is set up for a wide range of excitation variation. However additional set up are carried out so that the flux and flux intensities can be calculated around the MA structure and based on these values branch reluctance corresponding to the MEC model can be computed from FEA model. The branch reluctance matrices for variety of excitation variation for constant physical attributes of MA are used to train the ANN. The reluctance matrices predicted by ANN are compared against the reluctance from the simple MEC. As the simple MEC considers only the flux flow through the ferromagnetic core, i.e., it does not represent the leakages, and there are multiple supplies to MA,

74

the reluctances obtained from the MEC are pretty inaccurate. On the other hand, reluctances matrices from FEA are more accurate depending on the size and positions of planes for flux calculation. Based on the reluctance matrix comparison, improvement can be made to the simplified MEC with some multiplication factors. This way, this framework estimates the dynamic leakage reluctance for MEC accuracy improvement.

The approximate equivalent reactance of MA from simple MEC:

$$X_{eq} = \frac{\omega n_{ac}^2}{\mathcal{R}_{eq}} = \frac{\omega n_{ac}^2}{R_2 + 0.5R_3 + R_7 + R_8} \tag{5.4}$$

In (5.4), $\mathcal{R}_{eq}$ is the equivalent reluctance from the MEC, obtained by circuit simplifications, which is placed in series with the ac excitation. The symmetrical nature of the MEC resulted in a simplified expression of (5.4). Also, since the dc excitation causes the reluctances to change, they are removed while calculating equivalent reluctance. ω is the angular system frequency.

Now, a multiplication factor is calculated using:

$$k_i = \frac{R_{i,ANN}}{R_{i,MEC}} \tag{5.5}$$

When these factors (k_i) are used with the reactance expression of (5.4), the modified reactance of the MA is:

$$X'_{eq} = \frac{\omega n_{ac}^2}{k_2 R_2 + 0.5k_3 R_3 + k_7 R_7 + k_8 R_8} \tag{5.6}$$

Here, X'_{eq} will be more accurate than X_{eq}. In this framework, the accuracy of the reactance calculation is improved using ANN. This time it does not work as a black box, and a lot of information

Table 5.1: Single-phase magnetic amplifier parameters

Parameters	Symbol	Value
Height of window	h_w(in)	14.72
Width of window	w_w(in)	2.2
Width of central leg	w_{cl}(in)	2.75
Width of outer leg	w_{cl}(in)	3
Height of yoke and base	h_y(in)	3
Depth of core	d_c(in)	3
Height of gap	g(in)	0.03
Number of DC turns	N_{dc}	39
Number of AC turns	N_{ac}	40
Angular system frequency	ω(rad/sec)	120π

can be derived from the closed-form reactance expression, (5.6). Now the information regarding the MA physics is combined with the ANN; thus, the framework's name is physics-informed ANN.

Numerical Studies

A case study has been set up to examine the effectiveness of the frameworks presented. A single phase MA with the parameters shown in Table 6.4 is used. The ferromagnetic material used is Silicon Steel (Si-Fe) M36, whose anhysteretic B-H characteristics (shown in Figure 5.6) are extracted from [47] with some accompanying quantities (relative permeability, permeability function parameters, and maximum flux densities). The effective reactance of the MA will be computed and compared using multiple methods: simplified MEC, FEA, ANN and PIANN. The two-core method will not be explored here as its effectiveness and accuracy are already known and inferior to other approaches.
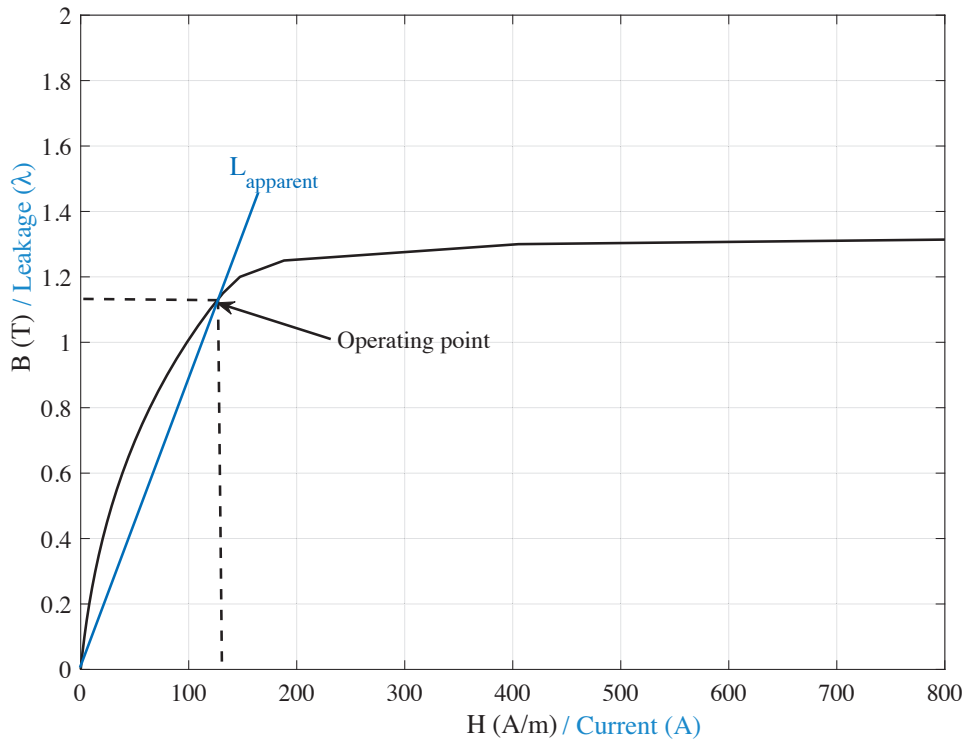
Figure 5.6: Si-Fe M36 B-H characteristics and apparent inductance definition

Simplified MEC

The effective reactance of the MA-based on a simplified MEC (Figure 5.3a) is given by (5.4). In (5.4), the equivalent reluctance of the circuit is found by the circuit reduction. As the supply to AC and DC windings are changed, the reluctance of the flux paths–ferromagnetic core pieces–get altered, and so do the effective reluctance of the circuit. For supply variation of AC and DC, the equivalent reactance of the MA using (5.4) is as shown in Figure 5.7.

From Figure 5.7, it can be seen that the effective reactance of the MA changes from 5.1Ω to 0.03Ω with the variation of supplies. Because the leakages are not considered in this computation, the reactance values change very swiftly, and the impact of wide supply variation can not be seen in

77
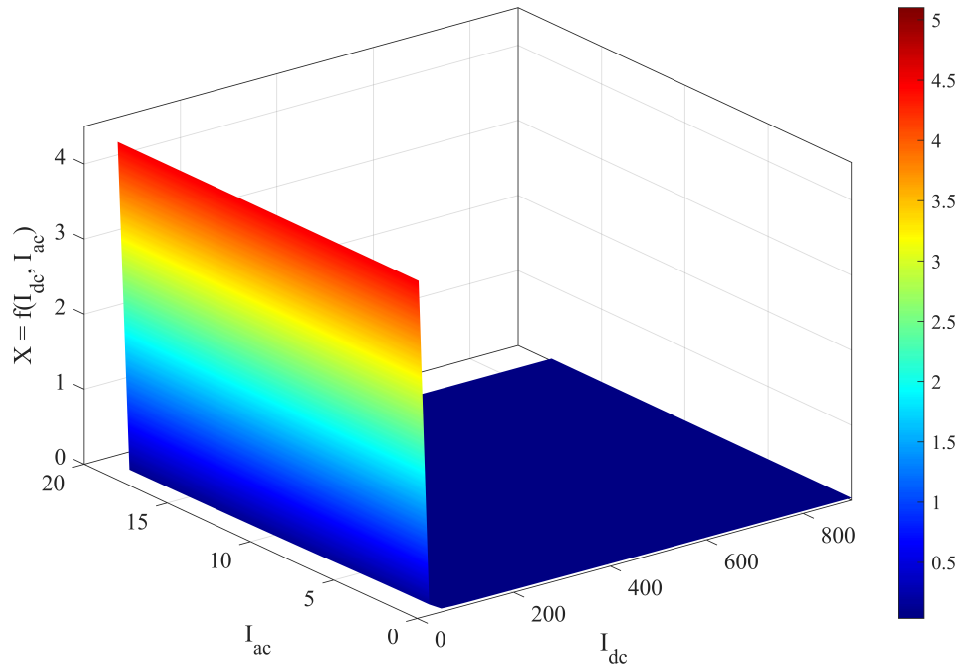
Figure 5.7: Reactance variation plot using simple MEC

this method. The reactances obtained from the simplified MEC is inaccurate because it does not consider all the flux flow paths.

FEA

The FEA simulations are used as a benchmark for the evaluation of all other methods. The FEA is performed using ANSYS Maxwell. The sample adaptive messing and flux density plot for an instant (AC supply of $3A$ (peak) and DC bias of $10A$ at $t = 44.44ms$) are shown in Figure 5.8 for the considered MA. At the given instant, the maximum flux density in the core is $1.27T$ around the outer ferromagnetic flux path.

The reactance variation to both of the supply variations is summarized in Figure 5.9. Here, the

(a) Adaptive meshing

(b) Flux density plot
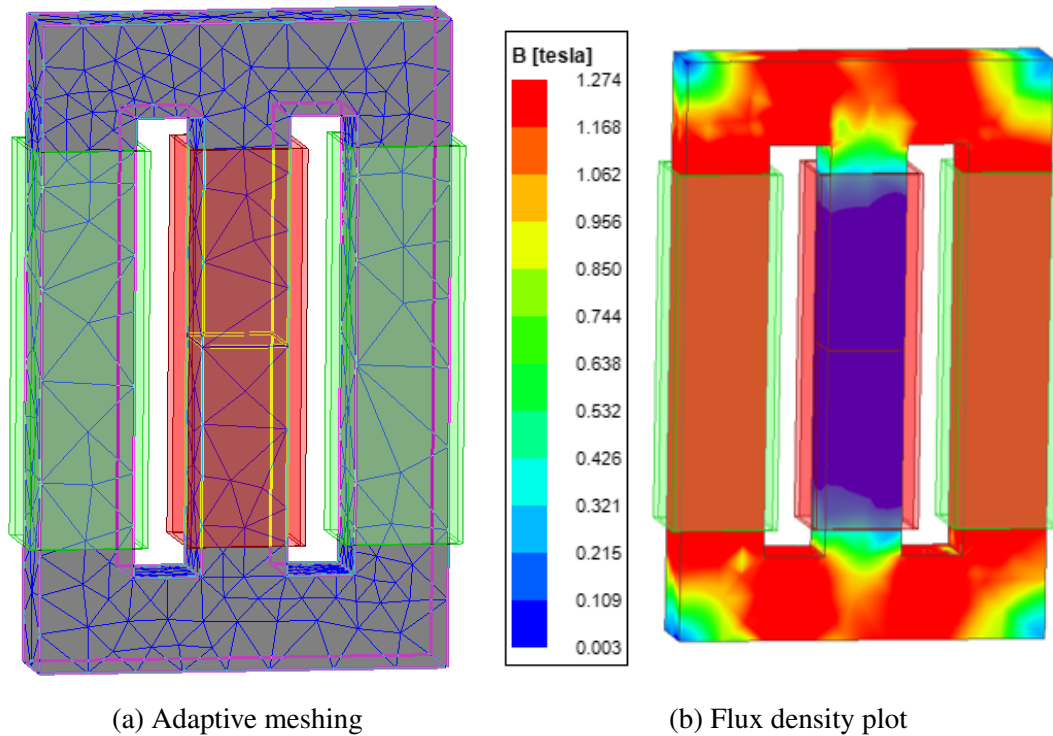
Figure 5.8: FEA simulation for $I_{ACp} = 3A$, and $I_{DC} = 10A$ at $t = 44.44ms$

self-inductive reactance is computed with apparent settings. As shown in Figure 5.6, the ratio of the flux linkage to the current gives the apparent inductance at that operating point. The simulation is run through multiple cycles of sinusoidal AC supply variation for a combination of peak AC and DC excitations. Moreover, reactance is expressed as the average over the entire simulation period for each excitation combination.

In Figure 5.9, the reactance varies from 6.03Ω to 0.4Ω with excitation combinations. The impact of both AC and DC variation can be observed in this approach.
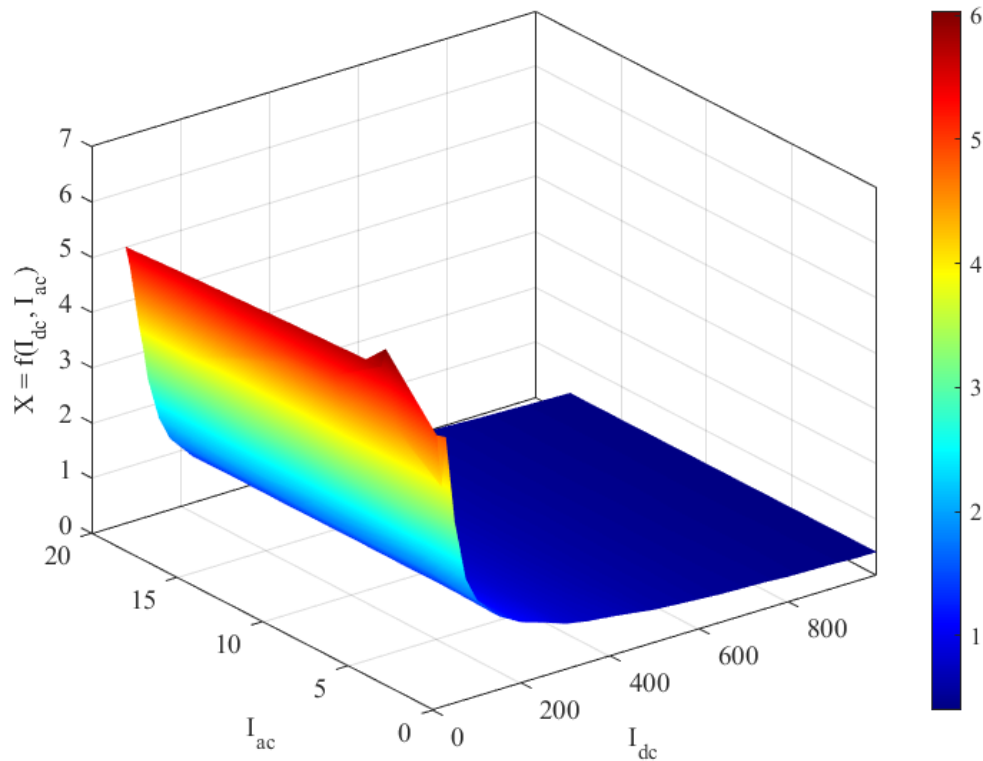
Figure 5.9: Reactance variation plot using FEA

ANN

The reactances of the MA computed using the FEA method described in the previous section for a variation on both AC and DC supplies are used to train ANN. The ANN has two inputs: AC and DC and one output: reactance, with one hidden layer of 10 elements. The ANN is performed using the neural network toolbox from MATLAB using Levenberg-Marquardt backpropagation algorithm. The ANN uses random data division with 70% being the training, 15% being the validation and the remaining 15% being the testing data. The performance of the ANN is summarized in Table 5.2.

Each of the performance measures is less than 2% for training, validation, and testing. Here MSE

Table 5.2: ANN performance matrices

	MSE	MAE	SAE
Training	6.899×10^{-3}	1.6377×10^{-2}	1.637×10^{-2}
Validation	5.197×10^{-3}	1.3847×10^{-2}	1.345×10^{-2}
Testing	1.024×10^{-2}	1.24×10^{-2}	1.29434×10^{-2}

(mean square error), MAE (mean absolute error), and SAE (sum absolute error) are used as ANN performance indices.

PIANN

In this case, the ANN is used to predict the branch reluctances corresponding to the branches of simplified MEC of Figure 5.3a. The data preparation for this framework is not straightforward. The reluctance of a branch, i corresponding to a branch in MEC is calculated as the ratio of magnetomotive force (F_i) and flux through the plane (ϕ_i), as described by (5.7). In order to make these calculations, seven non-model planes are created in the FEA model as shown in Figure 5.10.

$$R_i = \frac{F_i}{\phi_i} \tag{5.7}$$

In Figure 5.10, $\alpha_1 = (w_o + w_s)$, $\alpha_2 = (w_c + w_s)$, and $\beta_1 = \beta_2 = 3d_s$.

The application of the Ampere's law determines the effective flux intensities across each branches, which aid in calculating the respective magnetomotive force ($F = Ni = Hdl$). In FEA, a line integral of the flux intensities between two points corresponding to the nodes from the MEC is used to calculate the flux intensity across the select planes. Considering the symmetry of the MA, some representative flux intensities are shown in Figure 5.11.

81

(a) Top view   (b) Front view
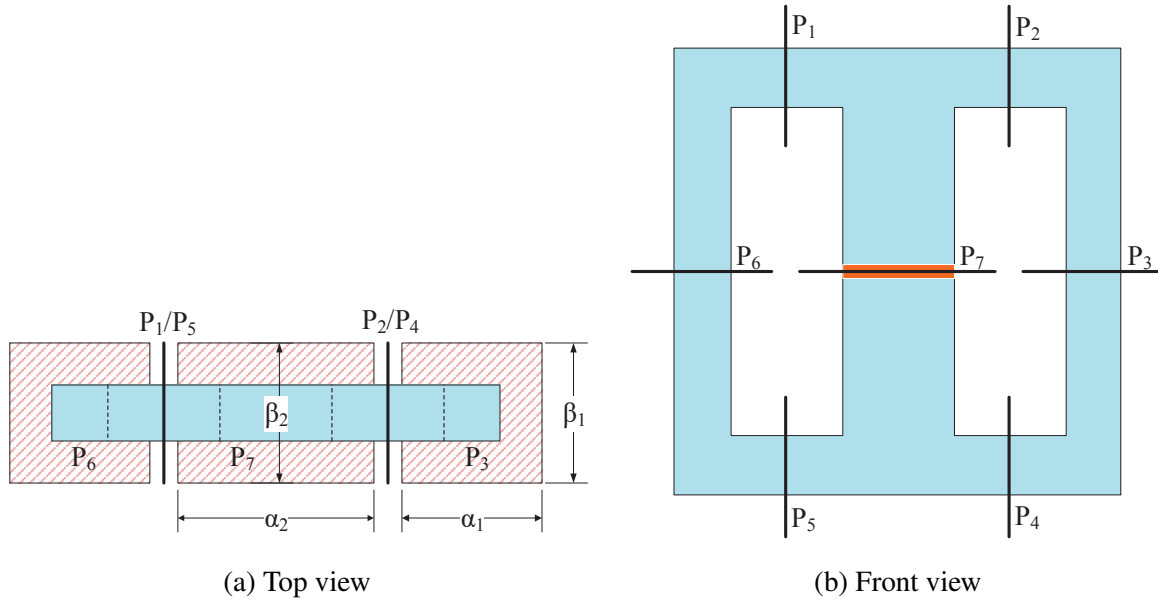
Figure 5.10: FEA model flux measurement planes: horizontal planes (P_3, P_6, P_7) & vertical planes (P_1, P_2, P_4, P_5)

The fluxes across each plane (j) are calculated using the surface integral of the flux densities across the select planes as described by (5.8). The sample fluxes through the planes are summarized in Figure 5.12. In (5.8), S_j is the cross sectional area of the respective plane.

$$\phi_j = \int B_j dS_j \tag{5.8}$$

The reluctance characteristics of the representative branches according to (5.7) are shown in Figure 5.13

Now, an ANN is constructed to predict the branch reluctances of the simplified MEC. The same toolbox and algorithm from the previous approach are applied. The performance matrices of this ANN are summarized in Table 5.3. The accuracy of the predicted reluctance matrix is character-
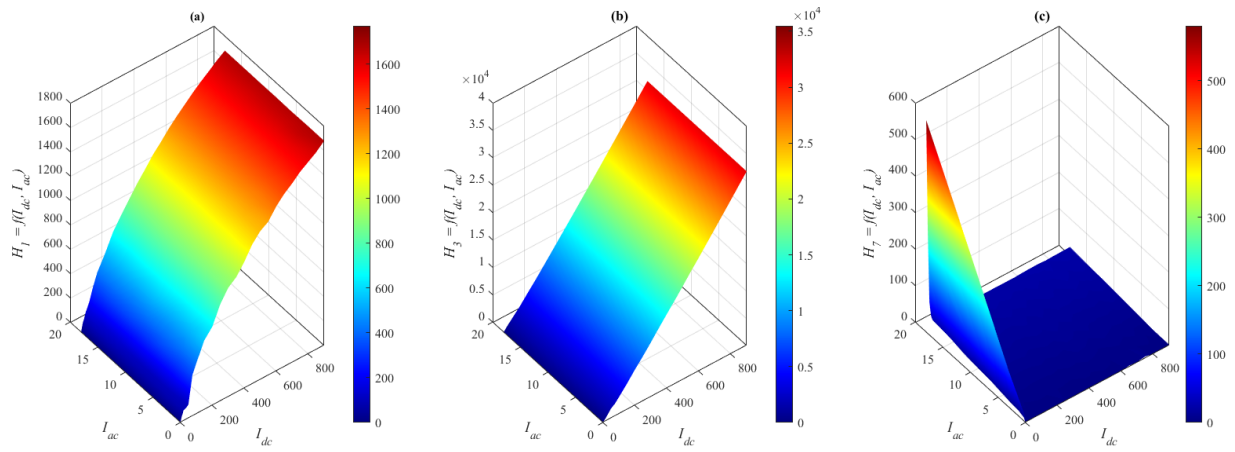
Figure 5.11: Magnetic field intensities across: (a) Branch 1, (b) Branch 3, and (c) Branch 7
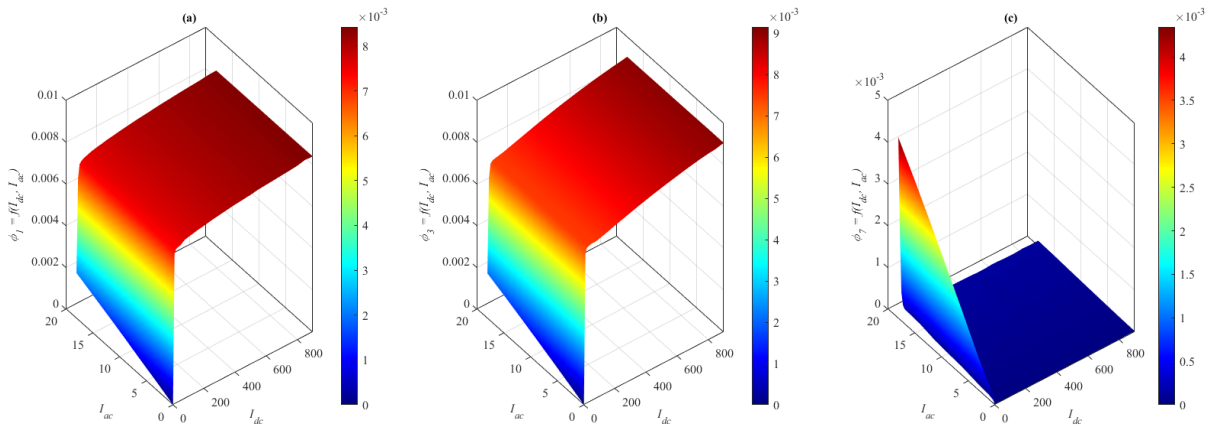
Figure 5.12: Magnetic flux through: (a) Plane 1, (b) Plane 3, and (c) Plane 7

ized by the ANN performance indices from the table, which shows minimal errors for training, validation, and testing. This ANN has two inputs, seven outputs, and five hidden layers, with each having ten elements.

Based on the predicted reluctance matrix, the dynamic multiplication factor, (5.5), can be generated for the wide range of excitation variations. Furthermore, using those multiplication factors for each branch, the improved reactance of the MA can be found using (5.6). This improved closed-form
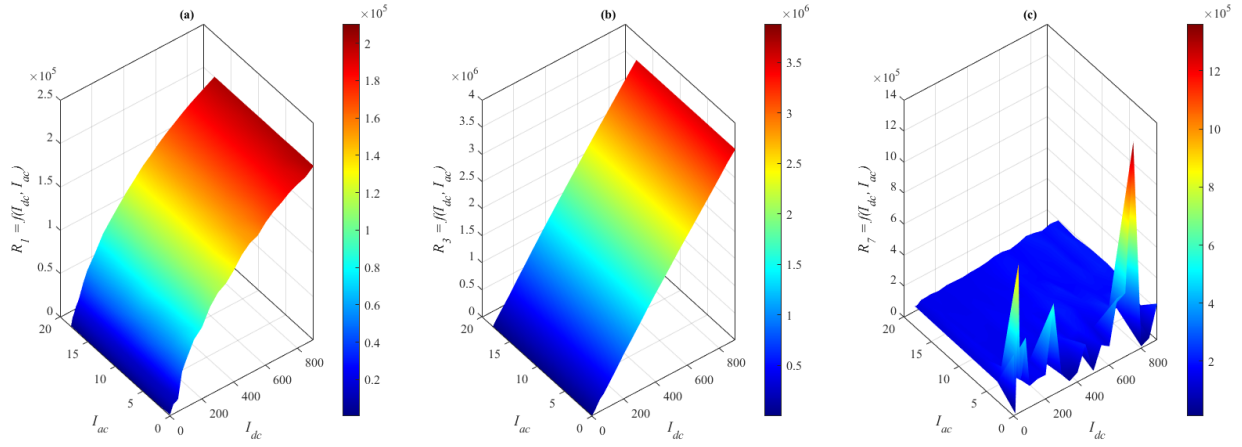
Figure 5.13: Reluctance of: (a) Branch 1, (b) Branch 3, and (c) Branch 7

Table 5.3: PIANN performance matrices

	MSE	MAE	SAE
Training	5.659×10^{-8}	5.7×10^{-8}	5.8821×10^{-8}
Validation	5.5×10^{-8}	1.3813×10^{-8}	8.59917×10^{-9}
Testing	8.29×10^{-9}	1.7067×10^{-8}	1.12246×10^{-8}

Table 5.4: Feature comparison for MA characterization

Methods	Complexity	Computational Need	Accuracy
Two Core Approach	✓	✓	✓
Simple MEC	✓✓	✓	✓✓
Complete MEC	✓✓	✓	✓✓✓
ANN	✓✓	✓✓	✓✓✓✓
PIANN	✓✓✓	✓✓✓	✓✓✓✓
FEA	✓✓✓✓✓	✓✓✓✓✓	✓✓✓✓✓

expression for reactance can be applied for further MA analysis like design optimizations and sensitivity analyses.

Finally, Table 5.4 summarizes the features of different approaches for MA characterization. It is

observed that the PIANN framework is the best approach with moderate computational need and complexity and high accuracy for MA characterization.

Conclusion

This chapter presents ML-based techniques for accurate characterization of MA after providing the background on the common methods used. These techniques include black-box type simple ANN and ANN assisted by a physics-informed analytical method. The results clearly indicate the superiority (accuracy and computational resources) of the presented methods over the conventional analytical and numerical methods. Among the methods, ANN assisted by the analytical model (MEC) is preferred not only because of computational advantage and accuracy but also because of its ability to provide a closed-form solution.

The future work will be the improvement of the closed-form solution to make it more general and capable that the MA characteristics can be worked for every parameter of the MA, including dimensions and material properties. It shows great promise for the design optimization of MA.

CHAPTER 6: 3-PHASE GAPPED CVSR

This chapter is based on the following published works:

S. Pokharel and A. Dimitrovski, "Modeling of An Enhanced Three-phase Continuously Variable Reactor," in *IEEE Power & Energy Society General Meeting*, Montreal, Canada, Aug. 2020;

S. Pokharel and A. Dimitrovski, "Analytical Modeling of a Three-phase Magnetic Amplier-based Continuously Variable Reactor," in *IEEE PES T & D Conference & Exposition*, Chicago, IL, Oct. 2020.

Introduction

This chapter is based on a DOE-funded collaborative work between the University of Central Florida (UCF), University of Tennessee Knoxville (UTK), Oak Ridge National Laboratory (ORNL), and Con Edison. The project is titled, 'Continuously Variable Series Reactor for Distribution System Applications.' In this project, the ability of CVSR to control the power flow has been explored for the meshed distribution system (metropolitan areas) to improve the reliability and economic benefits of grid operation. One of the constraints of CVSR application in the distribution system is space availability, meaning devices like CVSR should fit in the narrow utility vaults in downtown areas. The main tasks of the project were:

1. **System-level analysis to determine CVSR specifications.**

   First, analysis of the Con Edison distributed network was performed to evaluate existing power flow issues and determine potential use cases of CVSR. The overloading of the distribution transformer was the selected problem. The CVSR would be connected on the primary
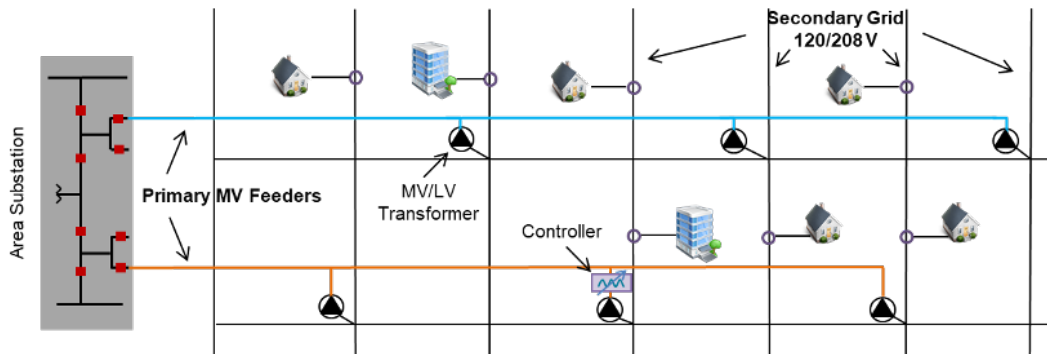
Figure 6.1: Representative distribution system

side of the transformer, which increases the equivalent impedance of the transformer, and the loading will be reduced. Some sensitivity analysis and optimization were run to figure out the ratings of the CVSRs. The most critical specification is the expected reactance variation of CVSR to relieve the overloading of the transformer. The analyses were first conducted on the IEEE 342-node low voltage networked test system [65] and later, the actual Con Edition system is used. Based on the various analyses, CVSR specifications were determined with optimal placement of limited CVSRs.

A representative distribution system, adopted from the ORNL internal report, is shown in Figure 6.1. In this system, the reactance controlling device, like CVSR, is connected between the primary MV feeder and secondary grid. Even though the primary feeders are connected to the area substation radially, the distribution system underneath is mesh connected. By rerouting the power flow through alternate paths, the loading of the MV/LV service transformers can be reduced. We are interested in meshed networks with high load density and high reliability requirements, which are very common in metropolitan areas.

2. **Device-level analysis to find optimal design according to specifications from 1.**

   In this step, an device-level analyses of CVSR models (FEA and MEC) to understand work-

ing principles and propose designs to meet the specifications within the given constraints are carried out.

3. **Validation of the design using a bench-top prototype.**

4. **Based on modeling and testing, analyze the CVSR scalability.**

Only completed works are presented in this chapter. Since the main focus of the work is on reactance modulation and approximate calculation of other factors like loss and induced voltages were not alarmingly unusual, no further analyses were carried out in those regards. And this chapter doesn't include those calculations.

Some of the design decisions made early in the projects were:

- A three-phase CVSR will be designed to meet the space constraint instead of using a bank of three single-phase CVSRs.

- The CVSR will be connected on the primary side of either 500 KVA or 1 MVA transformer with a primary voltage of 13.8kV or 27.6 kV, respectively. In either case, the RMS value of ac supply through CVSR is 20.91 A.

- Each CVSR should change its reactance from 0 to 3 Ω continuously to relieve the transformer overloading. This reactance range of the CVSR was found using sensitivity analysis with optimal placement of the limited number of CVSRs. A team from UTK carried out this part of the work.

Background

The bulk electric power generation, transmission, and distribution are carried out with three-phase systems. Even though small electric loads are single-phase, they are connected in a way to try to balance the load equally on the three-phases of the distribution system. The use of three-phase systems has many advantages compared to the single-phase systems. Therefore, it is important to explore the three-phase derivatives of the saturable core reactors, which were not a part of the previous work on magnetic amplifier based technology. This chapter focuses on the three-phase magnetic amplifier based CVSR.

Three-Phase Continuously Variable Series Reactor

The CVSR can be connected to a balanced three-phase system in two ways. The first way is to use a bank of three single-phase CVSRs in each phase of the polyphase network. The second approach is to use a three-phase CVSR. For most of the applications, the second method is preferred because of the advantages it offers in terms of cost and space requirements. The trade-off of using a three-phase CVSR is the increased complexity both in design and operation. Figure 6.2 shows a possible three-phase CVSR.

The reactor is made up of a high permeability ferromagnetic core with a special arrangement of windings around the legs. The design of the reactor is symmetrical with five legs: three of them are with gaps and the remaining two are gapless. The gapless ferromagnetic legs provide the easiest path for the magnetic flux flow within the device. The non-ferromagnetic gaps with magnetic properties same as that of free space are provided in selected legs. Generally, multiple layers of non-ferromagnetic materials (ceramic) are used to fill the gaps. For the sake of simplicity, the term 'Air Gap' is used and represented by a single gap in Figure 6.2. The three phases of the AC circuit
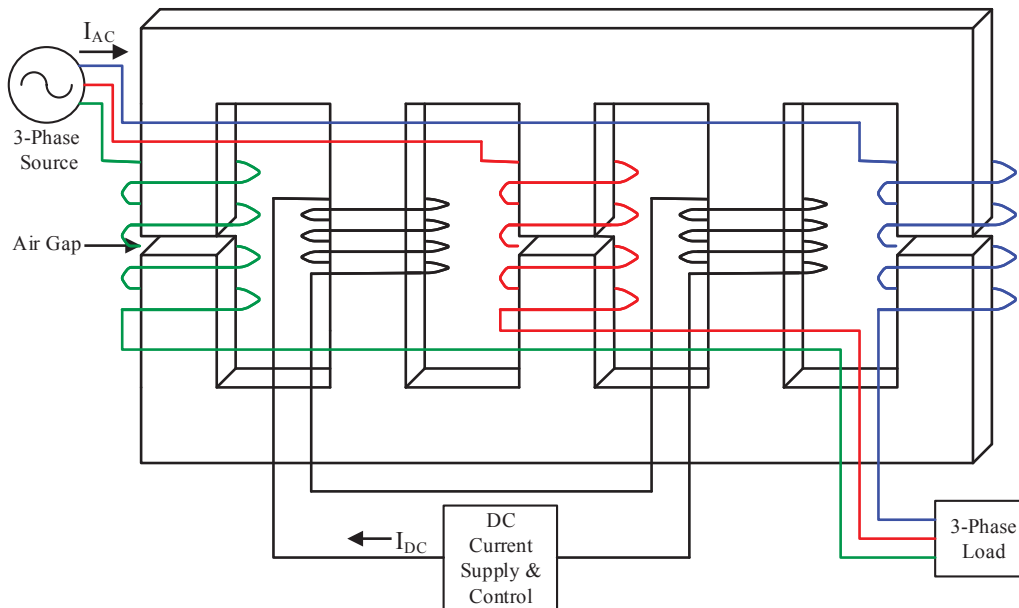
Figure 6.2: Five-legged three-phase CVSR connection

to be controlled are connected to three AC windings wound around the gapped ferromagnetic core legs. Each gapless leg of the reactor has a DC winding. The direction of currents through the DC windings are such that they produce flux in the same direction, which is interesting about this design. The numbers of turns in the AC and DC windings are selected to obtain the desired inductance regulation range. In accord with the ac ratings of the reactor, its rated load current and unsaturated inductance, a controlled DC source powers the DC windings. Because the reactor is connected in series with a balanced three-phase circuit, the five-legged core configuration is chosen because it offers the same variable reactance in each phase. Special attention is provided to limit the total induced voltage on the DC windings as well.
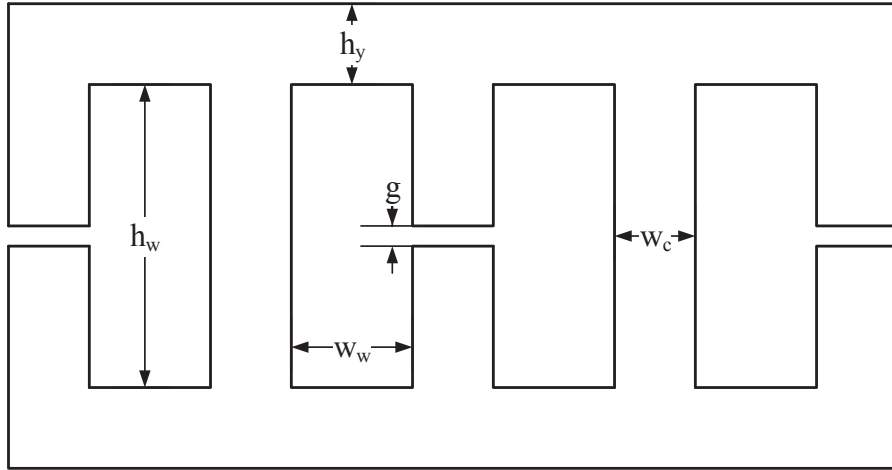
Figure 6.3: Cross-section of five-legged three-phase CVSR core

Magnetic Equivalent Circuit

The magnetostatic field analysis is performed on a three-phase CVSR over a period of an AC cycle. The cross-section of the CVSR with some characteristic geometric variables is as shown in Figure 6.3. This five-legged reactor houses four core windows with width w_w and height h_w. The height of both yoke and the base of the reactor is h_y. The legs of the symmetrical device have the same dimensions of width w_c and depth of d_c into the page. The height of the gaps beneath AC windings is g.

One possible magnetic equivalent circuit (MEC) for the reactor of Figure 6.2 is shown in Figure 6.4, The circuit is sufficiently accurate, yet simple. The MEC is composed of reluctances and magnetomotive forces (MMFs), arranged in a particular way so that it could represent the reactor clearly and easily. There are five MMF sources; three of them are sinusoidally varying in time representing the AC windings while the remaining two are constant representing the DC windings. The AC windings have the same number of turns: N_{ac}, creating a balanced three-phase source and
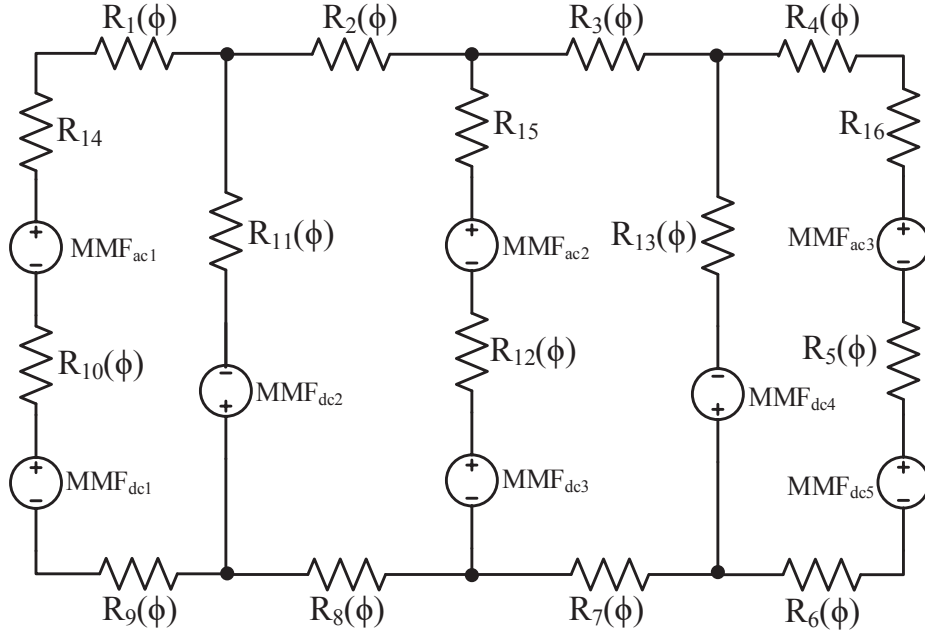
Figure 6.4: Magnetic equivalent circuit

a three-phase load with the peak current of I_P. The peak current in the AC windings varies, of course, according to the voltage level and the load at the location the device is placed. Each DC winding also has the same number of turns of N_{dc}, and the supply of the same current of I_{dc} is determined by the DC supply and control system, according to the application need. Therefore, in the MEC:

$$MMF_{ac1} = N_{ac}I_P cos(wt + \frac{2\pi}{3}) \tag{6.1a}$$

$$MMF_{ac2} = N_{ac}I_P cos(wt) \tag{6.1b}$$

$$MMF_{ac3} = N_{ac}I_P cos(wt - \frac{2\pi}{3}) \tag{6.1c}$$

$$MMF_{dc1} = MMF_{dc2} = N_{dc}I_{dc} \tag{6.1d}$$

Core Piece Reluctances

The representative reluctances of the symmetrical reactor according to (3.11) are given by (6.2). As these reluctances are dependent on the flux flow through them, they are represented as a function of ϕ.

$$R_1(\phi) = \frac{w_w + w_c}{K_A d_c h_y \mu_B(\frac{\phi}{K_A d_c h_y})} \tag{6.2a}$$

$$R_5(\phi) = \frac{h_y + h_w - g}{K_A d_c w_c \mu_B(\frac{\phi}{K_A d_c w_c})} \tag{6.2b}$$

$$R_{11}(\phi) = \frac{h_y + h_w}{d_c w_c \mu_B(\frac{\phi}{d_c w_c})} \tag{6.2c}$$

In the MEC, $R_1(\phi) = R_2(\phi) = R_3(\phi) = R_4(\phi) = R_6(\phi) = R_7(\phi) = R_8(\phi) = R_9(\phi)$, $R_5(\phi) = R_{10}(\phi) = R_{12}(\phi)$ and $R_{11}(\phi) = R_{13}(\phi)$.

Here, particular attention should be given to the constant K_A in (6.2). Because of the arrangement of the device, the flux flow is higher in the gapped legs and yokes (top and bottom) than the gapless legs. As the reactor is made to operate in the linear and non-linear regions, the core reactors should incorporate this dynamic nature of the flux flow in the ferromagnetic cores. For simplicity, the use of constant ($K_A = 1.12$) represents the dynamic nature for both saturated and unsaturated core pieces. It implies an increased virtual cross-sectional area of the selected core pieces due to increased leakage flux.

Air-Gap Reluctance

The air-gap reluctance is the magnetic resistance to the streamlined flux flow across the air-gap cross sections. It is a constant reluctance, independent of the flux flow through it. This reluctance

according to (3.4) is:

$$R_g = \frac{g}{d_w w_c \mu_0} \tag{6.3}$$

The reluctance in (6.3) does not represent the reluctance due to the spreading flux in the proximity of the corners of the gap in all directions. This flux is usually called fringing flux. A higher accuracy of the proposed MEC can be achieved if the air-gap reluctance incorporates the fringing flux. As a result of it, the active cross-sectional area of the air-gap increases, and there is a reduction of the air-gap reluctance. According to [9], the effective air-gap reluctance is:

$$(R_g)_{eff} = \frac{R_g}{1 + 4R_g P_{fring}} \tag{6.4}$$

where, P_{fring} is the fringing permeance, given by:

$$P_{fring} = \frac{\mu_0 d_c}{\pi} log \left\{ 1 + \frac{\pi(h_w - g)}{2g} \right\} \tag{6.5}$$

In the MEC, $R_{14} = R_{15} = R_{16} = (R_g)_{eff}$.

94

Table 6.1: Three-phase CVSR parameters

Parameters	Symbol	Value
Height of window	$h_w(in)$	14.72
Width of window	$w_w(in)$	2.2
Width of leg	$w_c(in)$	3
Height of yoke and base	$h_y(in)$	3
Depth of Core	$d_c(in)$	3
Height of Gap	$g(in)$	0.06
Number of DC turns	N_{dc}	39
Number of AC turns	N_{ac}	42
Current through the AC winding	$I_P(A)$	30
Angular System frequency	$\omega(rad/sec)$	120π

A = Ampere, in = inch

MEC Validation

A five-legged three-phase CVSR with the parameters shown in Table 6.1 is considered. The core of the reactor is made of Si-Fe M36 whose permeability characteristics are according to [47]. After the reluctances and MMFs of the MEC are determined, the mesh circuit analysis is done for the variation of the control current over a period of the AC cycle. The branch flux solutions are then used to find fluxes through the gapped legs where the AC windings are wound. For a unit increment in one AC MMF while keeping the other sources constant, the product of the number of AC turns and the differential flux flow gives the incremental inductance for that winding. The incremental inductance for a DC supply is the average of the incremental inductance values over a period the AC cycle for the same DC supply. This nested iterative process is carried out using to determine the incremental inductance for a wide range of DC variation.

A three-dimensional finite element analysis model has been developed for the same reactor, as shown in Figure 6.5. Here, the surrounding region for the FEA is assumed to be 100% of the core dimensions in each direction. The figure shows the flux density vector distribution throughout

the core for DC supply = 10 A at $t = 0$ s. The differential inductance per phase is found using this model for a given DC variation, and used for benchmarking purpose. The FEA modeling is carried out using ANSYS Maxwell. This kind of modeling is instrumental in analyzing the flux flow throughout the device which can be of significant help in coming up with a better analytical model.
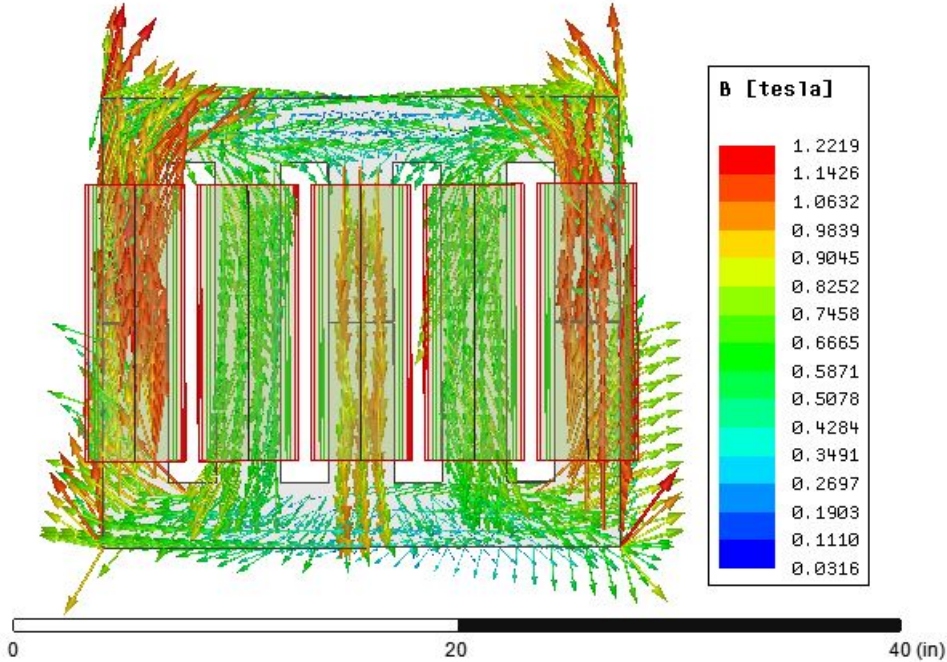
Figure 6.5: FEA model

Figure 6.6 shows the inductive reactance value comparisons using both of the approaches for the full range of control current variation.

A few observations can be made from this figure:

1. The reactance of the reactor is maximum when the DC supply is zero, and the reactance keeps decreasing with the increased DC supply. Therefore, depending on the reactance requirement, the reactor can be made to operate in pre-saturation mode, post-saturation mode,

96
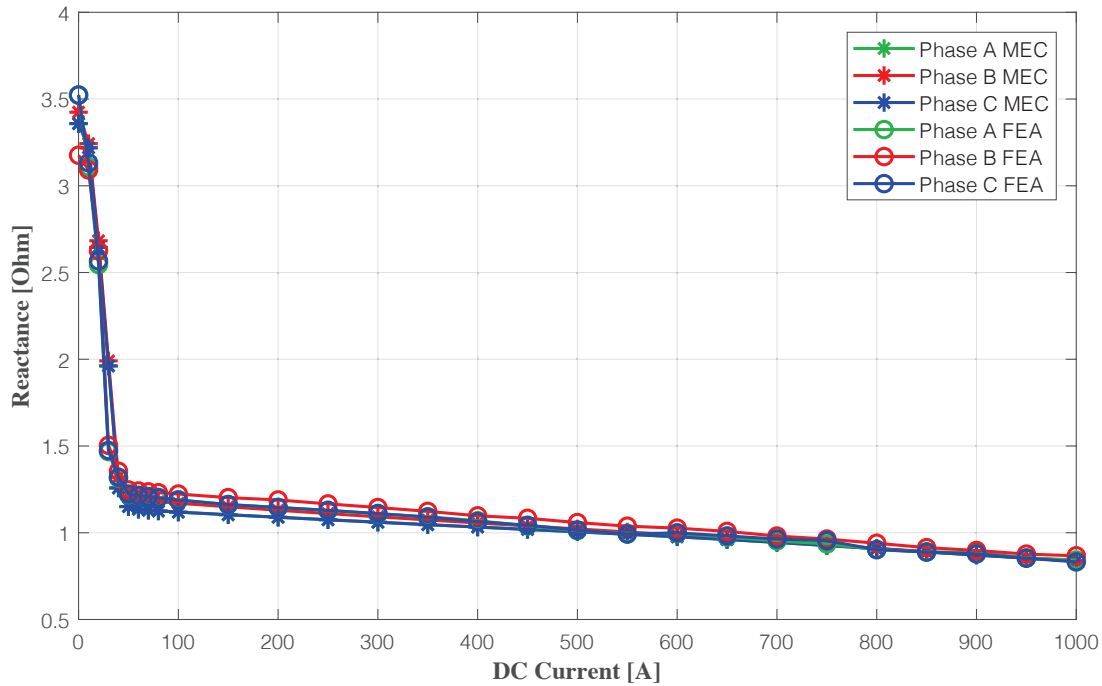
Figure 6.6: Reactances comparison

or anywhere in between.

2. The reactance of the device can be varied from 3.4 to 0.84 Ω by changing the control current from 0 to 1000 A. The reactance modulation is quick for a small DC supply when the core is unsaturated, and the reactance modulation is slow for higher DC supply when the core is saturated.

3. As a metric of the overall accuracy for both approaches, the root mean square error (RMSE) has been used to express the differences in reactance values for each pair of phases as shown in Table 6.2. As expected, the overall difference between the reactances in the outer legs (phases A and C) are very small as they should theoretically be the same due to the system symmetry. Furthermore, for the same reason, the differences between the reactances in the outer legs and the middle leg (phase B) should also be the same. The errors are mostly

Table 6.2: RMS errors in self-reactance pairs

	phase A-phase B	phase B-phase C	phase C-phase A
FEA	0.0742 Ω	0.0742 Ω	0.0083 Ω
MEC	0.0351 Ω	0.0351 Ω	0.0046 Ω

Table 6.3: Overal RMS errors in self-reactances

	phase A	phase B	phase C
RMSE	0.1105 Ω	0.1145 Ω	0.1082 Ω

concentrated around the knee point of the B-H curve of the ferromagnetic core. An important point to note here that proves the consistent performance of the MEC model is that its RMS errors are smaller compared to the FEA approach.

4. Total errors between the values for the self-reactances for each phase from both approaches using the same RMSE metric from above are shown in Table 6.3. These results show that the values from both approaches are fairly close to each other, as can be concluded from the figure.

The small overall errors in the inter-phase comparison (Table 6.2) and inter-approach comparison (Table 6.3) prove the validity of the presented MEC model.

Enhanced Three-phase CVSR

This work builds on the previous work with the improvements in the reactance characteristic. Multi-magnetic materials with different magnetic properties have been used in the core in some instances to improve the mechanical strength of an electromagnetic device, but they have been rarely used to improve the magnetic property of the device. Recently, micro-scale and high-frequency

98

magnetic device design have used multi-magnetic materials to adjust magnetic properties for some special applications [66]. This concept of multi-magnetic material has been explored here in the three-phase CVSR design for achieving a better reactance characteristic.

Improved CVSR Design

A novel and improved three-phase variant of the CVSR is shown in Figure 6.7. This symmetrical device consists of a high permeability ferromagnetic core with five legs: two outer gapless legs, and three inner gapped legs. The non-ferromagnetic gaps are placed in the three middle legs. In practice, the gaps are composed of multiple layers from a ceramic material. However, for simplicity, the gaps in the core are represented by an aggregated gap in each leg and indicated by 'Air Gap' in Figure 6.7, without considering the non-ferromagnetic material. Furthermore, the ferromagnetic core is considered to be solid, which is never the case in practice due to the core losses. Three-phase winding coils, connected in series in a three-phase power circuit, are wound above the DC coils around the gapped legs. The DC coils in the gapless outer legs have 150% the number of turns in the inner coils, with direction of the bias flux opposite to that through the inner coils. This way, the DC magnetomotive forces (MMFs) will balance out throughout the device. The DC bias current is supplied from the DC current supply & control system, whose output controls the reactance. The number of AC winding turns is chosen based on the required reactance range, whereas special attention is paid in the selection of the number of DC winding turns to minimize the bias current while keeping the residual induced voltage within acceptable limits.
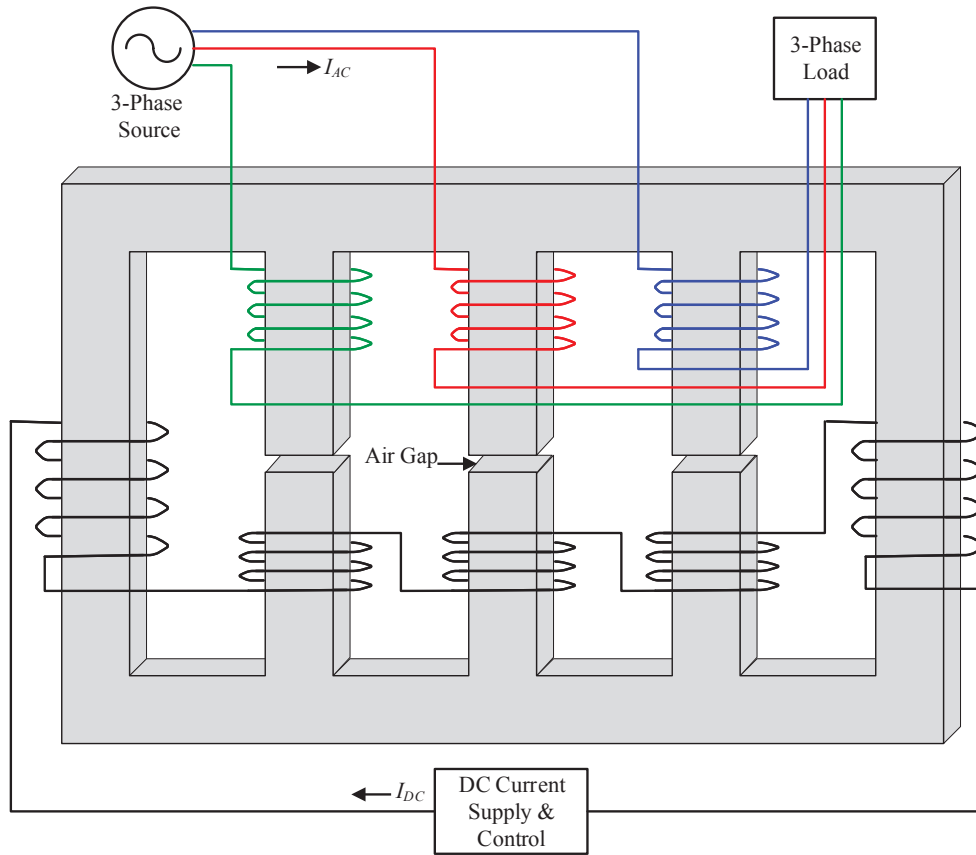
Figure 6.7: Three-phase continuously variable reactor

Magnetic Equivalent Circuit

One possible magnetic equivalent circuit (MEC) of the three-phase CVSR described in the previous section is shown in Figure 6.8. The MEC is a combination of lumped magnetic circuit components, MMFs and reluctances, in such a way that it represents the device characteristics in a simple but accurate manner. There are eight MMF sources: five of them represent DC winding coils, and the remaining three are parts of the sinusoidal time-varying AC winding. Each AC winding coil has N_{ac} number of turns. The DC winding has two groups of coils with turns represented as factors of N_{dc}. The peak current through the AC winding, which is a function of the system load and the

100

voltage level, is I_p. For the sake of simplicity, the alternating currents in the power system are assumed to be balanced. The selection of the current through the DC winding, I_{dc}, is based on the required reactance characteristics of the device and the DC supply and control system.
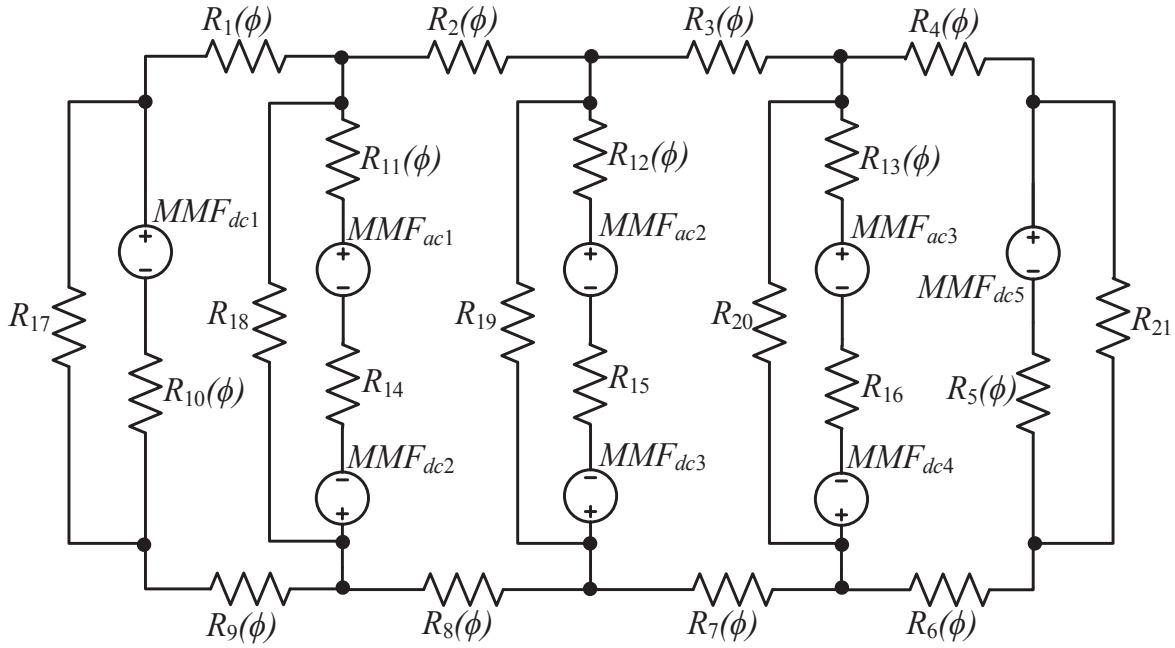
Figure 6.8: Magnetic equivalent circuit

The complete sets of MMFs in the MEC are given by (6.6):

$$MMF_{dc1} = MMF_{dc5} = \frac{3}{2}N_{dc}I_{dc} \tag{6.6a}$$

$$MMF_{dc2} = MMF_{dc3} = MMF_{dc4} = N_{dc}I_{dc} \tag{6.6b}$$

$$MMF_{ac1} = N_{ac}I_p cos(wt + \frac{2\pi}{3}) \tag{6.6c}$$

$$MMF_{ac2} = N_{ac}I_p cos(wt) \tag{6.6d}$$

$$MMF_{ac3} = N_{ac}I_p cos(wt - \frac{2\pi}{3}) \tag{6.6e}$$

Core-piece reluctances

Due to the symmetrical geometry of the device, the representative ferromagnetic core reluctances, using (3.11), are given by (6.7).

$$R_1(\phi) = \frac{w_w + w_c}{\mu_B(\frac{\phi}{d_c h_y})d_c h_y} \tag{6.7a}$$

$$R_5(\phi) = \frac{h_w + h_y}{\mu_B(\frac{\phi}{d_c w_c})d_c w_c} \tag{6.7b}$$

$$R_{11}(\phi) = \frac{h_w + h_y - g}{\mu_B(\frac{\phi}{d_c w_c})d_c w_c} \tag{6.7c}$$

For this device, $R_1(\phi) = R_2(\phi) = R_3(\phi) = R_4(\phi) = R_6(\phi) = R_7(\phi) = R_8(\phi)$, $R_5(\phi) = R_{10}(\phi)$, and $R_{11}(\phi) = R_{12}(\phi) = R_{13}(\phi)$.

One important point to make here is that the yoke reluctances which turn out to play small role in the device characteristic, also include the reluctances of the air-spaces around the yoke in all directions as parallel combinations.

Leakage Reluctance

The presence of multiple different MMFs within this complex device and the property of saturation make the leakage reluctances an essential component for accurate analytical representation. The leakage reluctances in the three-phase CVSR can further be sub-categorized into the following types.

Air-Gap Reluctances

The air reluctance with the fringing effect, $(R_g)_{eff}$, is found using (6.4), as discussed for the for previous three-phase CVSR, in one the former sections.

In this MEC, $R_{14} = R_{15} = R_{16} = (R_g)_{eff}$.

Slot-leakage Reluctances

The slot leakages which significantly contribute to the leakage flux, represent the fluxes that leak within the window space [43]. Generally, the slot leakage reluctances are represented as a combination of two orthogonal components, horizontal and vertical slot, which are found as reciprocals of (6.8a) and (6.8b), respectively, following the procedure from [43] for one half of the window space.

$$P_{hsl} = \frac{\mu_0 d_c \left(3h_w - 2h_c\right)}{24w_w} \tag{6.8a}$$

$$P_{vsl} = \frac{\mu_0 d_c \left(\frac{3}{2}w_w - 2w_{coil}\right)}{3h_w} \tag{6.8b}$$

where, w_{coil} is width of the coil. The permeances (6.8a) and (6.8b) represent the flux leakage within the window space only. However, there is flux leaking from the front and back of the window, as well. The permeances associated with these leakages can be represented using (6.9a) and (6.9b) from [40], [67], again for one half of the window space.

$$P_{hslf} = \frac{\mu_0 \left(3h_w - 2h_c\right)}{6\pi} log \left(1 + \frac{2\pi w_c}{w_w}\right) \tag{6.9a}$$

$$P_{vslf} = \frac{\mu_0 \left(\frac{3}{2}w_w - 2w_{coil}\right)}{3\pi} log \left(1 + \frac{\pi h_y}{h_w}\right) \tag{6.9b}$$

Therefore, the total slot leakage can be found by combining both of these components as:

$$\left(P_{hsl}\right)_{eq} = P_{hsl} + 2P_{hslf} \tag{6.10a}$$

$$\left(P_{vsl}\right)_{eq} = P_{vsl} + 2P_{vsif} \tag{6.10b}$$

where, the multiplication factor for P_{hslf} and P_{vslf} takes into account flux leakage from the front and the back of the window.

External Adjacent Leakage Reluctances

These are the reluctance due to the leakage flux associated with the bundle of conductors adjacent to the core on the front and the back of each leg. The permeance for this flux is given by (6.11) from [43], [67].

$$P_{eal} = \frac{\mu_0 l_e}{\pi w_{coil}^2} \left[\frac{r_1^2}{2} - \frac{h_c r_1}{\pi} + \frac{h_c^2}{\pi^2} \log \left(\frac{h_c + \pi r_1}{h_c}\right) + w_{coil}^2 \log \left(\frac{h_c + \pi h_{el}}{h_c + \pi r_1}\right) \right] \tag{6.11}$$

where, $h_{el} = h_y + (h_w - h_c)/2$ and $r_1 = min(h_{el}, w_{coil})$.

The combined effect of the flux leakages, except the air-gap leakage, is represented in the MEC by

a single reluctance for each leg. Here,

$$R_{17} = R_{18} = R_{19} = R_{20} = R_{21} = \frac{0.5}{(P_{hsl})_{eq} + (P_{vsl})_{eq} + P_{eal}} \tag{6.12}$$

Model Validation

For this purpose, a three-phase five-legged CVSR with the parameters shown in Table 6.4 is considered. The ferromagnetic material used for the comparison is Si-Fe M36, whose magnetic characteristics in terms of permeability function parameters are obtained from [47].

Table 6.4: Enhanced three-Phase CVSR parameters

Parameters	Symbol	Value
Height of window	h_w(in)	14.72
Width of window	w_w(in)	2.2
Width of coil	w_{coil}(in)	0.15
Width of leg	w_c(in)	3
Height of yoke and base	h_y(in)	3
Depth of Core	d_c(in)	3
Height of Gap	g(in)	0.06
Number of DC turns	N_{dc}	39
Number of AC turns	N_{ac}	40
Current through the AC winding	I_p(A)	30
Angular System frequency	ω(rad/sec)	120π

A = Ampere, in = inch

For benchmarking, a three-dimensional FEA model has been created for this CVSR using ANSYS Maxwell as shown in Figure 6.9. The figure shows the flux density distribution throughout the device for an instant of AC and DC supply with some specific settings, including the definitions of the region and the error tolerance. The FEA model like this is essential reference for the accuracy of the analytical model.
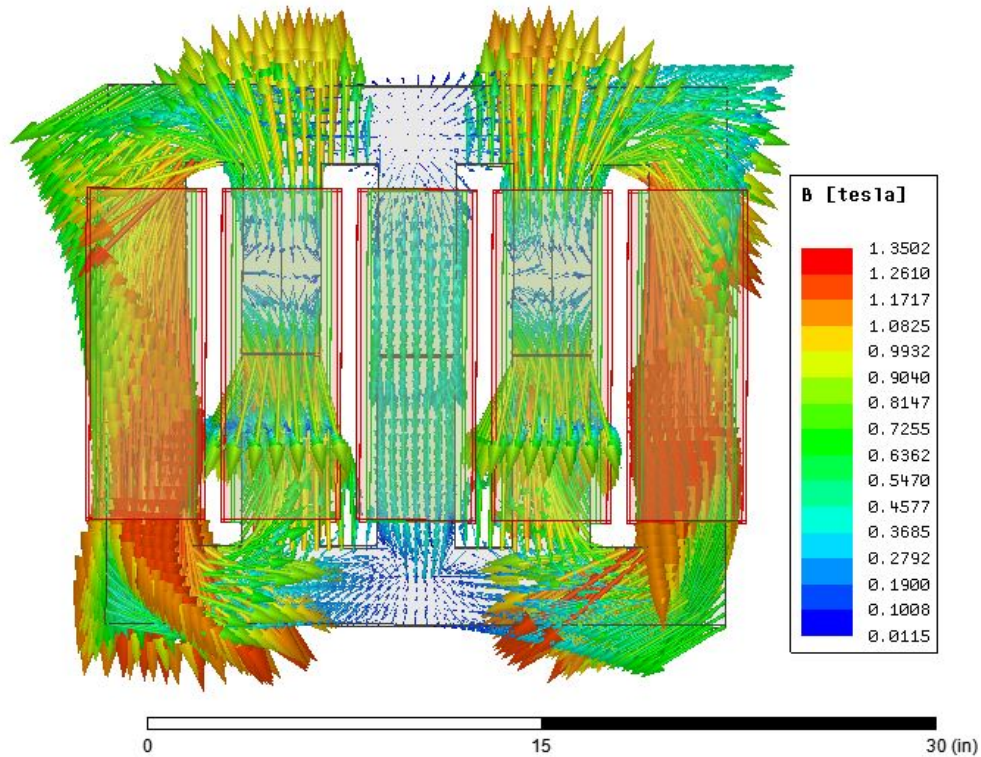
Figure 6.9: 3-D FEA model of an enhanced 3-phase CVSR

For the same CVSR, the proposed MEC model has also been developed with all the elements previously defined. MEC analysis has been performed for each control current over an AC cycle. Then the average of incremental inductance is found for each phase using the differential flux flow with respect to a unit change in the AC current. This iterative process is carried out using MATLAB over the complete range of control current variation. Results from both models are summarized in Figure 6.10.

From Figure 6.10, it can be seen that the reactance is maximum when the DC MMF is zero, and it decreases with the increase of the control MMF. The reactance regulation is found to be from 3.15 Ω to 0.06 Ω with DC MMF change from 0 to nearly 7800 AmpTurns. However, the rate of change of reactance for the DC MMF is not uniform but has several slopes. This indicates the different core

106
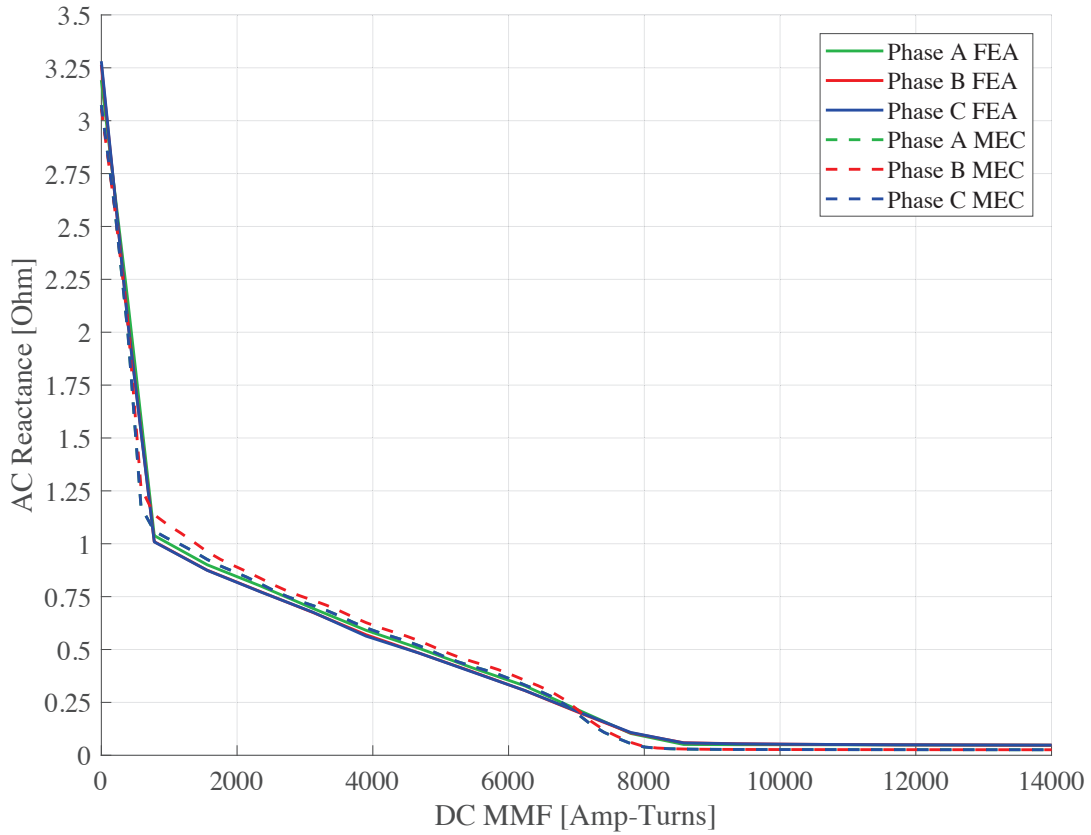
Figure 6.10: Reactance characteristics

regions go into saturation at different DC MMF values because of multiple simultaneous MMFs and the structure of the core. It is also evident that the results from both MEC and FEA approaches are almost the same for the whole range of control MMF variation. Furthermore, the reactances for each phase are very close to each other. This comparison proves the validity of the proposed CVSR model and its ability to reproduce the highly nonlinear behavior over the whole range. Based on the application need, the CVSR can operate in any of the three modes, pre-saturation mode, post-saturation mode, or anywhere in between.

Ferromagnetic Core Adaptation

The latest three-phase CVSR presented has a better reactance regulation compared to the previous CVSR from [29]. Nevertheless, the multi-slope reactance modulation characteristic is not preferred because of the negative impact it can have on the control system and the possibility of harmonics generation within the device. Two core adaptation approaches are discussed to eliminate the negative impact of multi-slope reactance modulations.

Heterogeneous Core CVSR

The design of a CVSR using heterogenous ferromagnetic material is explored here to obtain a smoother reactance curve. For that purpose, the core has been divided into several parts, and a variety of materials have been tried for each one of them. One such combination is where the outer flux path material is chosen to be from Hiperco50, and the inner gapped legs are made of M36. Both materials are a class of Si-Fe with ferromagnetic characteristics shown in Figure 4.6 [47].

From Figure 4.6, it can be seen that the Hiperco50 has a higher saturation point than M36. Also, the M36 is almost flat in the saturation region, whereas Hiperco50 exhibits a small incremental increase until full saturation. Because of these different characteristics, the reactance characteristic of the reactor is altered. The new reactance curve, using both FEA and MEC approaches, is shown in Figure 6.12 for the CVSR with the same parameters.

The modified CVSR reactance curve is smoother than the previous one, and the point of saturation is reached with a lower control MMF from before. As a result, a smaller DC bias power supply can be used for the same wide range of control of the device. Again, the curves from both approaches are almost the same, except in the region around the knee point. This result points to a somewhat higher leakage flux in one of the components of the MEC model which needs more refinement and
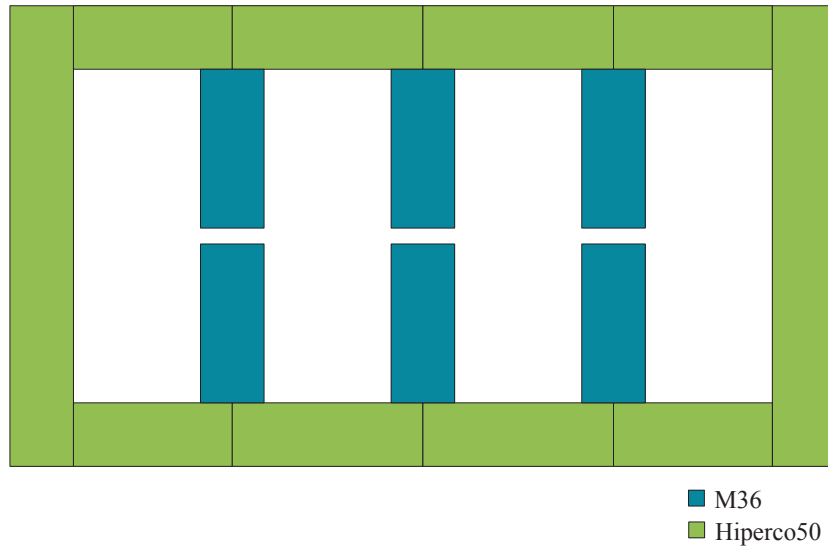
Figure 6.11: Materials used in the core: front view

further investigation.

Homogeneous Core CVSR

The front view of the reactor in Figure 6.13 is drawn to scale to show the actual proportion of the dimensions of Si-Fe M6 Core. However, the copper windings are not drawn to scale; instead, they only represent the exact current around the core (irrespective of current density).

Table 6.5 shows the differences between the dimensions of this homogenous CVSR with the previous design of the heterogenous CVSR to give a better understanding of the system. Here both designs include the same window dimension (width $\times$ height). Also, the core depth of both of the designs is the same (3").

The dimension differences indicate that the overall core dimension (volume) has increased by 16 % while the core material volume has increased by 20% for the homogeneous CVSR compared to

109
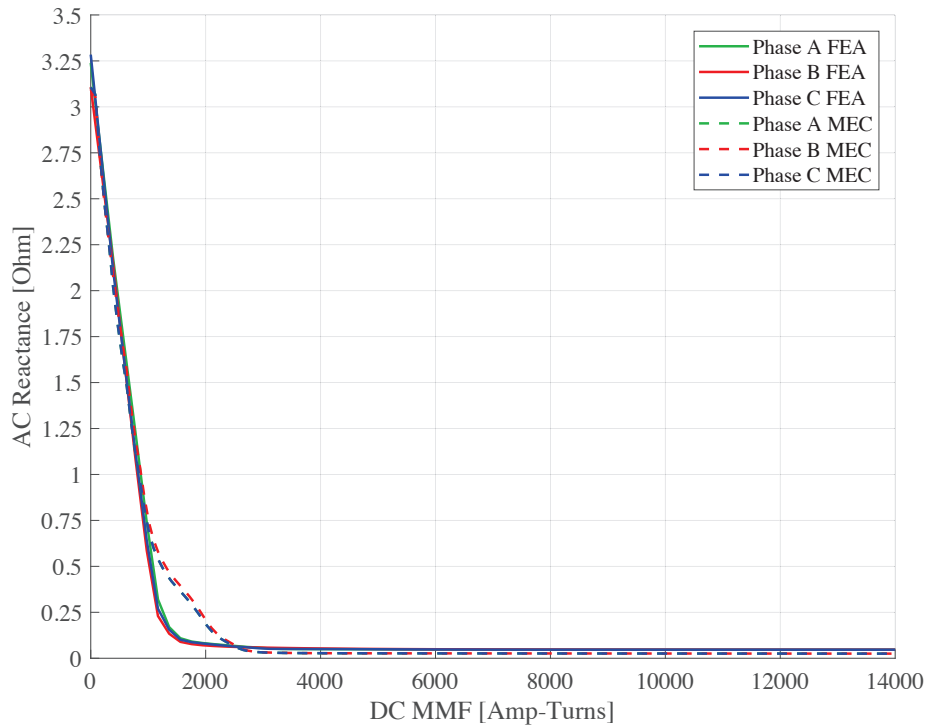
Figure 6.12: Modified reactance characteristics

the heterogeneous CVSR.

Note: For the sake of simplicity, the rectangular solid core is used throughout this study. However, in practice, the cores are always laminated to minimize the eddy current loss.

Table 6.5: Core adoptation dimension comparison

Parameters	Homogeneous Core CVSR (in)	Heterogeneous Core CVSR (in)
Core height	23.06	20.72
Middle leg width	2.7	3
Outer leg width	4.17	3
Yoke height (top & bottom)	4.17	3
Total width	33.44	32
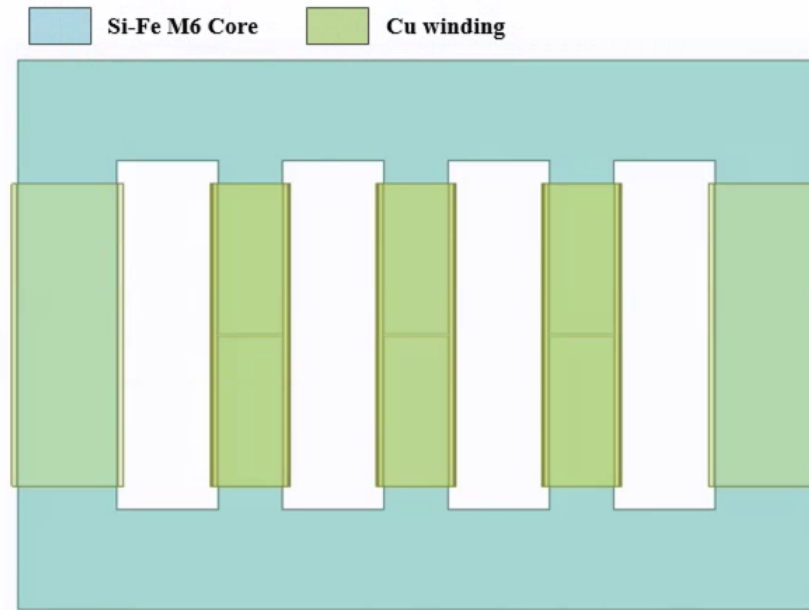
Figure 6.13: Dimensions of the core structures

Also the materials used for both core adaptations were chosen because the characteristics of these materials were readily available for our analysis. Based on the understanding of these setups, the ferromagnetic core magnetic materials can be selected that would fit the specific needs in terms of magnetic saturation, cost, availability, and other possible properties of interest.

Conclusion

This chapter discusses a novel, three-phase rendition of the continuously variable series reactor with an analytical model developed based on the magnetic equivalent circuit approach. Based on the reactance regulation requirement, balanced reactances between the phases, and the induced voltage on the DC windings, a five-legged configuration for the three-phase reactor is selected. The analysis of the mesh circuit following the determination of the elements of the MEC, show the
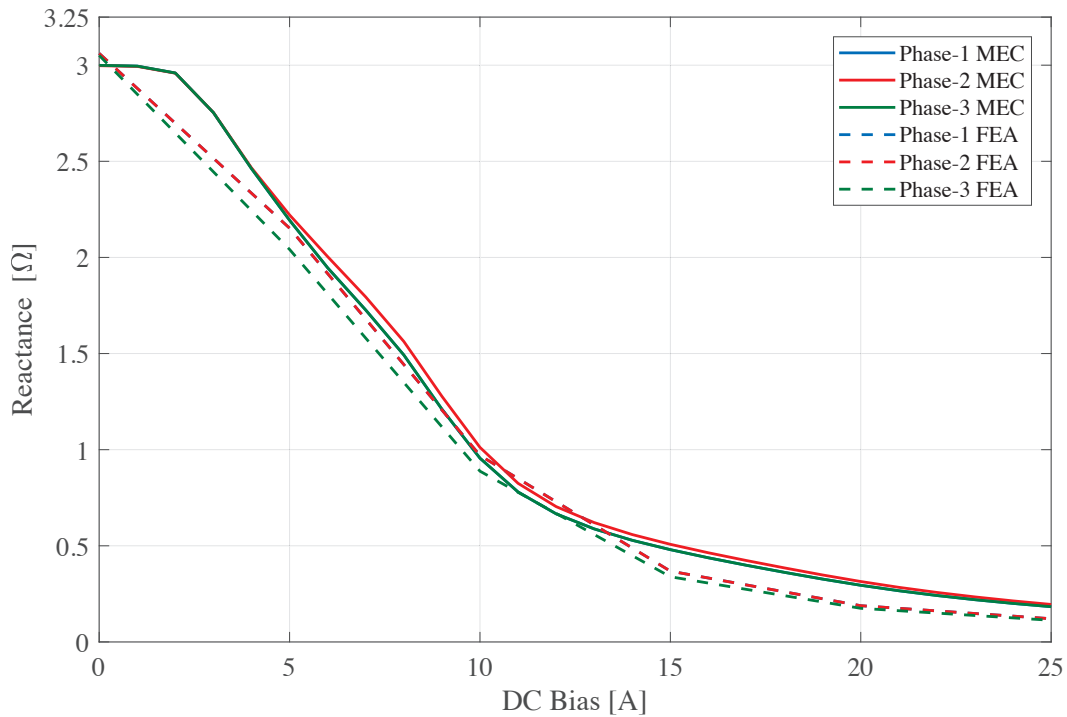
Figure 6.14: Reactance comparison

reactance regulation of the device. The incremental inductive reactance for a wide range of control current was used to validate the presented MEC by comparing it against the FEA results for a sample device. The results suggest both of the approaches produce almost the same reactances, validating the proposed MEC.

Later in this chapter, a new configuration of a three-phase five-legged CVSR is proposed with the improved reactance regulation range compared to the previous configuration. An analytical model for the device is presented based on the MEC. The model has been validated by comparing the differential inductances with those obtained using FEA. Adaptation of the ferromagnetic core using different mix of materials is explored to achieve a better reactance characteristics, again verified using FEA.

Future work will accurately calculate other relevant factors like the induced voltage, total loss, thermal analysis, etc., for the exact benchtop CVSRs.

CHAPTER 7: GAPLESS FERROMAGNETIC CORE REACTORS

This chapter is based on the following published works:

S. Pokharel and A. Dimitrovski, "A Gapless Ferromagnetic Core Reactor - Magnetic Equivalent Circuit & Inductance", in *IEEE Power & Energy Society General Meeting*, Atlanta, GA, Aug. 2019;

S. Pokharel and A. Dimitrovski, "Analytical Modeling of a Gapless Ferromagnetic Core Reactor," in *IEEE Transactions on Magnetics*, vol. 56, issue 2, 2020.

Introduction

The novel type of gapless ferromagnetic core reactor (GFCR) addresses the issues of gaps in standard power reactor designs. A GFCR has specially arranged multi-coil winding(s) in the same simple magnetic circuit configuration as the standard one, but without gaps in the core. Both types of reactors, the standard ferromagnetic core with gaps and the GFCR are depicted in Figure 7.1 in a simplified form. Here the single-phase ferromagnetic core reactor derived from a three-phase standard ferromagnetic core reactor is referred to as a standard reactor.

The ac winding of the GFCR consists of two coils wound on the same leg of the reactor connected in a counter-series connection. The two coils create magnetic fluxes in opposite direction that repel each other and close through the air space in the windows as shown in Figure 7.1b. In effect, they create a virtual gap in the middle of the leg between the coils that is extended through the core window opening. Therefore, the saturation of the ferromagnetic core is prevented even at large load currents without any gap in it.

For large power applications, the non-symmetrical magnetic circuit in Figure 7.1b may produce

(a) Standard reactor   (b) GFCR
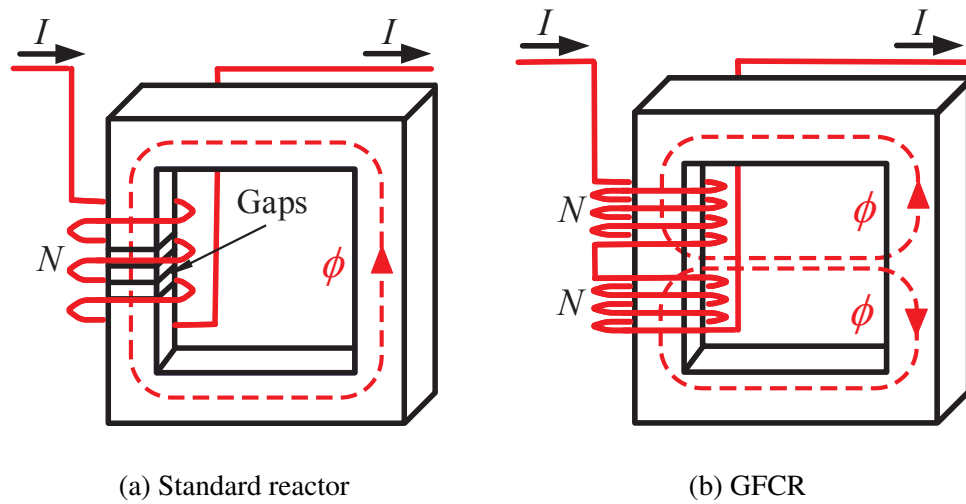
Figure 7.1: Simplified single-phase magnetic circuits

unwanted flux flow through the device container. This will create extra losses and heat. Therefore, for a single-phase reactor, it is preferable to maintain the magnetic circuit symmetry using the arrangement shown in Figure 7.2. Two cores with one-half cross-section of the core in Figure 7.1b can be arranged back-to-back. This configuration does not require additional core material and the fluxes produced in the central leg will flow symmetrically in the outer legs.

The single phase GFCR shown in Figure 7.2 can be installed in one of the phases of a poly-phase ac power system and a bank of three single-phase reactors can be used in three-phase applications. Alternatively, for applications in balanced symmetrical three-phase systems, a single three-phase reactor can be built with a three-legged core similar to the construction of a three-phase core-type transformer, as shown in Figure 7.3.
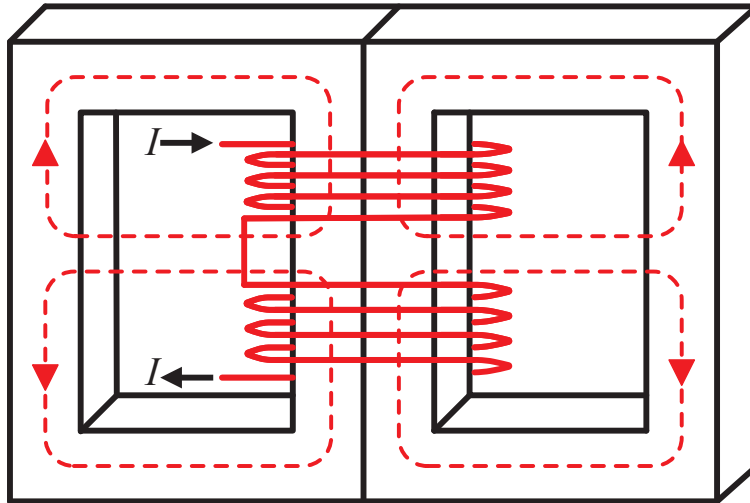
Figure 7.2: Improved single-phase GFCR
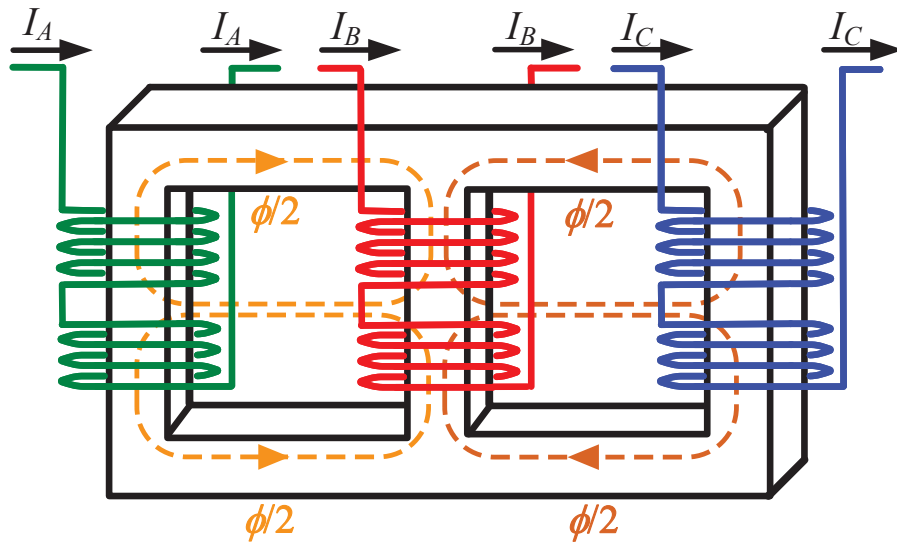
Figure 7.3: Three-phase GFCR
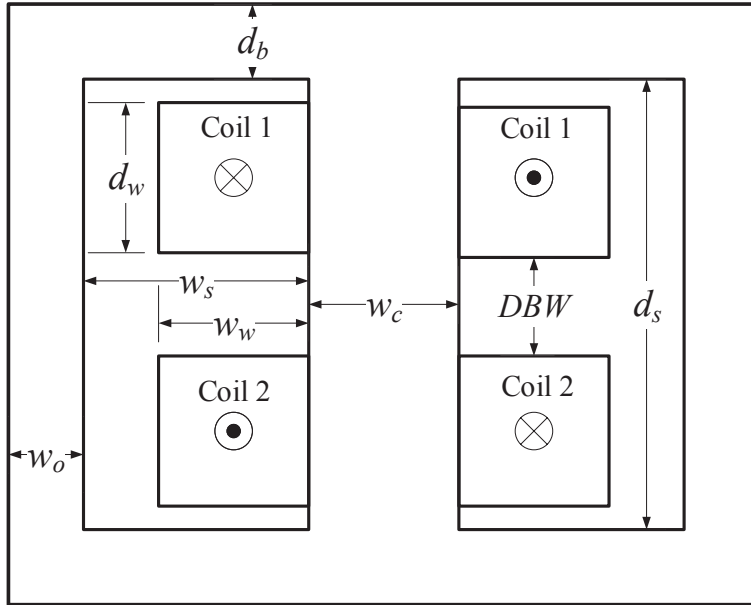
Figure 7.4: GFCR model front view

Magnetic Equivalent Circuit (MEC)

The magnetostatic field analysis of GFCR is preformed on a simple single-phase device model shown in Figure 7.2 with cross-section shown in Figure 7.4. The winding coils in the central core leg are assumed to have rectangular profile and are next to the core in all directions for the sake of simplicity. The rectangular core has two window slots of width w_s and height d_s that house two coils separated by a vertical distance denoted as '*DBW*'. The circled 'x' and circled 'o' indicate the direction of current flow through the bundle of conductors with width w_w and height d_w extending l_c into the page. The width of the central leg is w_c while that of outer legs are w_o. The height of the yoke is denoted by d_b.

Figure 7.5 shows one possible MEC for the GFC reactor described above.

For GFCR, where the magnetic energy is primarily stored in the surrounding space rather than in

117
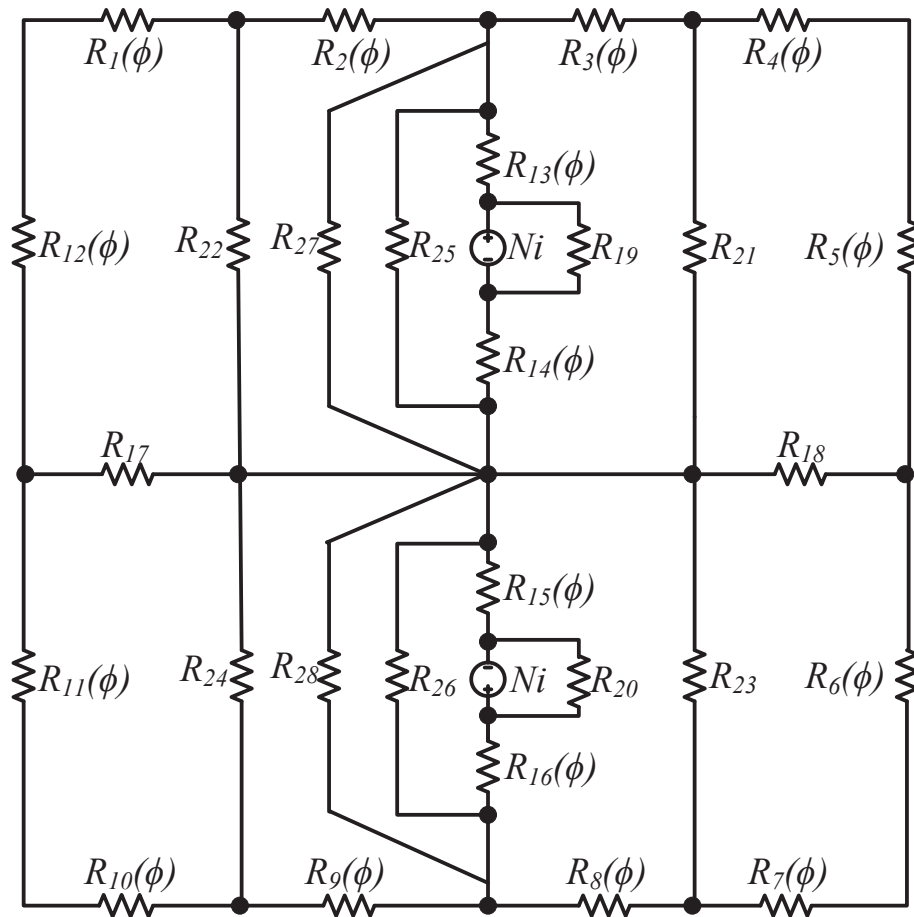
Figure 7.5: Magnetic equivalent circuit

the magnetic material itself, the hysteresis effect can be ignored.

The two winding coils wound around the central leg of the reactor with N number of turns and i Amperes of current, constitute the two MMF sources: $F_1 = F_2 = Ni$.

Core-Piece Reluctances

The reluctances for each core piece can be calculated using (3.11). Due to the symmetrical nature of the circuit, expressions for only one of the equal reluctances are given below:

$$R_1(\phi) = \frac{w_o + 2w_s - 2w_h}{2l_c d_b \mu_B(\frac{\phi}{l_c d_b})} \tag{7.1a}$$

$$R_2(\phi) = \frac{2w_h + w_c}{2l_c d_b \mu_B(\frac{\phi}{l_c d_b})} \tag{7.1b}$$

$$R_5(\phi) = \frac{d_b + d_s}{2l_c w_o \mu_B(\frac{\phi}{l_c w_o})} \tag{7.1c}$$

$$R_{13}(\phi) = \frac{d_b + d_s - 2d_w - DBW}{2l_c w_c \mu_B(\frac{\phi}{l_c w_c})} \tag{7.1d}$$

$$R_{14}(\phi) = \frac{d_w + DBW}{2l_c w_c \mu_B(\frac{\phi}{l_c w_c})} \tag{7.1e}$$

In each expression above, ϕ represents the flux through the corresponding branch, and w_h is the width from the inner end of the window which divides the outer vertical slot leakage flux into two parts (right and left of this width):

$$w_h = w_w + \frac{\frac{d_s}{2}(w_s + w_w) + 2w_s w_w}{d_s + w_s + w_w} \tag{7.2}$$

In the MEC presented in Figure 7.5, $R_1(\phi) = R_4(\phi) = R_7(\phi) = R_{10}(\phi)$, $R_2(\phi) = R_3(\phi) = R_8(\phi) = R_9(\phi)$, $R_5(\phi) = R_6(\phi) = R_{11}(\phi) = R_{12}(\phi)$, $R_{13}(\phi) = R_{15}(\phi)$ and $R_{14}(\phi) = R_{16}(\phi)$.

Leakage Reluctance Calculation

In the GFCR, the opposing MMF sources force the flux to flow outside the main magnetic circuit and close through the window spaces. There are also fluxes that leak from top and bottom yoke, and front and back of the reactor. They all contribute to the flux linkage in the coils [68]. The leakage fluxes can significantly alter the circuit and without taking into account these 'leaks' an
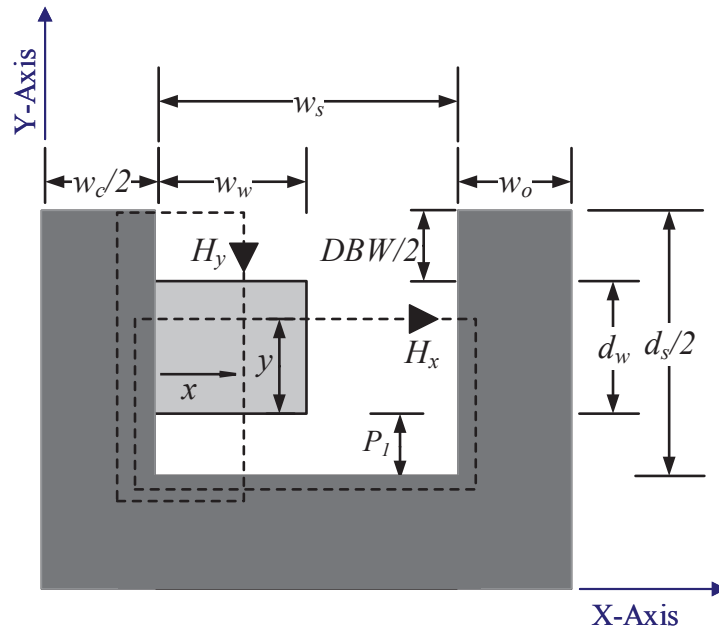
Figure 7.6: 2-D slot flux leakage

accurate MEC cannot be obtained. The coil position with respect to the core window, and winding configuration of the coils also play an important role in accurately predicting the leakage fluxes within the magnetic circuit [46].

2-D Slot Leakage Reluctance

The slot leakage is one of the major contributors of the leakage flux [43]. 2-D slot leakage is the flux leaked within the device window. This flux leakage is the combination of the horizontal and vertical field components labeled as H_x and H_y, respectively, as shown in the bottom $1/4^{th}$ portion of the reactor in Fig. 7.6. Applying Ampere's law to the indicated vertical flux path in the same figure:

$$H_y(d_s/2 + x) = \begin{cases} Ni\frac{x}{w_w}, & 0 \le x \le w_w \\ Ni, & w_w \le x \le w_s \end{cases} \tag{7.3}$$

The ratio in the right-hand side of (7.3) represents the fraction of the winding enclosed by the flux path. Solving (7.3) for field intensity and substituting in (3.15) with $dV = \frac{d_s}{2}l_c dx$, we get:

$$E = \begin{cases} \frac{1}{2}\mu_0 \int_0^{w_w} \left\{ \frac{Nix}{w_w(\frac{d_s}{2}+x)} \right\}^2 \frac{d_s}{2}l_c dx, & 0 \le x \le w_w \\ \frac{1}{2}\mu_0 \int_{w_w}^{w_s} \left\{ \frac{Ni}{(\frac{d_s}{2}+x)} \right\}^2 \frac{d_s}{2}l_c dx, & w_w \le x \le w_s \end{cases} \tag{7.4}$$

Using the energy equivalence,

$$P_{vsl} = \begin{cases} \frac{\mu_0 l_c d_s}{2w_w{}^2}\left[w_w + d_s log(\frac{d_s/2}{d_s/2+w_w}) - \frac{(d_s/2)^2}{d_s/2+w_w} + d_s/2\right], \\ \qquad\qquad\qquad\qquad 0 \le x \le w_w \\ \frac{\mu_0 l_c d_s}{2}\frac{(w_s-w_w)}{(w_s+d_s/2)(w_w+d_s/2)}, & w_w \le x \le w_s \end{cases} \tag{7.5}$$

In a similar way, applying Ampere's law along the horizontal path:

$$H_x w_s = Ni\frac{y}{d_w}, \qquad 0 \le y \le d_w \tag{7.6}$$

121

Here, because of the absence of MMF source between the coil winding and the yoke (represented by the height, $P_1 = (\frac{d_s}{2} - d_w - \frac{DBW}{2})$), there is no permeance component for space below the coil as shown in Figure 7.6. Following the similar procedure with $dV = w_s l_c dy$, energy equivalence yields:

$$P_{hsl} = \frac{\mu_0 l_c d_w}{3 w_s}, \qquad 0 \le y \le d_w \qquad (7.7)$$

3-D Slot Leakage Reluctance

The permeance described by (7.5) and (7.7) only considers the flux traveling straight across the window gap. But the leakage flux also flows over the front and back faces as well. Therefore, addition of some permeance components (3-D slot leakage permeances) to the 2-D slot leakage permeances results in a more accurate representation of the total slot leakage permeance. Figure 7.7 describes the 3-D vertical field path for the lower half of the GFCR. Applying Ampere's law to that 3-D vertical field path:

$$H_{yf}(d_s/2 + \pi r) = \begin{cases} Ni\frac{x}{w_w}, & 0 \le x \le w_w \\ Ni, & w_w \le x \le w_s \end{cases} \qquad (7.8)$$

with $dV = l_r dx dr$, where l_r is the length of leakage flux path: $l_r = d_s/2 + \pi r$, and r is the radius of curvature, the energy balance gives the 3-D vertical slot leakage permeance:
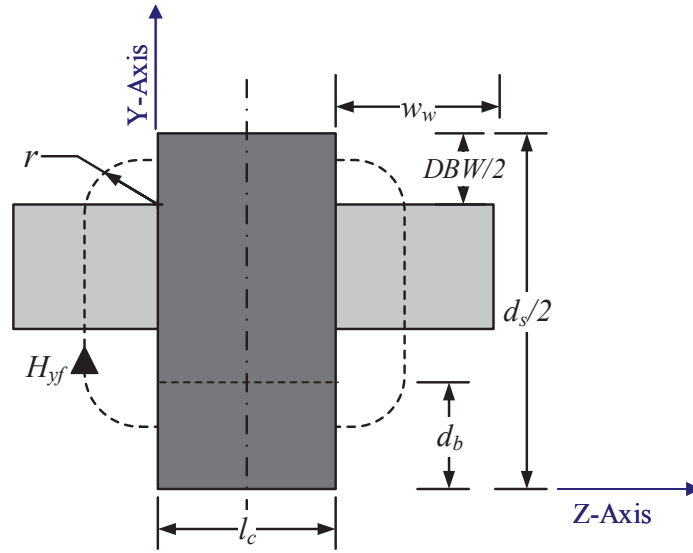
Figure 7.7: 3-D leakage fluxes

$$P_{vslf} = \begin{cases} \frac{\mu_0 w_w}{3\pi} log\left(\frac{d_s/2 + \pi d_b}{d_s/2}\right), & 0 \leq x \leq w_w \\ \frac{\mu_0 (w_s - w_w)}{\pi} log\left(\frac{d_s/2 + \pi d_b}{d_s/2}\right). & w_w \leq x \leq w_s \end{cases} \tag{7.9}$$

Similarly, the Ampere's law for 3-D horizontal slot leakage flux path:

$$H_{xf}(w_s + \pi r) = Ni\frac{y}{d_w}, \qquad 0 \leq y \leq d_w \tag{7.10}$$

With $dV = (w_s + \pi r)drdy$, gives 3-D horizontal slot leakage permeance:

$$P_{hslf} = \frac{\mu_0 d_w}{3\pi} log(\frac{w_s + \pi r_{mx}}{w_s}), \qquad 0 \leq y \leq d_w \tag{7.11}$$

where, $r_{mx} = min(w_c/2, w_o)$ is an approximate curvature of three-dimensional horizontal slot flux linkage.

The total horizontal leakage permeance for the region $0 \leq y \leq d_w$ corresponds to $P_{19} = P_{20}$ in the MEC model:

$$\begin{aligned} P_{19} = P_{20} &= 2(P_{hsl}|_{0 \leq y \leq d_w} + 2P_{hslf}|_{0 \leq y \leq d_w}) \\ &= 2 \left[\frac{\mu_0 l_c d_w}{3 w_s} + \frac{2\mu_0 d_w}{3\pi} log(\frac{w_s + \pi r_{mx}}{w_s}) \right] \end{aligned} \tag{7.12}$$

The total vertical leakage permeance for the region $0 \leq x \leq w_w$ corresponds to $P_{25} = P_{26}$ in the MEC model:

$$P_{25} = P_{26} = 2(P_{vsl}|_{0 \leq x \leq w_w} + 2P_{vslf}|_{0 \leq x \leq w_w})$$

$$= \frac{\mu_0 l_c d_s}{w_w{}^2} \left\{ w_w + d_s log \left(\frac{d_s}{d_s + 2w_w} \right) - \frac{d_s^2}{2d_s + 4w_w} + \frac{d_s}{2} \right\} + \frac{4\mu_0 w_w}{3\pi} log \left(\frac{d_s + 2\pi d_b}{d_s} \right) \tag{7.13}$$

The single reluctance representation of R_{19}, R_{20}, R_{25} and R_{26} in the MEC model are achieved by doubling the permeances in (7.12) and (7.13). In a similar way, for the region $w_w \leq x \leq w_s$, the total vertical slot permeances $P_{21} = P_{22} = P_{23} = P_{24}$ in the MEC model are:

$$P_{21} = P_{22} = P_{23} = P_{24} = P_{vsl}|_{w_w \leq x \leq w_s} + 2P_{vslf}|_{w_w \leq x \leq w_s}$$
$$= \frac{2\mu_0 l_c d_s (w_s - w_w)}{(2w_s + d_s)(2w_w + d_s)} + \frac{2\mu_0 (w_s - w_w)}{\pi} log \left(\frac{d_s + 2\pi d_b}{d_s} \right) \tag{7.14}$$

Exterior Adjacent Leakage Reluctance

This is a leakage reluctance due to the flux associated with the bundle of conductors adjacent to the core on the front and back of the central leg as shown in Figure 7.8. The figure shows the side view of only one symmetrical half of the central core winding with two possible paths for the flux flow. The flux path (interior or exterior) is based on the width of the winding, w_w, relative to the end widths, w_{e1} and w_{e2}.

Applying Ampere's law for the paths shown:

$$Hl_p = \begin{cases} Ni\frac{r}{w_w}, & 0 \leq r \leq r_1 \\ Ni, & r_1 \leq r \leq r_2 \end{cases} \tag{7.15}$$

where, $l_p = (d_w + \pi r)$, $r_1 = min(w_{e1}, w_{e2}, w_w)$ and, $r_2 = min(w_{e1}, w_{e2})$.

The external adjacent leakage reluctance should also include the part of the flux that flows from the top of the yoke as well. To take this flux into account, half of the depth of the yoke ($l_c/2$) has been

125
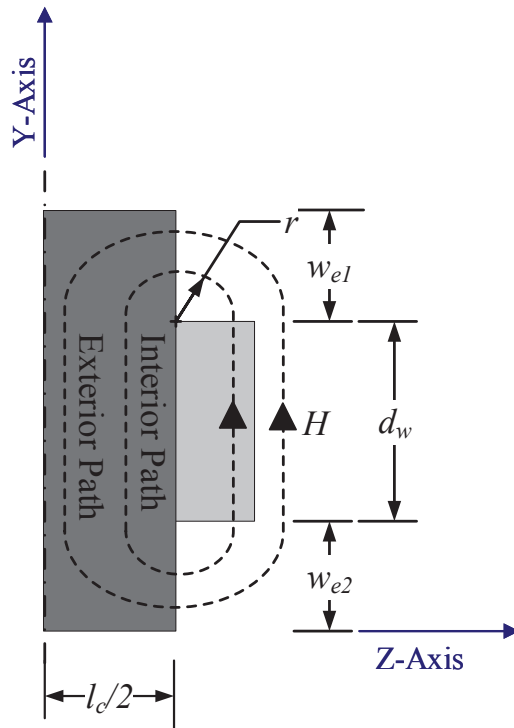
Figure 7.8: Exterior adjacent leakage flux

added to the top end width, w_{e1}. A special attention should be given while defining the differential volume for integration, $dV = l_p l_e dr$; the effective depth (l_e) of the external adjacent leakage flux path in the figure is not the same as the depth of core into the page (l_c), but:

$$l_e = w_c + 2w_w \tag{7.16}$$

The external adjacent leakage permeance is found to be:

$$P_{eal} = \frac{\mu_0 l_e}{\pi w_w^2} \left[\frac{r_1^2}{2} - \frac{d_w r_1}{\pi} + \frac{d_w^2}{\pi^2} \log \left(\frac{d_w + \pi r_1}{d_w} \right) + w_w^2 \log \left(\frac{d_w + \pi r_2}{d_w + \pi r_1} \right) \right] \qquad (7.17)$$

In the MEC, $P_{27} = P_{28} = 2P_{eal}$ to accommodate permeance on both of the faces.

Air Gap Reluctance

The GFCR makes the use of the window air space. Therefore, it is important to include the reluctance associated with this air gap, which is not included in the slot leakage calculation. A lumped reluctance of the space between the coils within and outside the window is considered in the model. The reluctance of the air-gap inside the window space according to (3.4) is:

$$R_{airin} = \frac{w_s}{\mu_0 l_c DBW} \qquad (7.18)$$

The leakage flux from the front and the back of the air-gap is represented by the approximate reluctance of:

$$R_{airout} = \frac{1}{2} \frac{(w_s + r_{mx})}{\mu_0 r_{mx} DBW} \qquad (7.19)$$

where, $r_{mx} = min(w_c/2, w_o)$ is an approximate curvature of R_{airout} flux linkage. The parallel combination of R_{airin} and $2R_{airout}$ gives the total air-gap reluctance for a window. This total

127

air-gap reluctance corresponds to R_{17} and R_{18} in the MEC model.

Equivalent Inductance

The GFCR can be represented by a passive electric circuit element, an inductor, facilitating the translation from the magnetic circuit into an electric circuit.

Being a multiple winding system device, the inductance of the GFCR can also be found using the self and the mutual inductances of each coil when the system is linear, i.e. unsaturated. If L_{11} and L_{22} are the self-inductance of each coil and $M(= L_{12} = L_{21})$ is the mutual inductance between them, the equivalent inductance of the reactor will be:

$$L = L_{11} + L_{22} - 2M \tag{7.20}$$

Since the two coils are assumed to be identical and placed symmetrically around the horizontal mid-plane of the core, the equivalent inductance becomes:

$$L = 2(L_{11} - M) \tag{7.21}$$

The self and mutual inductance calculation of the GFCR can be found from the MEC by considering only one excitation coil at a time, and finding the flux linkages in both coils. From the relationship between flux linkages and currents,

$$\begin{bmatrix} \lambda_1 \\ \lambda_2 \end{bmatrix} = \begin{bmatrix} L_{11} & L_{12} \\ L_{21} & L_{22} \end{bmatrix} \begin{bmatrix} I_1 \\ I_2 \end{bmatrix} \tag{7.22}$$

If only I_1 is applied then the self and mutual inductance are calculated by

$$\begin{bmatrix} L_{11} \\ L_{21} \end{bmatrix} = \frac{1}{I_1} \begin{bmatrix} \lambda_1 \\ \lambda_2 \end{bmatrix} = \frac{N}{I_1} \begin{bmatrix} \Phi_1 \\ \Phi_2 \end{bmatrix} \tag{7.23}$$

where, Φ_1 and Φ_2 are fluxes through coils 1 and 2, respectively. In a similar way, the self and mutual inductance can be calculated with coil 2 excited alone and then superposition can be applied between the inductance values using (7.20) to get the total inductance of the reactor. Special attention should be paid while performing this calculation not to saturate the core. This is because with only one coil excited and no gaps within the core, even a small amount of excitation in one winding can saturate the ferromagnetic core and the reactor operation will fall into the nonlinear region.

For the MEC shown in Figure 7.5, the symmetry of the system can be taken advantage off to obtain the simplified circuit relatively easily. Figure 7.9 shows the process of arriving at the Thevenin equivalent by first folding the circuit along the horizontal and vertical axes of symmetry, and representing the parallel branches with their equivalents. In Figure 7.9a, $R_X = 0.5(R_{25}||R_{27})$. Then, the circuit is reduced to a single reluctance by sequentially consolidating the branches in series and parallel.
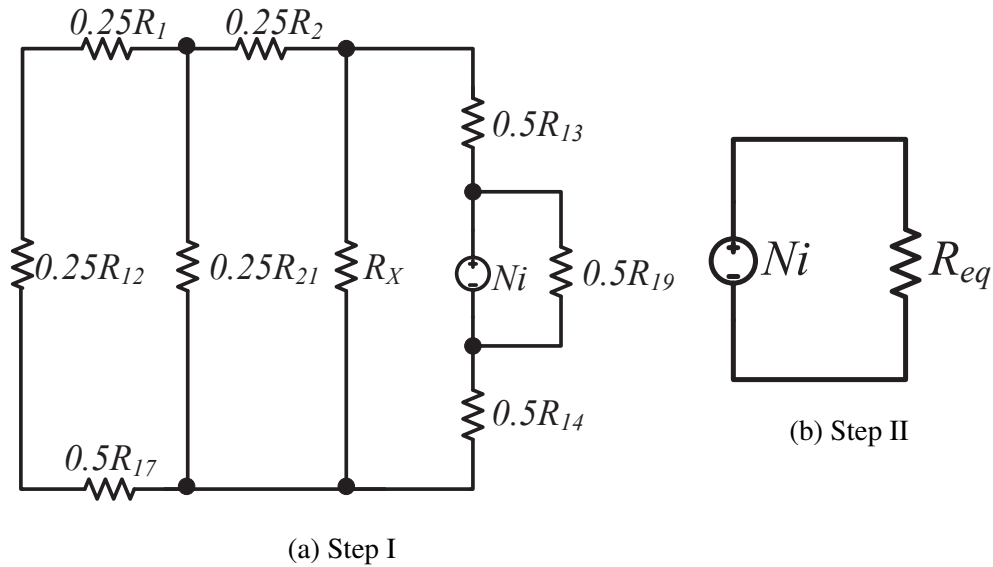
Figure 7.9: MEC circuit reduction

MEC Validation

For validation of the proposed MEC model, a GFCR is considered with parameters as shown in Table 7.1. The magnetic core material is chosen to be Si-Fe M36. The properties of the material along with the $\mu_B()$ characterization function parameters are taken from [44] and presented in Table 7.2. The relative error between the inductance values obtained using MEC and a 3-D FEA serves as a criterion for the validity of the model. For simplicity, the reactor is excited by a current that does not cause saturation of its core.

Magnetic Equivalent Circuit Approach

The anhysteretic B-H characteristics curve for Si-Fe M36 is described by (3.9) and shown in Figure 4.6 with the help of $\mu_B()$ parameters from Table 7.2.

Table 7.1: GFCR parameters

Parameters	Symbol	Value
Height of slot	$d_s(mm)$	660.4
Width of Slots	$w_s(mm)$	152.4
Width of outer leg	$w_o(mm)$	90
Width of central leg	$w_c(mm)$	180
Height of yoke and base	$d_b(mm)$	90
Depth of Core	$l_c(mm)$	90
Height of winding bundle	$d_w(mm)$	190.5
Width of windings	$w_w(mm)$	15.15
Number of turns in each winding	N	50
Current through each winding	$i(A)$	100
Distance between the windings	$DBW\ (mm)$	140

A = Ampere, mm = milimeter.

Table 7.2: Silicon steel M36 properties

Density $\rho(Kg/m^3)$	Max Flux $B_{max}(T)$	μ_r	$\mu_B()$ Data		
			α_k	β_k	γ_k
7018	1.34	26673	0.226	271.844	1.351
			0.0432	97.3174	10.0
			0.0311	42.2946	1.3241
			0.00437	0.80580	5.3817

T=Tesla

For the *DBW* shown in Table 7.1, the equivalent inductance of the reactor is calculated by solving the MEC and using (3.22)-(3.24), and checked again with (7.21).

Finite Element Analysis (FEA) Approach

Based on the geometrical description given in Table 7.1, a 3-D FEA model for the GFCR was created using ANSYS Maxwell, an electromagnetic field simulation software based on FEA. This model is shown in Figure 7.10. In the figure, the flux flow in the core is indicated by vector arrows
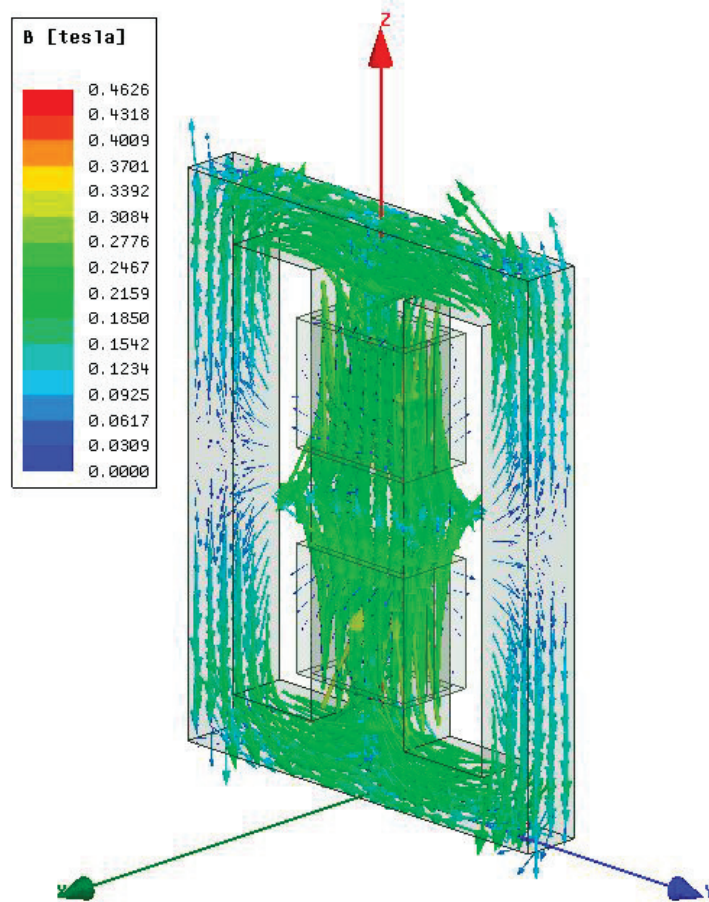
Figure 7.10: FEA model of GFC reactor

and flux densities within the core are represented by the color index. It can be seen that the reactor operates in the linear region of the B-H curve of Figure 4.6.

The results from calculations using both methods on the same computer are summarized in Table 7.3.

Comparing the values, the relative error between the calculated inductances is 3.62%. The computation time for the FEA approach is about 3000 times slower than the MEC approach.

The comparison of inductances is also performed for symmetrical variation of all possible winding

Table 7.3: Summary results from MEC and FEA

Approach	MEC	FEA
Computation time (s)	0.027	81
Inductance (mH)	3.72	3.86
Number of iterations	4	17

mH = mili-Henry, s = second
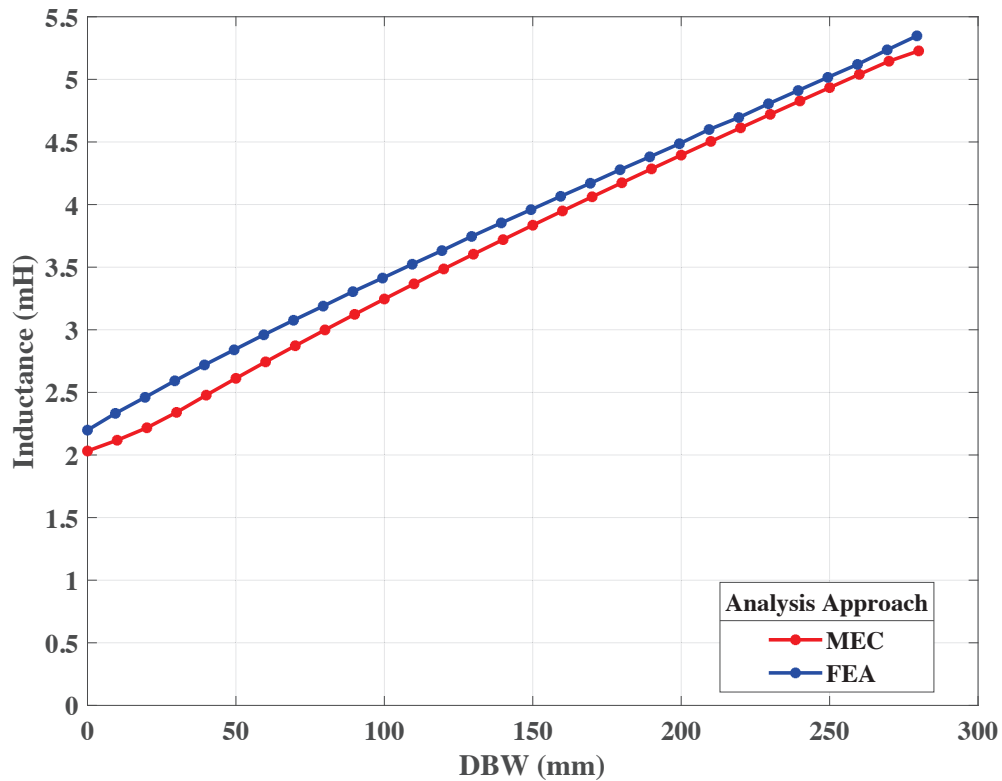
Figure 7.11: Inductance vs *DBW*

coil positions using both approaches. The results of inductance values for this whole range of *DBW* variation are shown in Figure 7.11.

From the figure, it can be seen that the inductance is highest when the two windings are farthest apart and lowest when the windings are next to each other. The range of errors between the values

is between 1.75% and 10.15% with the root mean square error (RMSE) of 0.1628 mH throughout the variation. As in the base case, the computation time of the FEA is much higher than that of MEC for the complete sweep of *DBW*. The deviation of inductance values is high for lower separation between the coils. The error between these approaches is due to the limited ability of MEC to represent all the leakages within and outside of the reactor in all directions.

An approximate analytical expression for inductance of the GFCR can be derived as a function of *DBW* using (3.25) with help from some symbolic computation software. Wolfram MATHEMAT-ICA was used for this purpose with the following result:

$$L = 5.676 - \frac{1.64 \times 10^7 + 38289.1DBW}{2.88 \times 10^6 + 11009.1DBW + (428 + DBW)log(0.8 + 6.6DBW)} \quad (7.24)$$

The inductance variations obtained from using MEC model and (7.24) are shown in Figure 7.12. The plot proves the validity of the approximate expression derived for the whole range within a very small tolerance. In a real device, the distance between the coils can be decreased to the point where the two coils are next to each other. The approximate expression allows us to virtually decrease the distance further in the negative direction and these inductance values are plotted in Fig. 7.13. It can be seen that the inductance value drops down to zero at *DBW* = -91mm. This value is very close to one-half of the height of each coil $(d_w/2)$ which is 95.25mm. Theoretically, when the two opposing coils completely overlap, the total MMF of the system becomes zero as well as its equivalent inductance. This result is a further proof of the expression derived in (7.24), which can be used to quickly assess the characteristic parameter for a specific inductance required.

134
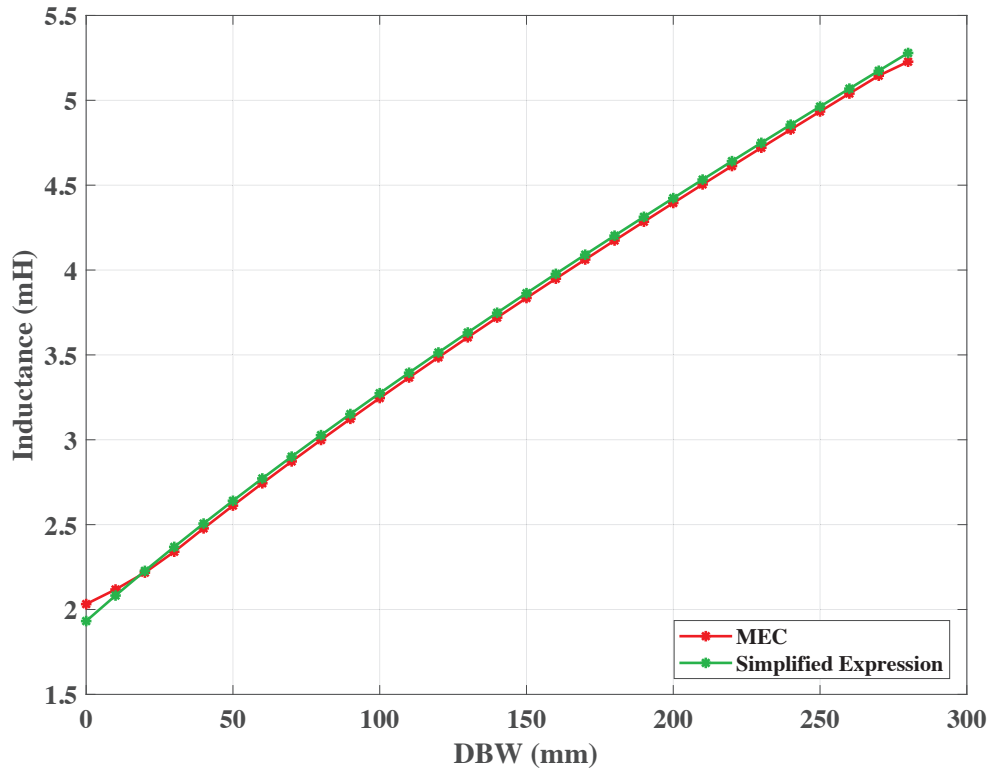
Figure 7.12: Inductance from simplified expression

Ferromagnetic Core Volume Comparison

A volumetric comparison is carried out between a GFCR and a conventional gapped ferromagnetic core reactor. The intention is to provide an insight into the bulkiness of the GFCR and, hopefully, help in making the decision which reactor is more appropriate for a specific application. Only the volume of the ferromagnetic core material is compared, considering it to be the driving factor for the size difference between the two reactor types. The core volume is given by:

$$Vol_{GFCR} = d_s w_c l_c + 2 w_o d_s l_c + 2(2w_s + 2w_o + w_c) d_b l_c \qquad (7.25)$$

135
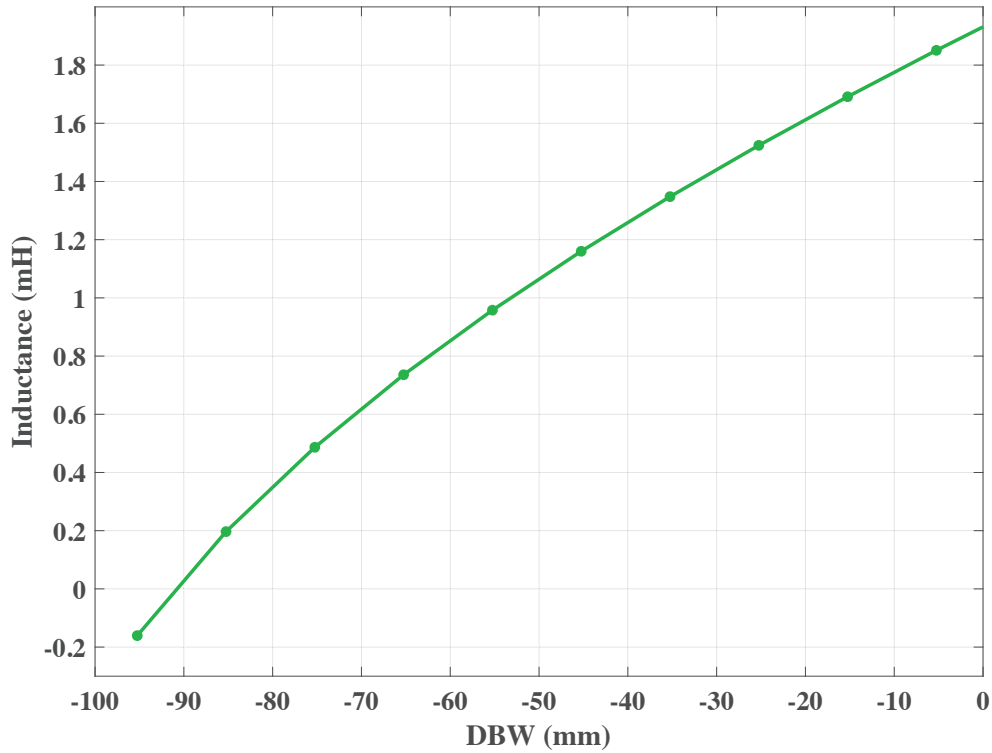
Figure 7.13: Zero induction point verification

For the dimensions of the GFCR shown in Table 7.1, the ferromagnetic volume according to (7.25) is found to be 1962.93 in^3. For a specific winding configuration with $DBW = 210$ mm from Figure 7.11, the inductance of the device is found to be $L_{FEA} = 4.6\ mH$ and $L_{MEC} = 4.5\ mH$, from the FEA and the MEC analysis, respectively. A single-phase gapped ferromagnetic core reactor can be designed with a gap (g) of 0.6327 in in the central core of the reactor. The main electromagnetic parameters and the core material specifications are kept the same for both reactors. An optimization design procedure to minimize the ferromagnetic volume described in [9] has been applied, and the volume of the gapped reactor is found to be 1947.045 in^3.

From the above example, it can be observed that the core volumes of both reactors are nearly the same while producing identical inductances. This implies that in terms of the required tank

136

volumes, they are also going to be the same. This example confirms that it is possible to design a GFCR under the same volume constraints as the conventional gapped reactor.

Conclusion

A generic magnetic equivalent circuit of a GFCR has been developed and validated for the whole range of variation of its characteristic parameter, distance between the two coils of the winding. The MEC takes into account all major three-dimensional flux flows when calculating the reluctances. The model is verified by comparing the results for the equivalent inductance with those obtained using 3-D FEA. The comparison shows that the error is small over the whole range of variation, confirming the accuracy of the MEC model. Based on the developed model, an approximate inductance expression has been derived in terms of the characteristic parameter. The approximation has proved surprisingly good.

CHAPTER 8: OPTIMAL POWER FLOW IN POWER SYSTEMS WITH VARIABLE SERIES IMPEDANCES

Nomenclature

Parameters

α	Percentage change in reactance of a transmission line
θ_n^{max}	Maximum voltage angle for bus m
θ_n^{min}	Minimum voltage angle for bus n
$B0_k$	Constant susceptance branch connected to line k
B_k'	Changed susceptance of transmission line k
B_k^{max}	Maximum susceptance limit of transmission line k
B_k^{min}	Minimum susceptance limit of transmission line k
$B_{k,i}$	Parallel susceptance branches of susceptance bank connected to line k, $i \in NBits$
$B_{k,low}$	Lowest susceptance branch of susceptance bank connected to line k
B_k	Original susceptance of transmission line k
c_g	Operational cost associated with generator g (\$/MWh)
d_n	Load at bus n
F_k^{max}	Maximum power flow capacity of transmission line k
N_l	Number of transmission branches after problem reformulation
n_l	Number of original transmission branches
N_{VSR}	Total number of VSR devices available
$Nbits$	Number of parallel susceptance branches connected in series with each transmission line
P_g^{max}	Maximum active power generation capacity of generator g
P_g^{min}	Minimum active power generation capacity of generator g
X_k'	Changed reactance of transmission line k
X_k	Original reactance of transmission line k

Sets

$\sigma^+(n)$	Set of lines specified to as to node n
$\sigma^-(n)$	Set of lines specified to as from node n
G	Set of generators
$g(n)$	Set of generator connected to node n
K	Set of all transmission elements, lines or transformer
$NBits$	Set of parallel suceptance branches of a susceptance bank

Indices

g	Index of generators, $g \in G$
i	Index of parallel susceptances
k	Index of transmission elements, $k \in K$
m, n	Index of buses

Variables

θ_n	Voltage angle of bus n
B'_k	Variable susceptance of transmission line k
F_k	Real power flow in transmission line k
P_g	Real power output of generator g
x_k	Binary variable in VSR allocation problem indicating whether branch k is equipped with VSR device or not
$y_{k,i}$	Binary variables representing switchable susceptance branch i state for lines k equipped with VSR devices
z_k	Binary variable indicating the sign of voltage angle difference on line k after initial DC OPF without VSR

Introduction

Despite the recent changes in power systems (structure, market, uncertainty, technological advancements), their ultimate goals remain the same, which is a safe, economical, efficient, secure, and reliable supply of electric energy [69]. Over the last decades, electricity consumption and generation have continually grown, but investments in T&D infrastructure have steadily declined. The combined effect is that the power system has become increasingly complex to operate and less secure. Furthermore, the existing power system is increasingly strained with extended operating limits causing the increased probability of instabilities [70]; and transmission bottlenecks are one of the sources of system inefficiency. This demands better power flow control or transmission infrastructure upgrades. Utilization improvement of the existing transmission infrastructure is a faster and cheaper alternative than developing new transmission lines to relieve the stress on the aging infrastructure in today's competitive environment. Optimal utilization of the existing resources also defers the necessary investment in new infrastructure to the future [71].

Numerous initiatives have been carried out to enhance hardware utilization capable of improving power flow control, including methods like transmission switching (TS) [72], [73], phase shifting, and adjusting line parameters. TS can reduce operating costs, improve reliability, and improve the management of intermittent sources; however, it is challenged by computational complexity, solution infeasibility, and instability issues. The continuous adjustment of the line's reactance aims at the same goal with less concern for power system stability. To achieve this goal, different solutions have been put forward. They include: dry-type air-core reactors [74]; Flexible AC transmission System devices (FACTS) [75], [76]; distributed FACTS (DFACTS) [77], [78]; and, recently, Magnetic Amplifier-based Power Flow Controller (MAPFC) [79], also dubbed Continuously Variable Series Reactor (CVSR). The dry-type air-core series reactor is the simplest of all devices since it only has two states, completely on or off. This characteristic results in a lack of flexibility as different load distribution profiles would require different size reactors. Compared to the constant series reactor, FACTS can offer better control and flexibility. However, the converter complexity and semiconductor ratings significantly increase the cost of the FACTS device. Moreover, FACTS devices have lower reliability as a single component failure can prove fatal in the overall device performance. To overcome the disadvantages of the FACTS devices, distributed FACTS or DFACTS have been proposed [25]. They are comprised of a series of independent devices directly attached to the power conductor that use the transformation effect to inject small voltages into the conductor. A meaningful change of line impedance can be achieved by the overall effect of a number of these devices. One drawback of DFACTS is that they require complex communication and coordination. MAPFC utilizes both magnetic and power electronic components that are galvanically separated, with the goal of using the best of both worlds: robustness, reliability, efficiency, and low cost of high-power, traditional electromagnetic technology with the flexibility, speed, and size of power electronic-based control. Some more detailed models of this type of device have been recently proposed in [8], [29].

All of the above technologies share one common characteristic. Effectively, they all change the series impedance of the power line. In this chapter, the term "CVSR" is used loosely to indicate devices capable of significantly affecting the line's reactance. The reactance change makes the variable CVSR allocation problem a mixed-integer non-linear program (MINLP) even though it is incorporated within a DCOPF. The combinatorial form is due to binary variables used to find optimal locations of CVSR, while non-linearity comes from a product of a bus angle (variable) and a susceptance (variable). This MINLP form of the problem is an NP-hard problem which is challenging to solve [80]. Under a strong assumption that installation of a CVSR does not change the direction of power flows, authors in [71] reformulated the MINLP form of the CVSR allocation problem into a computationally efficient two-stage mixed-integer linear program (MILP). In the first stage, DCOPF is solved to find the direction of power flows. In the second stage, the MILP form of the CVSR allocation problem is put forward by fixing the direction of power flows on transmission lines to which series reactors are to be connected. Another approach also divides the problem into two stages. The first stage is a power flow control subproblem used to determine the new control variables, i.e., the susceptances of the lines with controllers. The second stage is the solution of the OPF using Sequential Quadratic Programming with successive linearization of the constraints [81].

In this chapter, we propose a new bitwise MILP formulation of the CVSR allocation problem. Unlike the formulation in [71], we have relaxed the assumption that a CVSR installation does not change the direction of power flows. This reformulation is free of any such assumptions and CVSRs are modeled to change susceptance in discrete steps using binary coding. The variable susceptances in the system are modeled as n parallel branches with an adequately selected ΔB such that each additional branch has twice the value of ΔB from the previous one. This way, with n binary switches, there are 2^n levels of values from the total branch susceptance B, which gives enough resolution in the selection of the optimal control variable. The selection of the discrete

susceptances is made by using binary variables. The approach is demonstrated on a modified version of a widely used power system test case: the IEEE 118-bus system. Simulation results are compared with the results reported in the literature to prove the robustness and effectiveness of the proposed approach. For the comparison, a two-stage LP-based formulation [71] is used and implemented.

The main contribution of this chapter is the novel bitwise MILP reformulation of the original MINLP CVSR allocation problem, along with some comparative analyses performed against the two-stage LP-based formulation for the modified IEEE 118-bus system. This chapter is organized as follows: the second section gives the background information regarding DCOPF with refined formulation and explanation of the two-stage LP approach with its drawbacks; the following section introduces the bitwise MILP based reformulation for the CVSR allocation problem; the next section provides the numerical case studies with comparative analyses; and the last section concludes the chapter with future directions regarding the scalability of the formulation, AC feasibility, system stability, and reliability.

Mixed Integer Linear Formulation

Optimal power flow (OPF) is an essential part of the electricity market and, in its original form, is a nonlinear and non-convex problem. Therefore, a variety of approximate OPF formulations have been introduced to get a close to optimal solution in a limited time. Among the approximations, DCOPF is the simplest and most widely used in power system operation because of its computational simplicity and convexity [82]. The formulation proposed in this chapter is based on the standard DC OPF formulation. Therefore, we first give the basic formulation of a DCOPF problem for a comprehensive presentation.

The DCOPF can be formulated as follows:

$$\min \sum_g c_g P_g \qquad\qquad (8.1\text{a})$$

$$\theta_n^{min} \leq \theta_n \leq \theta_n^{max} \qquad\qquad \forall n \qquad\qquad (8.1\text{b})$$

$$P_g^{min} \leq P_g \leq P_g^{max} \qquad\qquad \forall g \qquad\qquad (8.1\text{c})$$

$$-F_k^{max} \leq F_k \leq F_k^{max} \qquad\qquad \forall k \qquad\qquad (8.1\text{d})$$

$$F_k - B_k(\theta_n - \theta_m) = 0 \qquad\qquad \forall k \qquad\qquad (8.1\text{e})$$

$$\sum_{k \in \sigma^+(n)} F_k - \sum_{k \in \sigma^-(n)} F_k + \sum_{g \in g(n)} P_g = d_n \qquad \forall n. \qquad (8.1\text{f})$$

Active power generation cost minimization is the standard objective of OPF. A linear function for the cost is considered with a cost coefficient of $c_g(\$/MWh)$. Voltage angle limits are imposed by (8.1b)[1] for each bus. Constraint (8.1c) represents the active power generation limit for all generators, while (8.1d) indicates the active power flow limit through each branch. The linearized power flow equation is enforced by (8.1e), and (8.1f) represents the power balance at each bus. The latter states that the sum of all generation at a bus and total power flow to that bus is equivalent to the sum of power demand at the bus and the total power flow out of it.

In (8.1e), because of the presence of CVSR devices, B_k is no longer a parameter but a variable. The multiplication of two variables renders the DCOPF to be a nonlinear program (NLP) problem.

---

[1]Maximum and minimum voltage angle limits were set to be 0.6 and -0.6 radians respectively

For the optimal allocation of VSRs, the following $if - else$ statement (8.2) is introduced, which replaces the line flow constraint (8.1e):

if VSR installed:

$$F_k - B'_k(\theta_n - \theta_m) = 0 \qquad \forall k \qquad (8.2a)$$

$$B_k^{min} \leq B'_k \leq B_k^{max} \qquad \forall k \qquad (8.2b)$$

$else$:

$$F_k - B_k(\theta_n - \theta_m) = 0 \qquad \forall k \qquad (8.2c)$$

Since modeling of the $if - else$ statement requires introduction of binary variables, the NLP form of the VSR allocation problem is transformed into an MINLP form, which is a computationally intractable problem.

Refined Two-stage MILP formulation

Among the methods to solve the MINLP, [71] introduces a mixed-integer linear program (MILP) conversion of the MINLP as a two-stage linear problem. A characteristic of this approach is the sign enforcement of the voltage angle difference for the lines equipped with CVSRs.

First, the DCOPF, as defined in (8.1a)-(8.1f), is solved without CVSRs, and the phase angle difference is calculated for each line. Based on the sign of the phase angle difference, a binary variable assignment is done to each line according to (8.3).

$$z_k = \begin{cases} 1, & \text{if } \theta_m \geq \theta_n \\ 0, & \text{if } \theta_m \leq \theta_n \end{cases} \tag{8.3}$$

After that, a MILP CVSR allocation formulation is presented and applied with z_k enforced as parameters. A refined Big-M formulation for this approach can be given as follows:

$$\min \sum_g c_g P_g \tag{8.4a}$$

$$\theta_n^{min} \leq \theta_n \leq \theta_n^{max} \qquad \forall n \tag{8.4b}$$

$$P_g^{min} \leq P_g \leq P_g^{max} \qquad \forall g \tag{8.4c}$$

$$-F_k^{max} \leq F_k \leq F_k^{max} \qquad \forall k \tag{8.4d}$$

$$\sum_{k \in \sigma^+(n)} F_k - \sum_{k \in \sigma^-(n)} F_k + \sum_{g \in g(n)} P_g = d_n \qquad \forall n \tag{8.4e}$$

$$(1 - x_k)(F_k - B_k(\theta_n - \theta_m)) = 0 \qquad \forall k \tag{8.4f}$$

$$x_k((1 - z_k)B_k^{min} + z_k B_k^{max})(\theta_n - \theta_m)$$
$$+ M(1 - x_k) \geq F_k \qquad \forall k \tag{8.4g}$$

$$x_k((1 - z_k)B_k^{max} + z_k B_k^{min})(\theta_n - \theta_m)$$
$$- M(1 - x_k) \leq F_k \qquad \forall k \tag{8.4h}$$

$$x_k \{(1 - z_k)\theta_m + z_k\theta_n - (1 - z_k)\theta_n - z_k\theta_m\}$$
$$+ M(1 - x_k) \geq 0 \qquad \forall k \tag{8.4i}$$

$$x_k, z_k \in \{0, 1\} \qquad \forall k \tag{8.4j}$$

$$\sum_k x_k \leq N_{CVSR} \tag{8.4k}$$

$$M >> Max \{F_k + B_k(\theta_m - \theta_n)\}. \tag{8.4l}$$

In (8.4), (8.4f)-(8.4i) represent the line flow constraints with and without CVSR, dictated by binary variables x_k and z_k. The available number of CVSRs is constrained with (8.4k), and the value of big M is chosen according to (8.4l). The refined formulation provided here reduces the constraints,

using only the necessary ones, compared to the original in [71].

Issues with Two-stage MILP formulation

The above approach can produce optimal active power generation cost solution for the CVSR allocation problem, but it is not free from issues. The main drawbacks of this formulation are:

1. Power flow direction enforcement for the lines with CVSRs can cause the solution to be suboptimal. Based on the system size and conditions, a suboptimal power system operation can result in the loss of billions of dollars [83].

2. For the complete optimal allocation solution, two optimization problems, (8.1) & (8.4), need to be solved in sequence, which can make its application cumbersome.

3. The optimal susceptance value of CVSR is obtained by using a continuous variable bound between maximum and minimum limits. In practice, it may be difficult to implement the exact solution to the optimization problem.

The proposed bitwise MILP formulation presented in the sequel can resolve all of these issues.

Bitwise MILP Reformulation

In this approach, the change in branch reactance with the addition of a CVSR to the branch is represented by a parallel-connected susceptance bank in series with the line reactance, as shown in Figure 8.1, where the dashed box represents the CVSR connected in series with line k between bus m and n. Each parallel-connected susceptance can be switched on/off via a binary variable, resulting in an effective variable reactance of the line. The susceptance bank is equivalent to the

147
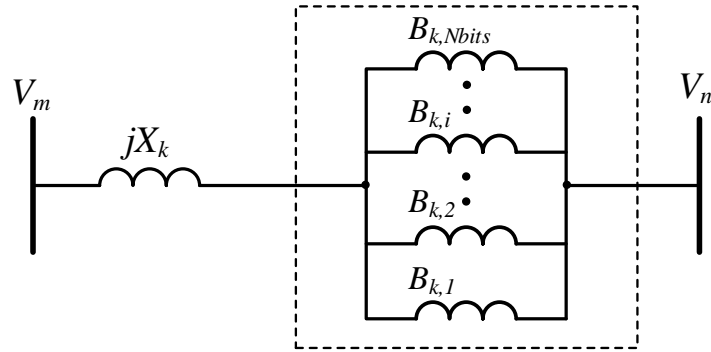
Figure 8.1: Addition of susceptance bank to a line

addition of several switchable short-circuited reactances in series with the transmission line. The use of susceptances is predominant in power flow studies and OPF problems, hence their use in Figure 8.1 and throughout the chapter. The addition of switchable parallel susceptance branches to each branch of the network, with $Nbits$ being the number of such branches, is the prerequisite for this formulation. A characteristic of this arrangement is the binary coding in which each next parallel branch has susceptance that differs from the previous by the factor of 2. The binary control of those branches allows the variable reactance variation in a bitwise fashion. Therefore, switching of $Nbits$ parallel susceptance branches gives 2^{Nbits} options for susceptance selection with MILP. The required susceptance resolution can be achieved with adequately chosen $Nbits$. The susceptance variation offered by the susceptance bank resembles the binary to decimal conversion, where the susceptance branch represents the bit of binary number.

If the reactance of a transmission line k can be changed by $\pm\alpha\%$ by the use of a CVSR, the changed reactance range is given by (8.5).

$$X'_k \in [(1 - \alpha)X_k, (1 + \alpha)X_k] \tag{8.5}$$

Equation (8.6) represents the equivalent new susceptance range.

$$B'_k \in \left[\frac{B_k}{(1 + \alpha)}, \frac{B_k}{(1 - \alpha)} \right] \tag{8.6}$$

Because of the presence of a CVSR, the incremental range of the susceptance of line k from original B_k is:

$$\left[-B_k \frac{\alpha}{(1 + \alpha)}, B_k \frac{\alpha}{(1 - \alpha)} \right] \tag{8.7}$$

Since the susceptance increment limits are not symmetrical to B_k, it can be made symmetrical by choosing either of the limits symmetrically (upper limit gives a better symmetrical range). Therefore, the total possible change in the susceptance is:

$$\Delta B_k = B_k \frac{2\alpha}{(1 - \alpha)} \tag{8.8}$$

The smallest value of the parallel susceptance in the susceptance bank can be found by dividing the total interval change into a number of sub-intervals, as in (8.9).

$$B_{k,low} = \frac{\Delta B_k}{2^{Nbits} - 1} \tag{8.9}$$

The susceptance steps generated by controlling the binary switches are the multiple of this value.

$$B_{k,i} = 2^{(Nbits-i-1)} B_{k,low} \tag{8.10}$$

Furthermore, a careful initial selection of constant susceptance (capacitive) for each branch, (8.11), could make the variation of the line reactance in both directions with binary switches in the parallel susceptance bank and the original line susceptance in the middle of the change.

$$B0_k = B_k - B_{k,low}(2^{Nbits-1} - 1) \tag{8.11}$$

The complete bitwise MILP reformulation is given by (8.12).

$$\min \sum_g c_g P_g \tag{8.12a}$$

$$\theta_n^{min} \leq \theta_n \leq \theta_n^{max} \qquad \forall n \tag{8.12b}$$

$$P_g^{min} \leq P_g \leq P_g^{max} \qquad \forall g \tag{8.12c}$$

$$-F_k^{max} \leq F_k \leq F_k^{max} \qquad \forall k \tag{8.12d}$$

$$\sum_{k \in \sigma^+(n)} F_k - \sum_{k \in \sigma^-(n)} F_k + \sum_{g \in g(n)} P_g = d_n \qquad \forall n \tag{8.12e}$$

$$F_k = (\theta_m - \theta_n) \left[(1 - x_k) B_k + B0_k x_k + \sum_{i=1}^{Nbits} y_{k,i} B_{k,i} \right]$$

$$\forall k \tag{8.12f}$$

$$x_k \geq y_{k,i} \qquad \forall k, \forall i \tag{8.12g}$$

$$x_k, y_{k,i} \in \{0, 1\} \tag{8.12h}$$

$$\sum_k x_k \leq N_{CVSR} \tag{8.12i}$$

Technically, with this formulation, the problem size becomes larger with the number of branches being:

$$N_l = (N_{Bits} + 1) n_l. \tag{8.13}$$

Here, n_l represents the original number of branches. The branch flow limits should be imposed on the combined flow in the original branch and all binary controlled parallel branches connected to it. This flow limit can be achieved by the combination of constraints (8.12d) and (8.12f). The total number of available CVSRs is constrained with (8.12i). This bitwise MILP reformulation provides the flexibility to change the reactance in discrete steps, in case an actual reactance consists of a bank of discrete values as modeled in the proposed formulation.

Numerical Case Studies

The comparative analyses are performed on the modified IEEE 118-bus test system to examine the effectiveness of the proposed reformulation. The original test case data are taken from [84] and modifications are made according to [85]. The modified IEEE 118-bus test system still has 118 buses and 19 generators, but the marginal cost of active power generators and some branch and bus data was modified. Moreover, the total number of branches is reduced by one to 185. The modified costs are smaller by a factor of 50 to 100 than typical generation costs [72]. The same generation costs are used to make the results consistent with the previous reported in the reference. The power flow limits (long-term ratings are used here) play a critical role in the optimal CVSR allocation.

The cost of generation dispatch for different numbers of CVSRs and allowed reactance change (α) with the three approaches are summarized in Table 8.1. These cases cover a comprehensive range of scenarios regarding the number of CVSR and the allowable reactance change. Again, the scenarios are adopted from [71] so that comparison of the results is consistent with the reference.

Without any transmission parameter adjustments, all approaches produce the exact optimal generation cost of $ 2074.4. The refined formulation produces optimal costs that are very near the results obtained from the original two-stage formulation [71]. The refinement is in cleaning up

Table 8.1: Optimal cost comparison under different scenarios

# CVSR	$\alpha(\%)$	Cost ($/hr)		
		Two-Stage MILP [71]	Refined Two-Stage MILP	Bitwise MILP
-	-	2074.4	2074.4	2074.4
13	2	2015.7	2014.7	2007
29	5	1887.4	1883.3	1871
27	10	1684.9	1692	1668.8
31	20	1502.2	1506.9	1487
23	30	1454.3	1464.4	1440.9
31	50	1335.2	1336.6	1316.5
24	70	1306	1303.3	1303.4
11	90	1303.3	1303.3	1303.3

the original formulation, by removing unnecessary constraints and combining some of them for a more concise formulation. Hence, the results should be the same as in the original formulation. The slight differences in the total optimal costs can be attributed to the numerical precisions of the solvers and a larger optimality gap used in the original work (either 3% or 6%, conditionally) to generate the results. The results produced using the refined formulation uses at most a 2.5% optimality gap.

It can be seen from Table 8.1 that the optimal cost produced using the bitwise MILP is always better or at least the same as those produced using the original/refined formulations. Except for the last two cases, the optimal costs are generated using only one susceptance branch ($Nbits = 1$); this means susceptance values are allowed to change from minimum to maximum with zero in between. For the last two cases with higher values of α, $Nbits = 4$ is used.

The relationship between the total available CVSRs and the objective values of the CVSR allo-

cation problem with the modified IEEE 118-bus system is shown in Figure 8.2- Figure 8.4. The figures show three scenarios with different reactance ranges ($\alpha = 5\%, \alpha = 30\%, \alpha = 90\%$), and the optimal costs are compared between the two-stage MILP and the bitwise MILP approach. It can be seen that for all scenarios, with both approaches, the cost is inversely proportional to the number of CVSR. However, for $\alpha = 90\%$, after 11 CVSRs, addition of more CVSRs does not decrease the optimal cost as the most economic dispatch cost for the system is already reached. The bitwise MILP produces consistently better or the same cost as the two-stage MILP formulation for all scenarios. Even for $\alpha = 90\%$, when CVSR number is less than 11, the optimal cost from bitwise MILP formulation is slightly better. From the results summarized, the effectiveness of the proposed method is easily observed.
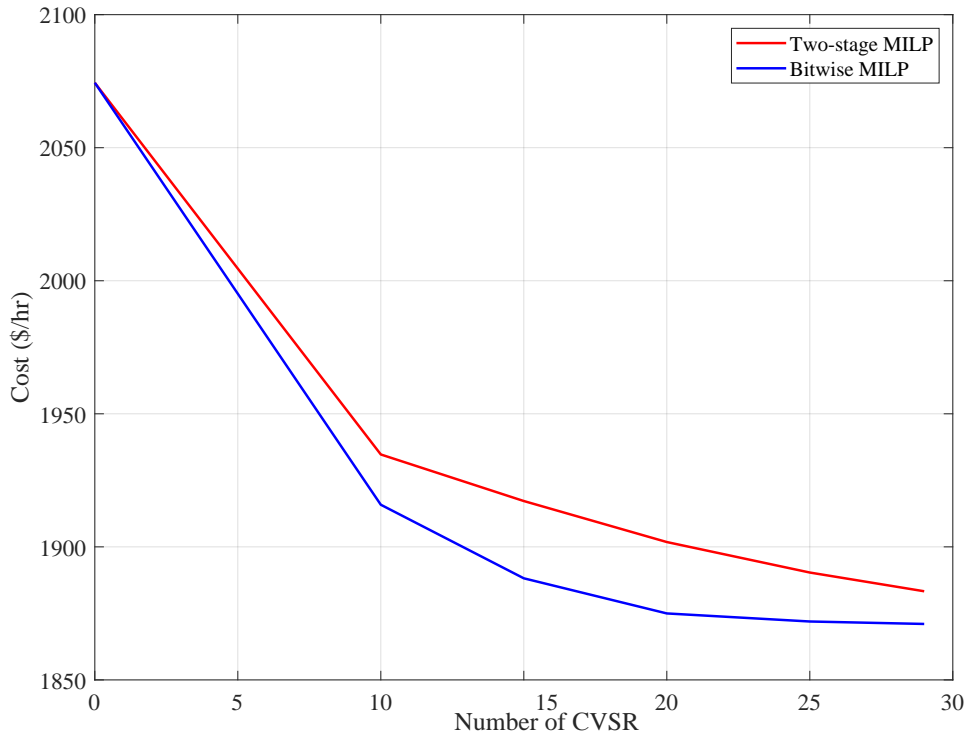
Figure 8.2: Total generation costs with up to 30 CVSR devices with $\alpha = 5\%$
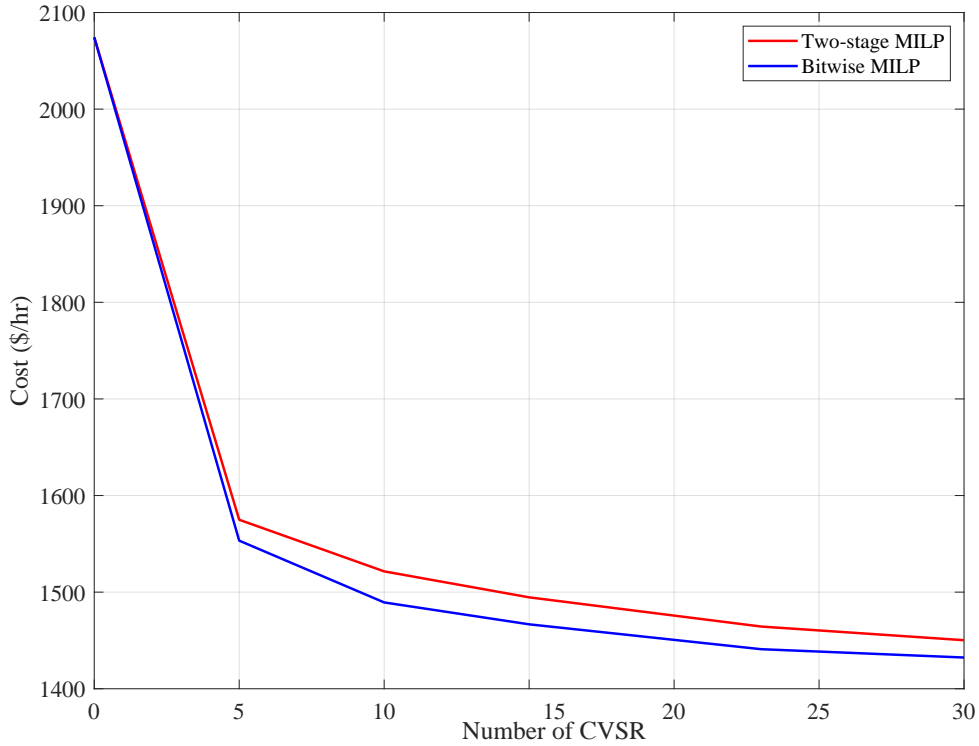
Figure 8.3: Total generation costs with up to 30 CVSR devices with $\alpha = 30\%$

The impact of the number of parallel branches in the susceptance bank connected in series with the transmission line on the optimal generation cost is shown in Fig. 8.5. Here, the two scenarios with the highest values of α were considered. In both of the scenarios, the cost reduces with the increase of the number of susceptance branches. Increasing $Nbits$ from 1 to 4, the cost reduction of \$147.13 and \$38.76 is achieved, for scenario I ($\alpha = 90\%, \#$ of $CVSR = 5$) and scenario II ($\alpha = 70\%, \#$ of $CVSR = 24$), respectively. It is worth noting again that the generator cost parameters used here are scaled-down by a factor of 50 to 100 from the typical generation costs [72]. Otherwise, the actual savings from the bitwise reformulation will be much higher. However, it should also be noted that these savings come at higher computational costs. Therefore, the $Nbits$ parameter should be selected carefully, according to the computational resource requirements and
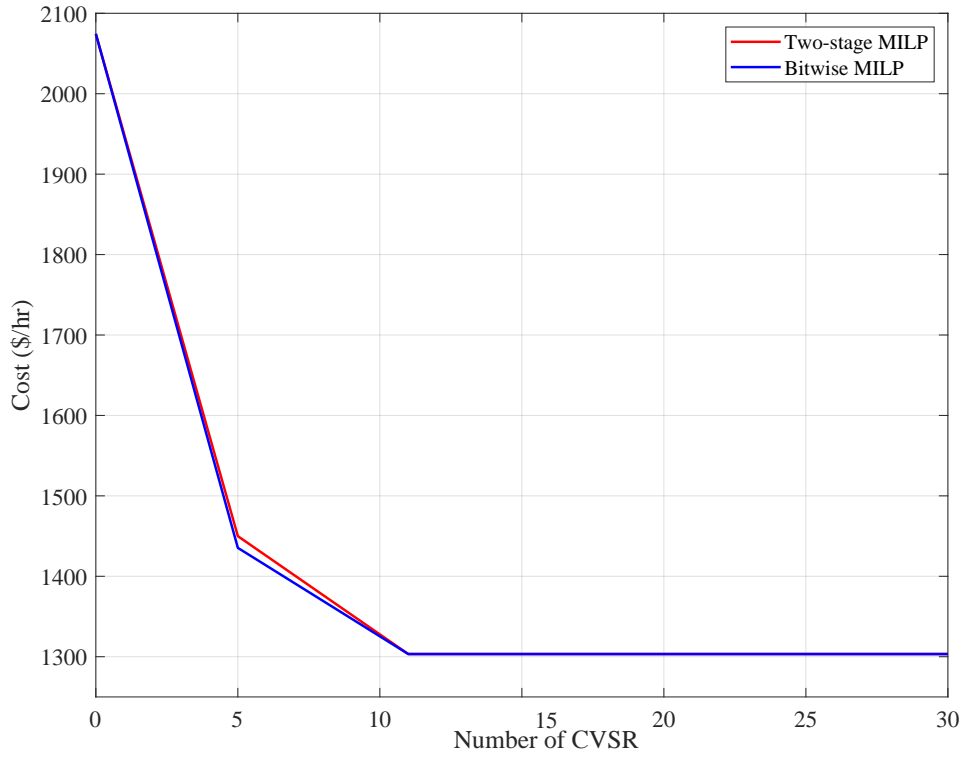
Figure 8.4: Total generation costs with up to 30 CVSR devices with $\alpha = 90\%$

any computational time constraints with the cost reduction.

Conclusion

A novel MILP-based optimization reformulation is presented for CVSR allocation and sizing, originally a MINLP, with some preliminary comparative results for the modified IEEE 118-bus test system. Compared to the two-step MILP formulation, which gives a suboptimal cost because of the assumed fixed direction of power flow for the line(s) with VSR, the proposed approach provides optimal results with a straightforward one-step reformulation. The new approach provides optimal generation cost results consistently better or the same as the two-stage MILP formulation in a wide
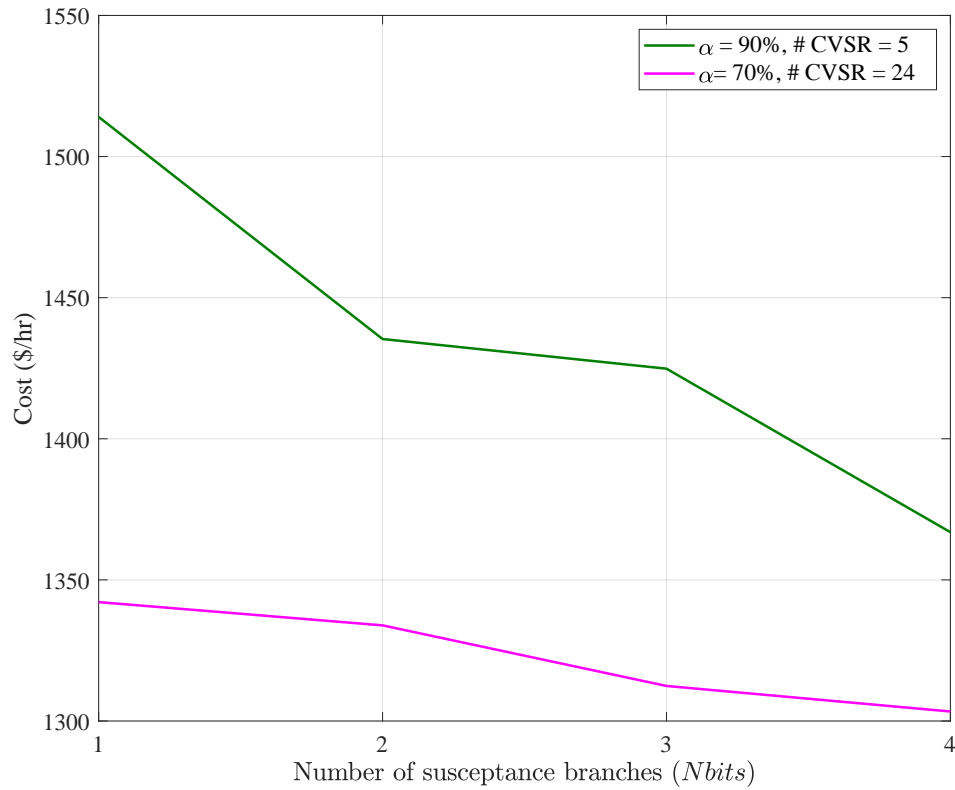
Figure 8.5: Cost comparison with $Nbits$ variation

range of cases. The optimal cost results can follow closely the results from the previous approach by choosing an appropriate number of steps for the susceptance change within the transmission line(s). The added advantage of the presented formulation is that it works for all scenarios of power flow without any exceptions. Also, this approach inherently allows for discrete step changes.

The future work will provide an in-depth analysis with more extensive test cases and scenarios, along with modifications in the formulation to make it computationally competitive, while considering AC feasibility, system stability, and (N-1) reliability criteria.

CHAPTER 9: CONCLUSION

Research Contribution Summary

Recent changes in the power industry, including market operations, emerging technologies, governmental policies and regulations, increased frequency and intensity of extreme weather events, have strained the existing transmission and distribution (T&D) system. Due to the prolonged lead times, getting the most out of the existing T&D infrastructure is the only viable choice shortly, and it is vital to find ways to optimize its utilization. The major problem is that an effective alternating current (ac) power flow control is challenging to achieve. Power electronics-based flexible ac transmission system (FACTS) devices have been considered a solution, but the semiconductor ratings and converter complexities make them costly and unreliable. This dissertation discussed non-FACTS-based power electromagnetic devices, which can provide some of the simplest yet efficient, robust, and cost-effective solutions for a wide range of problems in the power systems without the limitations of the FACTS-based solutions.

This dissertation covered various power inductor facets like designs, modeling, and applications. While exploring these topics, some novel designs and applications were identified and pursued.

First, the dissertation highlighted the importance of analytical modeling with a design optimization example. Both single objective and multi-objective design optimizations are presented for the standard gapped ferromagnetic core reactor with the closed-form reactance relations obtained from the MEC approach.

The reactance of magnetic amplifier (MA) was presented as a function of both AC and DC supplies. Two machine learning (ML)-based frameworks were introduced and applied to characterize a MA: the artificial neural network (ANN) and physics-informed artificial neural network (PIANN).

158

With an ample tranining data, A machine learning approach–ANN–outperformed physics-based numerical and analytical techniques. However, it could produce physically inconsistent results and behave like a black-box without any system information. The PIANN leveraged the complementary strengths of ANN and a physics-based model to improve MA modeling. Here MA modeling based on magnetic equivalent circuit (MEC) was aided by ANN using the finite element analysis (FEA) simulation results as training data sets. The ML performance matrices showed the validity of the ANN-based frameworks. Among the frameworks, PGANN based analytical modeling presented an excellent promise because of its accuracy, computational advantage, and ability to produce closed-form solutions.

A few novel designs for three-phase continuously variable series reactors (CVSRs) are presented with the reactance modulation. The purposed MECs are validated with the FEA based models. Those reactor designs are intended to solve the distribution transformer overloading issue in a low voltage meshed distribution network.

Additionally, the issue with the gaps in the standard ferromagnetic core reactor were discussed, and a unique design of the gapless ferromagnetic core reactor (GFCR) was introduced to solve those issues. A numerical method based on finite element analysis (FEA) verification of the MEC-based analytical modes is presented. A generic expression for the inductance of the reactor in terms of the characteristic design variable was derived.

Impact of addition of such variable reactance in the optimal power flow (OPF) was discussed with an unique OPF formulation was presented. The addition of variable series reactance device makes the DC optimal power flow – a linearized approximation of the AC OPF – a non-linear program (NLP) problem. In this dissertation, a mixed-integer linear program (MILP) reformulation for the optimal allocation (site & size) of available variable series reactor (VSR) devices was presented. The reactance variation of a transmission line was achieved by controlling parallel susceptances

in a susceptance bank connected in series with a line in discrete steps. The effectiveness of the proposed reformulation was examined by comparing its results with a state-of-the-art technique implemented in the modified IEEE 118 bus system. The comparison showed a great potential of the proposed approach in terms of globally optimal solutions and their interpretations/applicability.

Future Directions

The findings from the dissertation pave the way for various future avenues in the advancement of reactor technology. Some immediate possible future works based on the dissertation are listed below.

1. Improve the accuracy of the reactor analytical models by capturing the leakage fluxes as much as possible.

2. Explore the application of constant and variable reactors for modern power system issues and challenges. One such application could be to reduce the extreme voltage impact of high PV penetration with the reactors.

3. Expand and check the OPF formulation with the variable series reactors for scalability, computational efficiency, AC feasibility, system stability, and reliability.

4. Experimentally validate the reactors' ratings and performance and further reactor analysis with the hardware-in-the-loop (HIL) simulations.

5. Better understand and expand the working of the magnetic amplifier. One way would be to combine the transformer technology with the magnetic amplifier technology to develop a voltage regulating transformer.

6. Amalgamate the principles of the gapless ferromagnetic reactor (GFCR) and magnetic amplifier to convert constant reactance GFCR to a varying reactance device with the strategic placement of DC windings.

APPENDIX A: LIST OF PUBLICATIONS

Journal

S. Pokharel and A. Dimitrovski, "Ferromagnetic Core Reactor Modeling and Design Optimization," in *Advances in Science, Technology and Engineering Systems Journal*, vol. 6, no. 1, pp. 810-818 (2021).

S. Pokharel and A. Dimitrovski, "Analytical Modeling of a Gapless Ferromagnetic Core Reactor," in *IEEE Transactions on Magnetics*, vol. 56, issue 2, 2020.

Conference

S. Pokharel and A. Dimitrovski, "Analytical Modeling of a Three-phase Magnetic Amplier-based Continuously Variable Reactor," in *IEEE PES T&D Conference & Exposition*, Chicago, IL, Oct. 2020.

S. Pokharel and A. Dimitrovski, "Modeling of An Enhanced Three-phase Continuously Variable Reactor," in *IEEE Power & Energy Society General Meeting*, Montreal, Canada, Aug. 2020.

S. Pokharel and A. Dimitrovski, "Analytical Modeling of A Ferromagnetic Core Reactor," in *IEEE PES North American Power Symposium (NAPS)*, Wichita, KS, Oct. 2019.

S. Pokharel and A. Dimitrovski, "A Gapless Ferromagnetic Core Reactor - Magnetic Equivalent Circuit & Inductance", in *IEEE Power & Energy Society General Meeting*, Atlanta, GA, Aug. 2019.

APPENDIX B: IEEE COPYRIGHT STATEMENT

More IEEE sites

IEEE

Author ✦ Center

Resources & Tools
for Authors

Search this section 🔍

Journal Authors ▶

Home » Choose a Publishing Agreement »
Avoid Infringement upon IEEE Copyright

Avoid Infringement upon IEEE Copyright

Learn when and how to get permission to reuse IEEE
material to avoid infringement upon IEEE Copyright.

As a general rule, you will need to request permission to
reproduce content published by IEEE. This may include
any text, graphics, tables, or other material from an IEEE
publication.

Permission can be requested and approved online in
minutes through IEEE's partnership with RightsLink®, the
automated permission granting service from the
Copyright Clearance Center. Click the copyright symbol in
the icon menu of the article's Abstract page in
IEEE *Xplore® Digital Library* ↗ to submit your permission
request via RightsLink.

165

The answers to some frequent permissions questions are included below. Further questions may be directed to pubs-permissions@ieee.org.

Can I Reuse Material From a Previous Article I Published With IEEE?

Although authors are permitted to reuse all or portions of the work in other works, this does not include granting third party requests for reprinting, republishing, or other types of reuse. Permission is required.

Can I Reuse My Published Article in My Thesis?

You may reuse your published article in your thesis or dissertation without requesting permission, provided that you fulfill the following requirements depending on which aspects of the article you wish to reuse.

- **Text excerpts:** Provide the full citation of the original published article followed by the IEEE copyright line: © 20XX IEEE. If you are reusing a substantial portion of your article and you are not the senior author, obtain the senior author's approval before reusing the text.

166

- **Graphics and tables:** The IEEE copyright line (© 20XX IEEE) should appear with each reprinted graphic and table.
- **Full text article:** Include the following copyright notice in the references: "© 20XX IEEE. Reprinted, with permission, from [full citation of original published article]."

When posting your thesis on your university website, include the following message:

> "In reference to IEEE copyrighted material which is used with permission in this thesis, the IEEE does not endorse any of [name of university or educational entity]'s products or services. Internal or personal use of this material is permitted. If interested in reprinting/republishing IEEE copyrighted material for advertising or promotional purposes or for creating new collective works for resale or redistribution, please go to http://www.ieee.org/publications_standards/publications/rights/ to learn how to obtain a License from RightsLink. If applicable, University Microfilms and/or ProQuest Library, or the Archives of Canada may supply single copies of the dissertation."

167

Only the accepted version of your article, **not the final published version**, may be posted online in your thesis.

Do I Need Permission to Republish in Another Language?

Yes, you will need to request a license that includes translation rights. Use the RightsLink procedure outlined above to submit the request. The license you receive from RightsLink will include guidelines and a disclaimer to be displayed on the translated article.

Do I Need Permission to Reuse IEEE Material in Another IEEE Publication?

You may reuse small portions of text (up to several paragraphs) and graphics from one IEEE publication in another, provided that you provide full citation to the original article. Contact pubs-permissions@ieee.org if you wish to reuse larger portions.

Where Can I Post My Published Article?

See our policy on posting your article for detailed information.

Subscribe to our newsletter

Home
New Authors

168

APPENDIX C: ASTESJ OPEN ACCESS POLICY

Quick Links ▼

ASTES Journal
A Bimonthly Peer-Review Journal (ISSN: 2415-6698)

Search...   **Search**

☰ ✖ Menu

Home | Editorial Board | Archive ▾ | CFP ▾ | Online Submission | Instructions for Authors ▾ | About Journal ▾

Open Access Information and Policy

All articles published by ASTES Journal are made immediately available worldwide under an open access license. This means:

- everyone has free and unlimited access to the full-text of *all* articles published in ASTES Journal, and
- everyone is free to re-use the published material if proper accreditation/citation of the original publication is given.
- open access publication is supported by the authors' institutes or research funding agencies by payment of a comparatively low Article Processing Charge (APC) for accepted articles.

ASTES Journal started to publish articles under the Creative Commons Attribution License and are now using the latest version of the CC BY-SA license, which grants authors the most extensive rights. This means that all articles published in ASTES Journal, including data, graphics, and supplements, can be linked from external sources, scanned by search engines, re-used by text mining applications or websites, blogs, *etc.* free of charge under the sole condition of proper accreditation of the source and original publisher.

There are various advantages of open access of authors. Some advantages are listed below

- Everyone can freely access and download the full text of all articles published with ASTES Journal: readers of open access journals, i.e., mostly other researchers, do not need to pay any subscription or pay-per-view charges to read articles published by ASTES Journal.
- Open access paper get high citations.
- ASTESJ has a very low publication cost and also provides various discounts to authors.
- Accepted articles are typically published online more rapidly in ASTES Journal than those of traditional journals.

CFP for Special Issue

Special Issue on Multidisciplinary Sciences and Engineering

Special Issue on Innovation in Computing, Engineering Science & Technology

Important Links

» Scopus Indexed Papers
» Online Submission System
» Special Issue Proposal Application
» Journal Template (Word & Latex)
» Online Submission Guidelines
» Call for Papers
» Abstract & Indexing
» Publication Fee
» Copyright Form

Past Issues

» Conferences
» Special Issues
» Volume 1
» Volume 2
» Volume 3
» Volume 4
» Volume 5
» Volume 6
» Volume 7
    » Issue 1

Facebook Page

Send message

170

Creative Commons License Deed

Attribution 4.0 International (CC BY 4.0)

This is a human-readable summary of (and not a substitute for) the license.

You are free to:

Share — copy and redistribute the material in any medium or format

Adapt — remix, transform, and build upon the material

for any purpose, even commercially.

The licensor cannot revoke these freedoms as long as you follow the license terms.

Under the following terms:

Attribution — You must give appropriate credit, provide a link to the license, and indicate if changes were made. You may do so in any reasonable manner, but not in any way that suggests the licensor endorses you or your use.

No additional restrictions — You may not apply legal terms or technological measures that legally restrict others from doing anything the license permits.

Notices:

You do not have to comply with the license for elements of the material in the public domain or where your use is permitted by an applicable exception or limitation.

No warranties are given. The license may not give you all of the permissions necessary for your intended use. For example, other rights such as publicity, privacy, or moral rights may limit how you use the material.

171

LIST OF REFERENCES

[1] A. D. Mills, R. H. Wiser, and K. Porter, "The cost of transmission for wind energy: A review of transmission planning studies," LBNL, Berkeley, Tech. Rep., Feb. 2009, p. 66.

[2] K. K. Sen and M. L. Sen, "Applications of facts controllers," in *Introduction to FACTS Controllers: Theory, Modeling, and Applications*. 2009, pp. 1–12. DOI: `10.1002/9780470524756.ch1`.

[3] C. Schauder, M. Gernhardt, E. Stacey, *et al.*, "Development of a ± 100 MVAR static condenser for voltage control of transmission systems," *IEEE Transactions on Power Delivery*, vol. 10, no. 3, pp. 1486–1496, 1995. DOI: `10.1109/61.400933`.

[4] ——, "Operation of ± 100 MVAR TVA STATCON," *IEEE Transactions on Power Delivery*, vol. 12, no. 4, pp. 1805–1811, 1997. DOI: `10.1109/61.634209`.

[5] G. Wolf, J. Skliutas, G. Drobnjak, and M. De Costa, "Alternative method of power flow control using air core series reactors," in *2003 IEEE Power Engineering Society General Meeting (IEEE Cat. No.03CH37491)*, vol. 2, 2003, 574–580 Vol. 2. DOI: `10.1109/PES.2003.1270362`.

[6] K. Papp, G. Christiner, H. Popelka, and M. Schwan, "High voltage series reactors for load flow control," *e & i Elektrotechnik und Informationstechnik*, vol. 121, no. 12, pp. 455–460, 2004.

[7] S. Pokharel and A. Dimitrovski, "Analytical modeling of a gapless ferromagnetic core reactor," *IEEE Transactions on Magnetics*, vol. 56, no. 2, pp. 1–10, 2020, ©2020 IEEE. DOI: `10.1109/TMAG.2019.2949932`.

[8] ——, "Modeling of an enhanced three-phase continuously variable reactor," in *2020 IEEE Power Energy Society General Meeting (PESGM)*, ©2020 IEEE, 2020, pp. 1–5. DOI: 10.1109/PESGM41954.2020.9282074.

[9] ——, "Analytical modeling of a ferromagnetic core reactor," in *2019 North American Power Symposium (NAPS)*, ©2019 IEEE, 2019, pp. 1–6. DOI: 10.1109/NAPS46351.2019.9000352.

[10] C. W. T. McLyman, *Transformer and inductor design handbook*. CRC press, 2017.

[11] "Ieee standard for requirements, terminology, and test code for dry-type air-core series-connected reactors - redline," *IEEE Std C57.16-2011 (Revision of IEEE Std C57.16-1996) - Redline*, pp. 1–194, 2012.

[12] C. F. Burgess and B. Frankenfield, *Regulation of electric circuits.* US Patent 720,884, Feb. 1903.

[13] J. G. Miles, "Bibliography of magnetic amplifier devices and the saturable reactor art," *Transactions of the American Institute of Electrical Engineers*, vol. 70, no. 2, pp. 2104–2123, 1951.

[14] U. S. Navy, *Magnetic amplifiers: Another lost technology*, (edited by G. Trinkaus in 2000), 1951.

[15] P. Mali, *Magnetic Amplifiers: Principles and Applications*, 261. JF Rider, 1960.

[16] W. A. Geyger, *Magnetic-amplifier circuits: basic principles, characteristics, and applications*. McGraw-Hill, 1954.

[17] A. Dimitrovski, Z. Li, and B. Ozpineci, "Magnetic amplifier-based power-flow controller," *IEEE transactions on power delivery*, vol. 30, no. 4, pp. 1708–1714, 2015.

[18] A. Dimitrovski, Z. Li, and B. Ozpineci, "Applications of Saturable-core Reactors (SCR) in Power Systems," *2014 IEEE PES T & D Conference and Exposition*, pp. 1–5, 2014, ISSN: 21608563. DOI: 10.1109/TDC.2014.6863404.

[19] B. Raju, K. Parton, and T. Bartram, "A current limiting device using superconducting dc bias applications and prospects," *IEEE Transactions on Power Apparatus and Systems*, no. 9, pp. 3173–3177, 1982.

[20] F. Moriconi, N. Koshnick, F. De La Rosa, and A. Singh, "Modeling and test validation of a 15kv 24mva superconducting fault current limiter," in *IEEE PES T&D 2010*, IEEE, 2010, pp. 1–6.

[21] S. Abbott, D. Robinson, S. Perera, F. Darmann, C. Hawley, and T. Beales, "Simulation of hts saturable core-type fcls for mv distribution systems," *IEEE transactions on power delivery*, vol. 21, no. 2, pp. 1013–1018, 2006.

[22] C. Zhao, S. Wang, J. Qiu, *et al.*, "Transient simulation and analysis for saturated core high temperature superconducting fault current limiter," *IEEE Transactions on Magnetics*, vol. 43, no. 4, pp. 1813–1816, 2007.

[23] F. Moriconi, F. De La Rosa, A. Singh, B. Chen, M. Levitskaya, and A. Nelson, "An innovative compact saturable-core hts fault current limiter - development, testing and application to transmission class networks," in *IEEE PES General Meeting*, 2010, pp. 1–8. DOI: 10.1109/PES.2010.5590090.

[24] J. Jin, S. Dou, H. Liu, *et al.*, "Electrical application of high T_c superconducting saturable magnetic core fault current limiter," *IEEE Transactions on Applied Superconductivity*, vol. 7, no. 2, pp. 1009–1012, 1997. DOI: 10.1109/77.614678.

[25] A. Dimitrovski, Z. Li, and B. Ozpineci, "Magnetic amplifier-based power-flow controller," *IEEE Transactions on Power Delivery*, vol. 30, no. 4, pp. 1708–1714, 2015. DOI: `10.1109/TPWRD.2015.2400137`.

[26] M. Young, A. Dimitrovski, Z. Li, Y. Liu, and R. Patterson, "Continously variable series reactor: Impacts on distance protection using ccvts," in *2015 IEEE Power & Energy Society General Meeting*, IEEE, 2015, pp. 1–5.

[27] X. Zhang, K. Tomsovic, and A. Dimitrovski, "Security constrained multi-stage transmission expansion planning considering a continuously variable series reactor," *IEEE Transactions on Power Systems*, vol. 32, no. 6, pp. 4442–4450, 2017.

[28] K. Lin, K. Tomsovic, Q. Wan, and A. Dimitrovski, "A study of magnetic amplifier-based power flow controller for power system stability improvement," *Electric Power Components and Systems*, vol. 44, no. 9, pp. 966–973, 2016. DOI: `10.1080/15325008.2015.1131770`. eprint: `https://doi.org/10.1080/15325008.2015.1131770`. [Online]. Available: `https://doi.org/10.1080/15325008.2015.1131770`.

[29] S. Pokharel and A. Dimitrovski, "Analytical modeling of a three-phase magnetic amplifier-based continuously variable reactor," in *2020 IEEE/PES Transmission and Distribution Conference and Exposition (T D)*, ©2020 IEEE, 2020, pp. 1–5. DOI: `10.1109/TD39804.2020.9299988`.

[30] L. F. Romba, S. S. Valtchev, R. Melício, M. V. Mudrov, and A. M. Ziuzev, "Electric vehicle battery charger controlled by magnetic core reactor to wireless power transfer system," in *2017 IEEE International Conference on Environment and Electrical Engineering and 2017 IEEE Industrial and Commercial Power Systems Europe (EEEIC / I CPS Europe)*, 2017, pp. 1–6. DOI: `10.1109/EEEIC.2017.7977782`.

[31] X. Chen, B. Chen, C. Tian, J. Yuan, and Y. Liu, "Modeling and harmonic optimization of a two-stage saturable magnetically controlled reactor for an arc suppression coil," *IEEE*

175

Transactions on Industrial Electronics, vol. 59, no. 7, pp. 2824–2831, 2012. DOI: `10.1109/TIE.2011.2173090`.

[32] L. Austrin and G. Engdahl, "Modeling of a three-phase application of a magnetic amplifier," in *Proc. of the 24th International Congress of the Aeronautical Sciences*, 2004, pp. 1–8.

[33] M. Tian, Q. Li, and Q. Li, "A controllable reactor of transformer type," *IEEE Transactions on Power Delivery*, vol. 19, no. 4, pp. 1718–1726, 2004. DOI: `10.1109/TPWRD.2004.832352`.

[34] A. Balakrishnan, W. T. Joines, and T. G. Wilson, "Air-gap reluctance and inductance calculations for magnetic circuits using a schwarz-christoffel transformation," *IEEE Transactions on Power Electronics*, vol. 12, no. 4, pp. 654–663, 1997.

[35] M. Moallem and G. Dawson, "An improved magnetic equivalent circuit method for predicting the characteristics of highly saturated electromagnetic devices," *IEEE Transactions on magnetics*, vol. 34, no. 5, pp. 3632–3635, 1998.

[36] A. Deihimi, "Improved Model of Saturated Regions in Magnetic Equivalent Circuits of Highly Saturated Electromagnetic Devices," *11th International Conference on Optimization of Electrical and Electronic Equipment, OPTIM*, pp. 45–50, 2008. DOI: `10.1109/OPTIM.2008.4602385`.

[37] X. Chen and B. Wang, "Optimal design and modeling of the multi-stage saturable magnetically controlled reactor," in *2017 Progress In Electromagnetics Research Symposium - Spring (PIERS)*, 2017, pp. 76–81. DOI: `10.1109/PIERS.2017.8261710`.

[38] D. A. Lowther, "Automating the design of low frequency electromagnetic devices - A sensitive issue," *COMPEL - The International Journal for Computation and Mathematics in Electrical and Electronic Engineering*, vol. 22, no. 3, pp. 630–642, 2003, ISSN: 03321649. DOI: `10.1108/03321640310475083`.

[39] M. Amrhein and P. T. Krein, "3-D Magnetic Equivalent Circuit Framework for Modeling Electromechanical Devices," *IEEE Transactions on Energy Conversion*, vol. 24, no. 2, pp. 397–405, 2009, ISSN: 08858969. DOI: `10.1109/TEC.2009.2016134`.

[40] J. Cale, S. Sudhoff, and L.-Q. Tan, "Accurately modeling ei core inductors using a high-fidelity magnetic equivalent circuit approach," *IEEE Transactions on Magnetics*, vol. 42, no. 1, pp. 40–46, 2006. DOI: `10.1109/TMAG.2005.859439`.

[41] A. Taher, S. Sudhoff, and S. Pekarek, "Calculation of a tape-wound transformer leakage inductance using the mec model," *IEEE Transactions on Energy Conversion*, vol. 30, no. 2, pp. 541–549, 2015.

[42] B. N. Cassimere, S. D. Sudhoff, and D. H. Sudhoff, "Analytical design model for surface-mounted permanent-magnet synchronous machines," *IEEE Transactions on Energy Conversion*, vol. 24, no. 2, pp. 347–357, 2009.

[43] S. D. Sudhoff, "Magnetics and magnetic equivalent circuits," in *Power Magnetic Devices: A Multi-Objective Design Approach*. 2014, pp. 45–112. DOI: `10.1002/9781118824603.ch02`.

[44] G. M. Shane and S. D. Sudhoff, "Refinements in anhysteretic characterization and permeability modeling," *IEEE Transactions on Magnetics*, vol. 46, no. 11, pp. 3834–3843, 2010. DOI: `10.1109/TMAG.2010.2064781`.

[45] G. M. Masters, *Basic Electric and Magnetic Circuits*, second. Wiley, 2005, pp. 1–49, ISBN: 0471280607. DOI: `10.1002/0471668826.ch1`.

[46] A. Taher, S. Sudhoff, and S. Pekarek, "Calculation of a tape-wound transformer leakage inductance using the mec model," *IEEE Transactions on Energy Conversion*, vol. 30, no. 2, pp. 541–549, 2015. DOI: `10.1109/TEC.2015.2390260`.

177

[47] S. D. Sudhoff, "Selected magnetic steel data," in *Power Magnetic Devices: A Multi-Objective Design Approach*. Wiley-IEEE Press, 2014, pp. 443–444. DOI: `10.1002/9781118824603.app3`.

[48] D. S. Weile and E. Michielssen, "Genetic algorithm optimization applied to electromagnetics: A review," *IEEE Transactions on Antennas and Propagation*, vol. 45, no. 3, pp. 343–353, 1997. DOI: `10.1109/8.558650`.

[49] S. D. Sudhoff, "Optimization-based design," in *Power Magnetic Devices: A Multi-Objective Design Approach*. Wiley-IEEE Press, 2014, pp. 1–44. DOI: `10.1002/9781118824603.ch01`.

[50] S. Sudhoff and Y. Lee, "Goset manual version 1.03," *Available from Scott Sudhoff, Purdue University School of Electrical and Computer Engineering*, 2004.

[51] K. Deb, A. Pratap, S. Agarwal, and T. Meyarivan, "A fast and elitist multiobjective genetic algorithm: Nsga-ii," *IEEE Transactions on Evolutionary Computation*, vol. 6, no. 2, pp. 182–197, 2002. DOI: `10.1109/4235.996017`.

[52] M. Gyimesi and D. Ostergaard, "Inductance computation by incremental finite element analysis," *IEEE transactions on magnetics*, vol. 35, no. 3, pp. 1119–1122, 1999.

[53] J. Cale, S. Sudhoff, and J. Turner, "An improved magnetic characterization method for highly permeable materials," *IEEE transactions on magnetics*, vol. 42, no. 8, pp. 1974–1981, 2006.

[54] G. M. Shane and S. D. Sudhoff, "Refinements in anhysteretic characterization and permeability modeling," *IEEE transactions on magnetics*, vol. 46, no. 11, pp. 3834–3843, 2010.

[55] A. Barili, A. Brambilla, G. Cottafava, and E. Dallago, "A simulation model for the saturable reactor," *IEEE Transactions on Industrial Electronics*, vol. 35, no. 2, pp. 301–306, 1988. DOI: `10.1109/41.192663`.

[56] M. Young, "Saturable reactor for power flow control in electric transmission systems: Modeling and system impact study," *Ph.D. dissertation, University of Tennessee*, 2015.

[57] B. Donnot, I. Guyon, M. Schoenauer, P. Panciatici, and A. Marot, *Introducing machine learning for power system operation support*, 2017. arXiv: 1709.09527 [stat.ML].

[58] M. Sun, I. Konstantelos, and G. Strbac, "A deep learning-based feature extraction framework for system security assessment," *IEEE Transactions on Smart Grid*, vol. 10, no. 5, pp. 5007–5020, 2019. DOI: 10.1109/TSG.2018.2873001.

[59] J. H. Arteaga, F. Hancharou, F. Thams, and S. Chatzivasileiadis, "Deep learning for power system security assessment," in *2019 IEEE Milan PowerTech*, 2019, pp. 1–6. DOI: 10.1109/PTC.2019.8810906.

[60] F. Thams, A. Venzke, R. Eriksson, and S. Chatzivasileiadis, "Efficient database generation for data-driven security assessment of power systems," *IEEE Transactions on Power Systems*, vol. 35, no. 1, pp. 30–41, 2020. DOI: 10.1109/TPWRS.2018.2890769.

[61] F. Fioretto, T. W. Mak, and P. Van Hentenryck, "Predicting ac optimal power flows: Combining deep learning and lagrangian dual methods," in *Proceedings of the AAAI Conference on Artificial Intelligence*, vol. 34, 2020, pp. 630–637.

[62] A. K. Noor, "AI and the Future of the Machine Design," *Mechanical Engineering*, vol. 139, no. 10, pp. 38–43, Oct. 2017, ISSN: 0025-6501. DOI: 10.1115/1.2017-Oct-2. eprint: https://asmedigitalcollection.asme.org/memagazineselect/article-pdf/139/10/38/6360198/me-2017-oct2.pdf. [Online]. Available: https://doi.org/10.1115/1.2017-Oct-2.

[63] F. Filippetti, G. Franceschini, C. Tassoni, and P. Vas, "Recent developments of induction motor drives fault diagnosis using ai techniques," *IEEE Transactions on Industrial Electronics*, vol. 47, no. 5, pp. 994–1004, 2000. DOI: 10.1109/41.873207.

[64] G. S. Misyris, A. Venzke, and S. Chatzivasileiadis, "Physics-informed neural networks for power systems," *arXiv preprint arXiv:1911.03737*, 2019.

[65] K. Schneider, P. Phanivong, and J. Lacroix, "Ieee 342-node low voltage networked test system," in *2014 IEEE PES General Meeting — Conference Exposition*, 2014, pp. 1–5.

[66] S. Saha, N. Fernando, and L. Meegahapola, "Multi magnetic material laminated cores: Concept and modelling," in *2017 20th International Conference on Electrical Machines and Systems (ICEMS)*, 2017, pp. 1–5. DOI: 10.1109/ICEMS.2017.8056247.

[67] S. Pokharel and A. Dimitrovski, "A gapless ferromagnetic core reactor - magnetic equivalent circuit and inductance," in *2019 IEEE Power Energy Society General Meeting (PESGM)*, ©2019 IEEE, 2019, pp. 1–5. DOI: 10.1109/PESGM40551.2019.8973400.

[68] D. Lin, P. Zhou, Y. Hu, and M. Rosu, "Analytical computation of end-winding leakage inductance for multi-phase ac machines," in *2017 IEEE International Electric Machines and Drives Conference (IEMDC)*, 2017, pp. 1–6. DOI: 10.1109/IEMDC.2017.8002229.

[69] J. Zhu, *Optimization of Power System Operation*. John Wiley & Sons, 2014.

[70] M. Terbrueggen, "EPRI power systems dynamics tutorial," *Electric Power Reasearch Institute, EPRI,Palo Alto, CA*, pp. 1–1010, 2009.

[71] M. Sahraei-Ardakani and K. W. Hedman, "A Fast LP Approach for Enhanced Utilization of Variable Impedance Based FACTS Devices," *IEEE Transactions on Power Systems*, vol. 31, no. 3, pp. 2204–2213, 2016, ISSN: 08858950. DOI: 10.1109/TPWRS.2015.2447453.

[72] E. B. Fisher, R. P. O'Neill, and M. C. Ferris, "Optimal transmission switching," *IEEE Transactions on Power Systems*, vol. 23, no. 3, pp. 1346–1355, 2008. DOI: 10.1109/TPWRS.2008.922256.

[73] K. W. Hedman, R. P. O'Neill, E. B. Fisher, and S. S. Oren, "Optimal transmission switching—sensitivity analysis and extensions," *IEEE Transactions on Power Systems*, vol. 23, no. 3, pp. 1469–1479, 2008.

[74] G. Wolf, J. Skliutas, G. Drobnjak, and M. De Costa, "Alternative method of power flow control using air core series reactors," in *IEEE Power Engineering Society General Meeting (IEEE Cat. No.03CH37491)*, 2003, pp. 574–580, ISBN: 0780379896. DOI: `10.1109/pes.2003.1270362`.

[75] N. G. Hingorani and L. Gyugyi, "FACTS Concept and General System Considerations," in *Understanding FACTS*, Wiley-IEEE Press, 2009, pp. 1–34, ISBN: 9780470546802. DOI: `10.1109/9780470546802.ch1`. [Online]. Available: `http://ieeexplore.ieee.org/search/srchabstract.jsp?arnumber=5264427`.

[76] L. Gyugyi, C. D. Schauder, and K. K. Sen, "Static Synchronous Series Compensator: a Solid-State Approach To the Series Compensation," *IEEE Transactions on Power Delivery*, vol. 12, no. 1, pp. 406–417, 1997.

[77] D. M. Divan, W. E. Brumsickle, R. S. Schneider, *et al.*, "A distributed static series compensator system for realizing active power flow control on existing power lines," *IEEE Transactions on Power Delivery*, vol. 22, no. 1, pp. 642–649, 2007, ISSN: 08858977. DOI: `10.1109/TPWRD.2006.887103`.

[78] K. M. Rogers and T. J. Overbye, "Power flow control with distributed flexible ac transmission system (d-facts) devices," in *41st North American power symposium*, IEEE, 2009, pp. 1–6.

[79] A. Dimitrovski, Z. Li, and B. Ozpineci, "Magnetic Amplifier-Based Power-Flow Controller," *IEEE Transactions on Power Delivery*, vol. 30, no. 4, pp. 1708–1714, 2015, ISSN: 08858977. DOI: `10.1109/TPWRD.2015.2400137`.

[80] S. Sharma, Q. Huang, A. Tbaileh, and Q. Li, "Scenario-based analysis for disaster-resilient restoration of distribution systems," in *2019 North American Power Symposium (NAPS)*, IEEE, 2019, pp. 1–6.

[81] X. Zhang, K. Tomsovic, and A. Dimitrovski, "Optimal allocation of series FACTS devices in large-scale systems," *IET Generation, Transmission & Distribution*, vol. 12, no. 8, pp. 1889–1896, 2018, ISSN: 1751-8687. DOI: `10.1049/iet-gtd.2017.1223`.

[82] K. Baker, "Solutions of dc opf are never ac feasible," in *Proceedings of the Twelfth ACM International Conference on Future Energy Systems*, Virtual Event, Italy, 2021, pp. 264–268, ISBN: 9781450383332. DOI: `10.1145/3447555.3464875`.

[83] M. B. Cain, R. P. O'neill, A. Castillo, *et al.*, "History of optimal power flow and formulations," *Federal Energy Regulatory Commission*, vol. 1, pp. 1–36, 2012.

[84] R. D. Zimmerman, C. E. Murillo-Sánchez, and R. J. Thomas, "Matpower: Steady-state operations, planning, and analysis tools for power systems research and education," *IEEE Transactions on power systems*, vol. 26, no. 1, pp. 12–19, 2010.

[85] S. Blumsack, *Network topologies and transmission investment under electric-industry restructuring*. Carnegie Mellon University, 2006.